Reservoir Delineation Using Bandwidth Extension and Phase Decomposition

by
Understanding Olaniyi Aikulola

A Dissertation submitted to
the Department of Earth and Atmospheric Sciences

in partial fulfillment of the requirements for the degree of
Doctor of Philosophy

in Geophysics

Chair of Committee: Dr. John Castagna

Committee Member: Dr. Evgeny Chesnokov

Committee Member: Dr. Yingcai Zheng

Committee Member: Dr. Arnold Oyem

University of Houston
December 2019

ACKNOWLEDGEMENTS

My journey in life, including this PhD program, has only been possible by the grace of God through my Lord and Saviour, Jesus Christ.

My advisor, Dr. John Castagna, has been very supportive all the way, right form the day we met at one of the SEG conferences, it has been moments of quality learning and friendship. I am so fortunate to have such an icon as my supervisor. My committee members, Dr. Evgeny Chesnokov, Dr. Yingcai Zheng and Dr. Arnold Oyem have stood by me and have been reliable to show up and make positive contributions all through the program.

Members of the faculty and graduate students of University of Houston have made the program very worthwhile especially during the late lectures, field trips and unending discussions along the way. Members of staff of Lumina Technologies, Inc, especially Gabriel Gil, the Chief Geophysicist, have been very generous with peer assists and constructive challenges.

My soul mate, Dr. Oluwayemisi Grace Aikulola, has been a pillar throughout my life journey since our paths crossed about eighteen years ago. It’s likely this program might not have been completed but for her sacrifices and continuous encouragements, especially when it did not make sense to continue. Thank you, Sweetheart, for all you do behind the scene to support my dreams and aspirations.

ABSTRACT

Sandstone reservoir units prevalent in an upper slope Niger Delta oil field are commonly below seismic temporal resolution. Although conventional seismic amplitude and amplitude-variation-with-offset are good indicators of oil-filled reservoir rock in this area, they do not necessarily show the vertical distribution of reservoir and may sometimes be suppressed for thin pay intervals.

In some cases, multiple sub-tuning reservoir sands appear as one event on the original seismic data and derived attributes. Bandwidth extension using sparse-layer inversion better resolves thin layers than does the original seismic data and can detect multiple interfaces that are not otherwise seismically separated. As the hydrocarbon-filled reservoirs are low impedance relative to the surrounding shales, phase decomposition enhances amplitude anomalies and is found to have improved correlation between seismic amplitude and presence or absence of hydrocarbons.

Combining bandwidth extension and phase decomposition improves determination of the internal architecture of pay intervals as sub-tuning vertical variations in impedance become more apparent as are lateral changes in thickness. Resulting amplitude maps are sharper and provide better delineation of the areal reservoir distribution of reservoir as evidenced by well ties.

TABLE OF CONTENTS

LIST OF FIGURES

LIST OF TABLES

CHAPTER ONE

INTRODUCTION

1.1 Background

Direct hydrocarbon indication of oil reservoirs occurring in young clastic basins using seismic amplitudes and amplitude-variation-with-offset is well-established industry practice in exploration and development operations (e.g., Backus and Chen, 1975; Ostrander, 1984; Brown, 2011; Roden and Forrest, 2005) and has been widely used in Niger Delta prospecting (Adeoye et al., 2009; Opara, 2010; Oyeyemi et al., 2018). In the Niger Delta, compressible sandstone reservoirs containing light oil are expected to exhibit classical bright spots on near-angle stacks or full stacks (Hilterman, 2001). However, as reservoir pay intervals are commonly thinner than seismic temporal resolution (Widess, 1973), challenges remain. In sub-tuning intervals, the vertical distribution of pay intervals within a given interval may be seismically indeterminate, limiting the interpretation of reservoir architecture. Furthermore, lateral variations in amplitude may be due to changes in fluids or net reservoir thickness.

Conventional seismic inversion methods, such as the colored inversion (Lancaster and Whitcombe; 2000), are limited by the inherent resolution of the seismic data, which is determined by wavelet center frequency and bandwidth (Kallweit and Wood, 1982). However, it is well established that a constrained seismic inversion can possibly resolve layers much finer than the commonly assumed one-quarter wavelength (Widess, 1973) limit of seismic resolution (Hill, 2005; Puryear and Castagna; 2008). This leads to the idea that, with appropriate assumptions, the seismic bandwidth could be extended to higher frequencies (e.g. Smith et al., 2008; Yu et al., 2012); inversion being one possible means of doing so. Zhang and Castagna (2011) formulate a sparse reflectivity inversion method (sparse-layer inversion) for stacked seismic reflection data that is unbiased against thin layers and demonstrate its use in bandwidth extension.

However, bandwidth extension is controversial due to (1) the idea from linear filtering theory that a linear inverse filter will only amplify noise at frequencies where signal is missing, (2) the common use of non-physical methods that transform low into high frequencies while destroying the integrity of the signal, and (3) the non-uniqueness of seismic inversion. Regarding point (3), the argument that one can put anything in the inversion null space (frequencies outside the original band) and still be compatible with the original data is compelling until one realizes that constrained inversion is not simply putting “anything” at those frequencies but is rather exploiting a priori information to recover some of that signal. Liang and Castagna (2017) thoroughly discuss the controversial aspects of bandwidth extension, distinguish valid from invalid methods that do not improve resolution, and demonstrate the efficacy of the Zhang and Castagna (2011) method in improving resolution on synthetic and real data. They conclude that, given a sparse blocky earth-impedance structure, valid bandwidth extension can be achieved in the presence of noise on stacked data. Unlike previous work, Zhang et al. (2013) extended the sparse-layer inversion to pre-stack data.

Spectral periodicities that cannot be captured within the frequency band of the original seismic data cannot be extrapolated beyond the seismic bandwidth. As pointed out by Liang and Castagna (2017), the most serious case happens when the reflectivity time series is drawn from a uniform distribution from sample to sample. In this case, noise outside the seismic band is greatly amplified and no signal can be inferred. However, even in this worst-case situation, signal within the original seismic band can be amplified more than noise. Hence, Liang and Castagna (2017) find that the minimum extension achievable is spectral broadening within the seismic band with less noise amplification at frequencies with poor signal than would result from spiking deconvolution or other spectral shaping (Weiner, 1964). In the case of transitional geological environments, such as upwards coarsening or fining grain size and associated mineralogy resulting in a temporal ramp in seismic impedance, to the extent that the vertically varying impedance structure can be replicated by a blocky staircase, and if the vertical extent is such that the reciprocal of time-thickness is within the first half of the original seismic bandwidth so as to produce readily quantifiable spectral periodicity, spectral broadening outside the seismic band may still be possible to some degree. As a rule, when the earth model is not a true sparse blocky impedance structure, one can expect to only partially infer signal outside the original seismic band; with commensurate reduction in well ties. For the purpose of this study, the objective is only to identify top and base of layers and highlight anomalous behavior. This may still be possible, even with imperfect signal reconstruction outside the seismic band, and the purpose of this study is to evaluate the effectiveness at doing so in a real data situation.

1.2 Theory

According to the convolutional model of reflection seismograms, it is possible to express the recorded seismic trace as a simple convolution:

$$s(t) = w(t) * r(t) + n(t), \qquad (1)$$

where s(t) is the recorded seismogram, w(t) is the seismic wavelet, r(t) is the reflectivity series or earth's impulse response and n(t) is random noise. This model assumes a simplistic scenario of earth layers with uniform rock properties within the layers, ignoring many wave-propagation effects. It is possible to obtain bandwidth extension by extrapolating the spectrum outside the seismic bandwidth that has been originally sampled. The bandwidth extension is possible, because any transient signal has an infinite frequency response, some of which may be recoverable provided that enough of the spectrum has been sampled. Assuming the convolutional model stated in equation 1 adequately simulates seismic wave propagation and seismic data processing, it is valid to view seismic data as a band-limited version of the reflection-coefficient time series; the reflectivity spectrum within the data bandwidth is shaped by the wavelet spectrum, whereas the frequencies outside the band of the wavelet are zeroed out, causing an ambiguity in resolving seismic reflections. A blocky earth structure provides a physical basis for a valid bandwidth extension as the reflectivity spectrum is a superposition of layer responses that are sinusoidal in the frequency domain (Liang and Castagna, 2017).

Bracewell (1965) defined even, II(t), and odd, $I_I(t)$ impulse-pair symbols by:

$$II(t) = \delta(t + \tfrac{1}{2}) + \delta(t - \tfrac{1}{2}), \qquad (2)$$

and

$$I_I(t) = \delta(t + \tfrac{1}{2}) - \delta(t - \tfrac{1}{2}), \qquad (3)$$

where, δ(t) is the Dirac delta function taken to be a unit impulse at time zero in the context of signal processing. A layer with time thickness Δt and reflection coefficients, r, of equal magnitude and sign at the top and base, can be represented by an even impulse pair rII(t/Δt), with the reflectivity spectrum given by a real function:

$$II(f) = 2r\cos(\pi \Delta t f), \qquad (4)$$

which is periodic in frequency, f. For odd-impulse pairs, the spectrum is an imaginary sine function:

$$I_I(f) = i2r\sin(\pi \Delta t f). \qquad (5)$$

The basis for phase decomposition is the exact mathematical relationship showing that any waveform can be represented as the sum of symmetrical (even) and anti-symmetrical (odd) waveforms (Bracewell, 1965):

$$S(t) = Se(t) + So(t), \qquad (6)$$

where, Se(t) and So(t) are the unique even and odd parts which are the "phase components"; as Se(t) has a real spectrum it has 0° or 180° constant phase. Similarly, So(t) has an imaginary spectrum and, therefore, plus or minus 90° constant phase. The odd and even parts can be uniquely derived from S(t) using Se(t) = [S(t) + S(-t)]/2 and

$So(t) = [S(t) - S(-t)]/2$. As these relations hold for any time series, they also hold exactly for the reflection coefficient series r(t). Assuming the convolutional model, where the seismogram is given by convolution of the wavelet with the reflectivity series and neglecting noise, for the response phase of a segment of S(t), ϕS is defined as:

$$\phi S = \phi r + \phi w, \qquad (7)$$

where, ϕr, is the response phase of the local reflectivity series and ϕw is the phase of the wavelet. For a zero-phase wavelet, the phase of the local signal is thus the phase of the reflectivity. The phase components of the signal thus conform to the phase components of the reflectivity. If the wavelet is not zero phased, the wavelet phase must be considered in subsequent analysis.

The effect of light hydrocarbons is for the impedance of a reservoir layer to be lower than the same reservoir rock frame fully filled with brine. Irrespective of the original reflectivity, the effect of adding hydrocarbons to a brine-filled layer is thus to make the pressure reflection coefficient at the top of the layer more negative (softer) and the pressure reflection coefficient at the base more positive (harder). Ignoring travel-time effects for the moment, this adds a -90° odd-impulse pair of some magnitude to the original reflection coefficient pair. This is illustrated schematically in Figure 1.1.

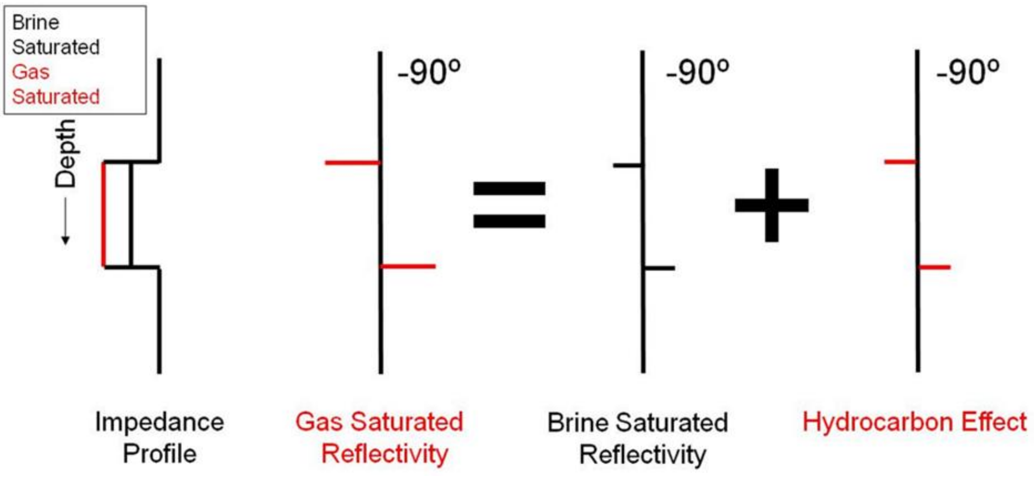

Figure 1.1 - The reflectivity for a gas-saturated layer is equal to the reflectivity of the brine-saturated layer plus the hydrocarbon effect, which is the change in reflection coefficients at top and base of the layer when gas is added. This relation is perfect in depth, but there will be misalignment in time due to the difference in velocity of gas-saturated and brine-saturated rocks.

To carry this idea into the time domain, one can rely on the concept from Widess (1973) that waveform shape is weakly dependent on time-thickness for thin layers below seismic tuning. Then a simple thin layer has a reflection waveform for gas-filled reservoir, Sgas(t), that is defined to be equal to the corresponding fluid-substituted brine-sand response, Sbrine(t), plus a hydrocarbon effect, ΔShyd(t),

$$\mathrm{Sgas}(t) = \mathrm{Sbrine}(t) + \Delta\mathrm{Shyd}(t). \qquad (8)$$

As light (low density) hydrocarbons always reduces the impedance in sandstones relative to brine (e.g. Domenico, 1977), as evident in Figure 1.1, the effect of hydrocarbons when added to compressible brine-filled reservoir quality sandstones is to make the odd part of the reflectivity more negative in phase. As the layer impedance drops when hydrocarbons are added, the reflection coefficient at the top of the layer becomes more negative and the reflection coefficient at the base of the layer becomes more positive, adding a -90° phase component to the series. After the reflectivity series is convolved with a wavelet, the seismic waveform amplitude is, thus, also more negative. In the case of bright spots (low impedance layers), the result is a larger magnitude negative response. In the case of dim spots (high impedance layers), the result is a smaller magnitude positive response.

Phase decomposition (Castagna et al., 2016) breaks any seismic event response, S(t), centered at the instantaneous amplitude peak of an event (t=0), into the unique odd (asymmetrical) and even (symmetrical) parts, So(t) and Se(t), as described above. These can be further subdivided into parts with primarily positive or negative phase (see Figure 1.6 in the Appendix A). This is done for every event on the waveform and time locally summed to form traces that are sums of positive and negative odd and even parts as a function of time. These four parts are the fundamental phase components of the seismic response. The -90° phase component trace is thus the sum of all negative phase odd parts and the +90° phase component trace is the sum of all positive phase odd parts. Similarly, the 0° phase component trace is the sum of all positive phase even parts and the 180° trace the sum of all negative phase even parts.

The concept of phase decomposition is illustrated for a very thin low impedance layer in Figure 1.2. A conventional exploration paradigm is the expectation that, for a zero-phase wavelet, a low impedance thin layer should manifest as a -90° soft over hard response (in pressure units this is a trough over peak). However, if the reflection coefficient pair at top and base of the thin layer is not perfectly equal and opposite (odd), the result can be surprising. As shown in a schematic representation in Figure 1.2, the thin-layer response is much closer to zero phase than -90° in this case. This is because, as the layer thins, the even component of the reflectivity reinforces while the odd component cancels out (and goes to zero at zero thickness). However, the -90° phase component of the mixed phase signal is disentangled from the even component by phase decomposition and shows the expected trough-over-peak response.

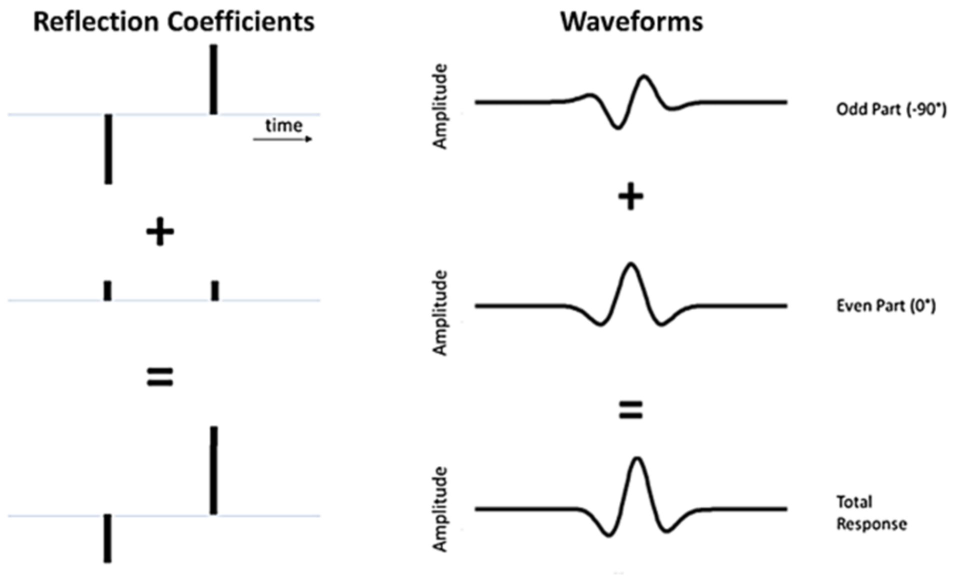

Figure 1.2: Schematic representation of phase decomposition. Reflection coefficient pair at the top and base of a low impedance thin layer (bottom left) decomposed into a strong odd impulse pair (top left) and a weak even impulse pair (middle left). The time thickness is 2 ms and the relative magnitudes of the reflection coefficients are -.8 at the top of the layer and 1.2 at the bottom of the layer. Contrary to conventional interpretation expectation, the total response is almost zero phase rather than almost -90° phase. Separating into even and odd components, the odd part of the waveform (top right) has been diminished by destructive interference while the even part (middle right) has been reinforced to the point where it can dominate the response phase of the total response (bottom right).

The proof of the additive property of reflective coefficients is detailed in Appendix A (Peterson et al., 1955).

1.3 Seismic Data

A baseline survey acquired with East-West parallel shooting acquired almost 20 years ago was combined with a monitor survey acquired about 10 years ago (with North-South parallel shooting). Both surveys used single vessel streamer acquisition. The baseline survey was acquired using 10 streamers of 408 channels each (giving a 5100 m active length) while the monitor survey had 10 streamers of 480 channels each (6000 m cable length). Both surveys were reprocessed as a single dataset with only 5% of the traces in the merged survey coming from the baseline survey. These data were incorporated and processed to better undershoot the field (minimize reduced fold by shooting around surface structures). The time-lapse effect on the monitor data set was inconsequential as there was only marginal production in the field before the acquisition of both vintages of seismic data. Due to residual hydrocarbon effects, the change in impedance with oil saturation over time is expected to be second order for the purposes of this study, given that the study is not an attempt to quantitatively predict rock properties with seismic inversion and will focus entirely on discerning the vertical and lateral distribution of hydrocarbon-bearing sandstone.

A standard processing sequence as outlined in Figure 1.3 was used to improve the signal to noise ratio and image the subsurface. Seismic data was processed for the wavelet to be zero phased. For this study, seismic well tie was done to apply any residual phase rotations.

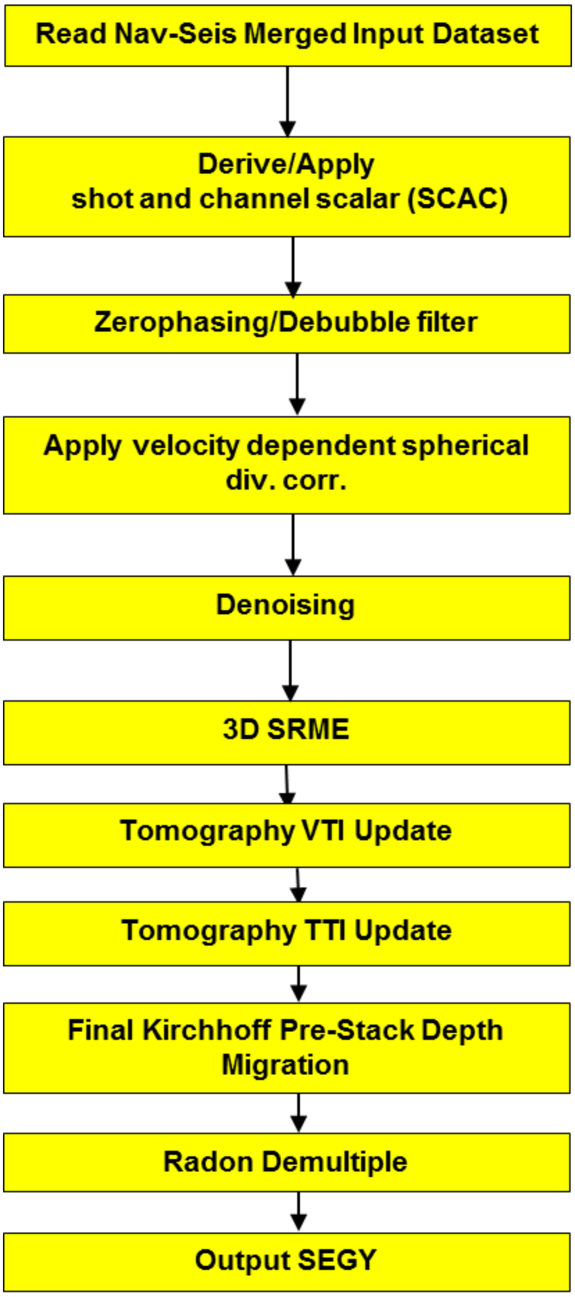

Figure 1.3 Seismic Processing Flow Summary.

1.4 Objectives

In the field of study, oil-saturated reservoir sandstones stand out as relatively blocky impedance anomalies. If thicker than about 1/4 of the P-wave wavelength, it is expected they will be readily seen on sparse or band-limited seismic inversions. However, if they are below seismic resolution, conventional seismic inversion methods may fail to resolve them. Given the blocky nature of the target sands, it is reasonable to attempt to improve resolution by extending the seismic bandwidth via sparse-layer inversion. This bandwidth extension is accomplished by inverting for reflectivity and bandpass filtering the reflection coefficients to a usable bandwidth selected by maximizing correlation with synthetics at validation wells. An objective of this study is to evaluate the use of pre-stack bandwidth extension to detect and resolve oil reservoirs.

Even if resolution can be improved in this fashion, very thin low-impedance layers may suffer from poor signal strength due to destructive interference of reflections from the top and the base of the layer; any method to improve the hydrocarbon signal relative to background would be advantageous in delineation of the pay. Castagna et al. (2016) introduced phase decomposition as a method to enhance seismic amplitude anomalies based on the expected phase of seismic responses from thin layers. The signal enhancement is achieved by removing contributions to the reflectivity that do not exhibit the same phase as the effect of the hydrocarbons. Castagna et al. (2016), Meza et al. (2016) and Barbato et al. (2017) have shown the utility of phase decomposition for direct hydrocarbon detection. de Abreu et al., (in press) demonstrated the enhanced amplitude-variation-with offset (AVO) response achieved over a known gas field using phase decomposition.

1.5 Methodology

The method adopted in this study is to apply phase decomposition to the bandwidth-extended data to enhance amplitudes for thin oil-bearing intervals. In other words, angle-stack data was enhanced by increasing the frequency bandwidth and the resultant dataset was decomposed into different phase components in order to be able to better predict hydrocarbons away from, once validated at, the well locations.

CHAPTER TWO

GEOLOGY OF NIGER DELTA

2.1 Location

The Niger delta basin is situated on the continental margin of the Gulf of Guinea in equatorial West Africa, at the southern end of Nigeria bordering the Atlantic Ocean between latitudes 30 and 60, and longitudes 50 and 80 (Figure 2.1). Known oil and gas resources of the Niger Delta rank the province as the twelfth largest in the world, with 2.2% of the world's discovered oil and 1.4% of the world's discovered gas. To date, 34.5 billion barrels of recoverable oil and 93.8 trillion cubic feet of recoverable gas have been discovered. The Niger-Benue present-day drainage area of about 1,200,000 km^2 has produced a delta area of about 75,000 km^2 with a clastic fill with a maximum thickness of about 12,000 m. The Niger Delta is one of the most prominent basins in West Africa and the largest delta in Africa. The Niger Delta Province contains only one identified petroleum system referred to as the Tertiary Niger Delta (Akata-Agbada) Petroleum System (Orife and Avbovbo, 1982; Ekweozor and Daukoru, 1994; Reijers et al., 1996; Tuttle et al. 1999).

2.2 Regional Geologic Setting

The onshore portion of the Niger Delta is delineated by the geology of southern Nigeria and southwestern Cameroon (Figure 2.2). The northern boundary is the Benin flank, an east-northeast trending hinge line south of the West Africa basement massif. The northeastern boundary is defined by outcrops of the Cretaceous on the Abakaliki High and further east-southeast by the Calabar flank, a hinge line bordering the adjacent Precambrian. The offshore boundary of the Niger Delta is defined by the Cameroon volcanic line to the east, the eastern boundary of the Dahomey.

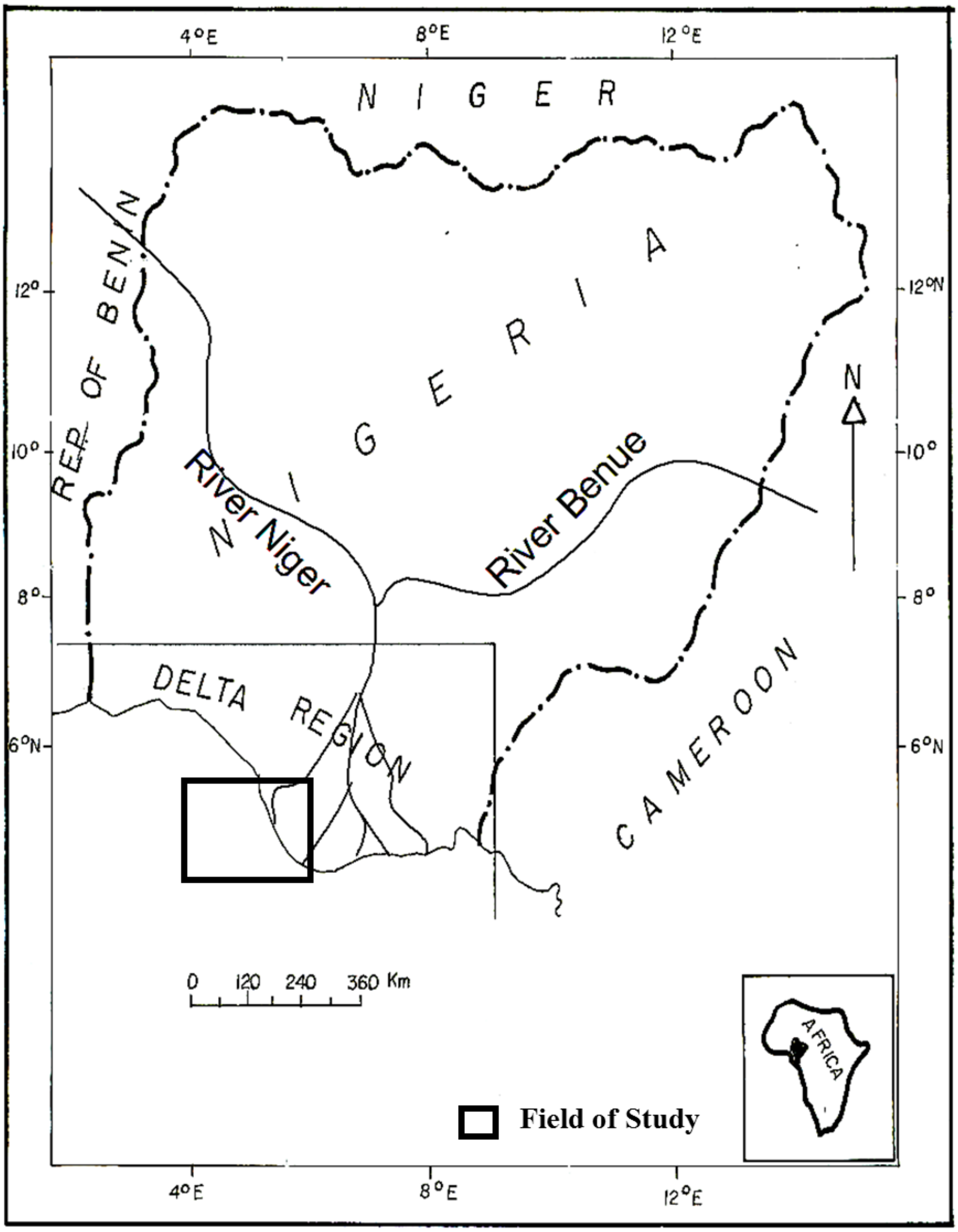

Figure 2.1: Location map of the Niger Delta showing the drainage system of Rivers Niger and Benue (modified from Orife and Avbovbo, 1982). The approximate location of the field studied is shown.

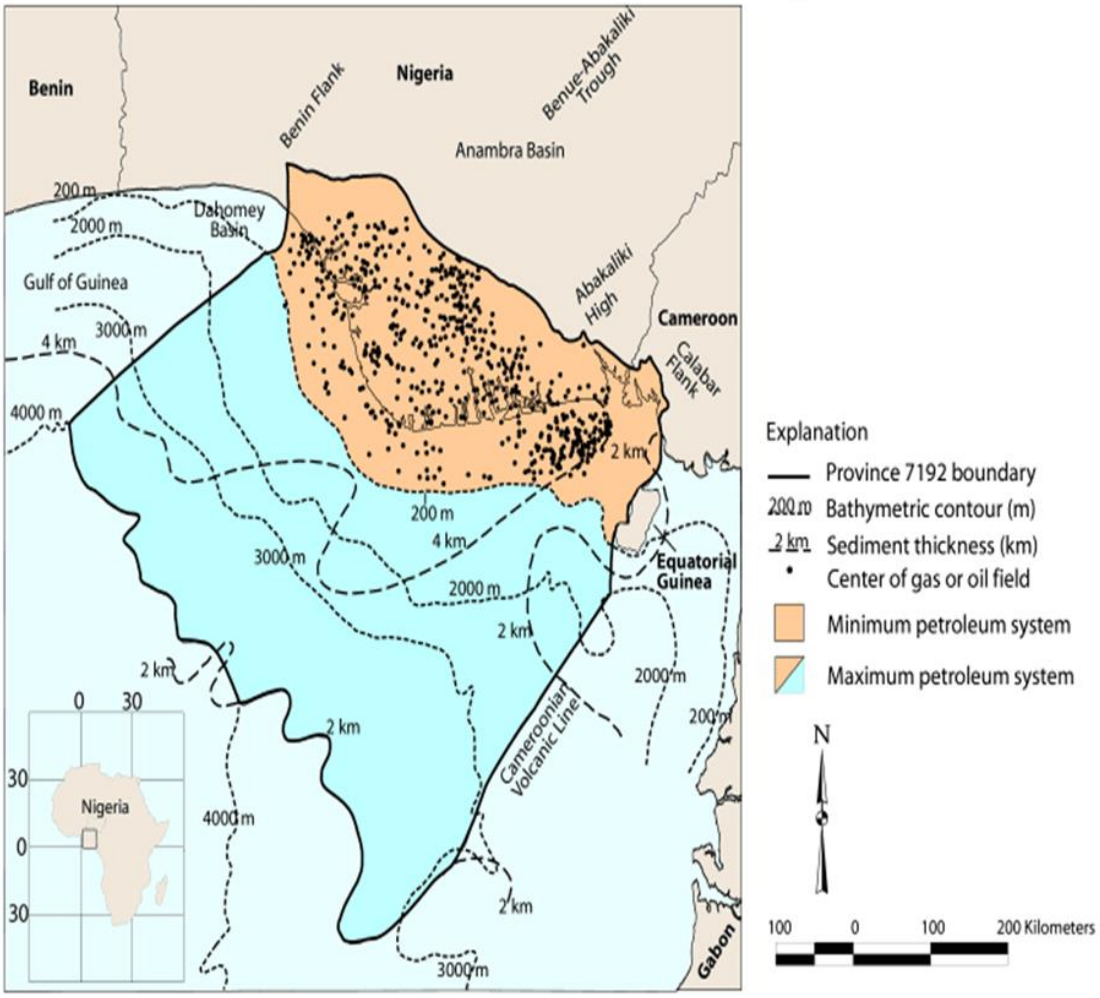

Figure 2.2 Regional geology outline map of the Niger Delta (Maximum petroleum system); bounding structural features; minimum petroleum system as defined by oil and gas field center points 200, 2000, 3000 and 4000m bathymetric contours; and 2 and 4km sediment thickness. (after Tuttle et al., 1999).

2.3 Development

The tectonic setting and geological evolution of the Niger Delta basin goes beyond the post-Eocene regressive clastic wedge that is conventionally ascribed to the modern delta, and the sedimentary entity within which the modern Niger Delta lies (Reijers et al., 1996). The development of the proto-Niger Delta began with the formation of the Benue-Abakaliki trough in the early Cretaceous as a failed arm of a rift triple junction associated with the opening of the south Atlantic (Burke et al., 1972; Weber and Daukoru 1975; Whiteman, 1982). From the Aptian to the Santonian, 6,000 m of sediments were deposited in the Benue-Abakaliki trough. During the Santonian, the Benue-Abakaliki trough was folded and uplifted to form the Abakaliki high, whereas to the west, the adjacent Anambra platform subsided to form the Anambra basin and, to the east, the Afikpo basin. The Anambra and Afikpo basins were the sites of deltaic sedimentation through the Paleocene.

Uplift of the Benin formation and the Calabar flank (parts of the lower Benue trough) during the Paleocene-early Eocene (Murat, 1972) initiated a major regressive phase represented by the Eocene to Holocene Niger Delta. From the Eocene to middle Miocene, the Niger Delta prograded along three main sedimentary axes;

- The Anambra basin (embayment)
- Enugu embayment fed by the Niger and Benue Rivers and
- Afikipo Syncline and Ikang trough fed by the Cross-River System

(Weber and Daukoru, 1975).

In the Miocene, uplift of the Cameroon Mountains in eastern Nigeria and adjacent Cameroon and the continued progradation of the delta resulted in merging of the Niger-Benue and Cross River delta lobes, which resulted in a progressive seaward shift of the coastline. The shoreline was about 16 km seaward of the present shoreline in the late Miocene and about 40km seaward by the Pleistocene (Figures. 2.3 and 2.4).

The modern delta dates from the late Pleistocene and records major regressive-transgressive sequences related to eustatic sea level fluctuations during the last glaciation (Allen, 1965).

2.4 Stratigraphy

The basal deposits of the sedimentary fill of the Benue trough are best exposed in the northern parts. They are the early Cretaceous alluvial fan, braided river, lacustrine and deltaic clastics of the Bima sandstone, which extend into the central Benue trough. The Asu River group underlies the southern parts.

The Tertiary stratigraphy of the Niger Delta has been described and defined by Short and Stauble, (1967), who recognized three distinct facies belts (formations). In ascending order, they are the prodelta facies; the paralic delta front facies; and the continental delta top facies.

(i) The prodelta facies (Akata formation): The Akata formation is generally an open marine and prodelta dark gray shale with lenses of siltstones and sandstone and plant remains at the top. Planktonic foraminifera may account for over 50% of the rich micro fauna and the benthonic assemblage indicates shallow marine shelf depositional environment. It is under compacted (i.e. over pressured) in much of the delta and believed to have been deposited in a front of the advancing delta and ranges from Eocene to Recent. It is over 1,200 m thick (Figure 2.5).

(ii) The paralic delta front facies (Agbada formation): The overlying Agbada formation consists of cyclic coarsening-upward regressive sequences and poor sorting resulting from distributory migration and deposition indicates fluviatile origin. The formation is rich in micro-fauna at the base decreasing upward and thus indicating an increasing rate of deposition in the delta front. The coarsening-upward sequences are composed of shales, siltstones, and sandstones, which include delta front and lower delta plain deposits (Weber, 1971). The thickness of the Agbada sequences is highly variable, but most are about 150 m thick. Transgressive deposits, although locally present, are thin and not everywhere distinguishable. The Agbada formation occurs in the subsurface of the entire delta area and may be continuous with the Ogwashi-Asaba and Ameki formations of Eocene to Oligocene age (Table 2.1). It is over 3,000 m thick and ranges from Eocene in the north to Pliocene/Pleistocene in the south and Recent in the delta surface (Short and Stauble, 1967).

In the south eastern part of the Niger Delta, the Agbada formation is divided into four members namely: the D-1, which is predominantly, regressive, marine sands and shales that contain minor oil and gas reservoirs; the Qua-Iboe, consisting of a thick pile of shale with thin intercalated sands that are possible oil and gas reservoirs in some places; the rubble beds; which lie directly below the Qua-Iboe are truncated beds, and the Biafra member; which is predominantly sands and shales and contains principal oil and gas reservoirs divided into upper, middle and lower units. Major hydrocarbon accumulations are found in the interval between Eocene and Pliocene age (Orife and Avbovbo, 1982).

(iii) Continental delta top facies (Benin formation): The Benin formation extends from the west across the whole Niger Delta and southward beyond the present coastline (Figure. 2.5). It is over 90% sandstone with shale intercalation. It is coarse-grained, gravelly, locally fine grained, poorly sorted, sub-angular to well-rounded and bears lignite streaks and wood fragments. It is continental deposits of probable upper deltaic depositional environment with various sedimentary deposits (point bar, channel fills, natural levees, back swamp deposits, oxbow fills) identifiable within this formation, indicating the variability of the shallow water depositional medium. It is of Oligocene age in the north becoming progressively younger southward. In general, it ranges from Miocene to Recent. The thickness is variable but generally exceeds 1,800 m. Very little hydrocarbon accumulation has been associated with the formation.

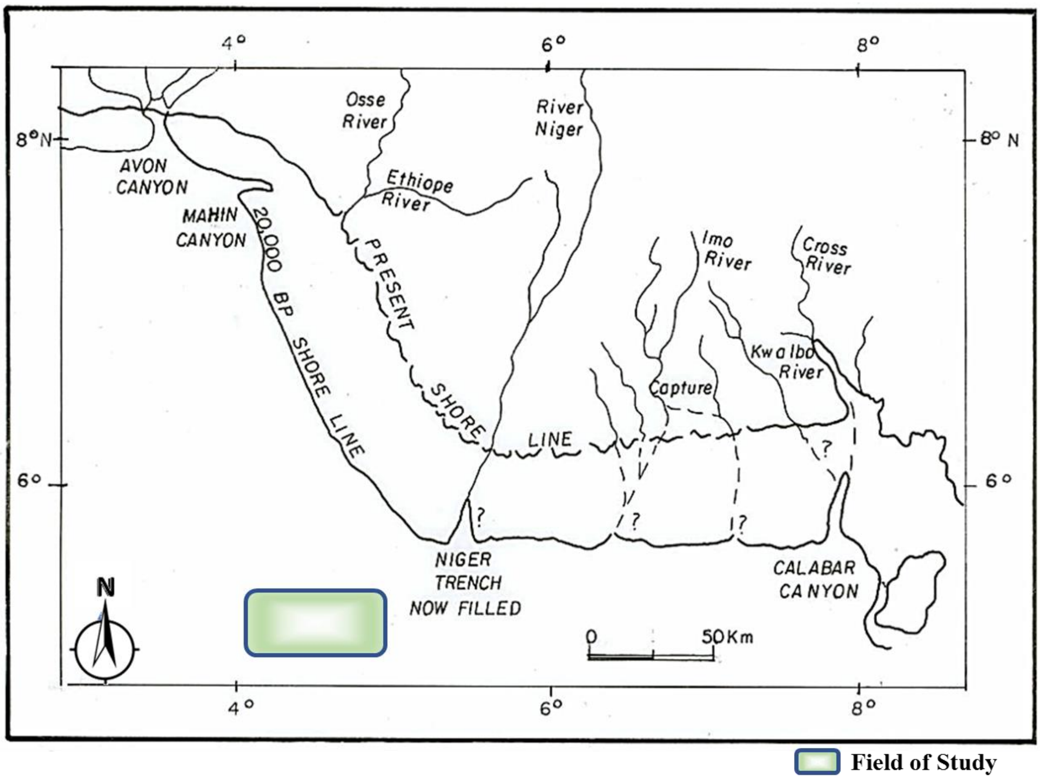

Figure 2.3 Present shoreline of the Niger Delta (modified from Allen, 1965). The approximate location of the field studied is shown.

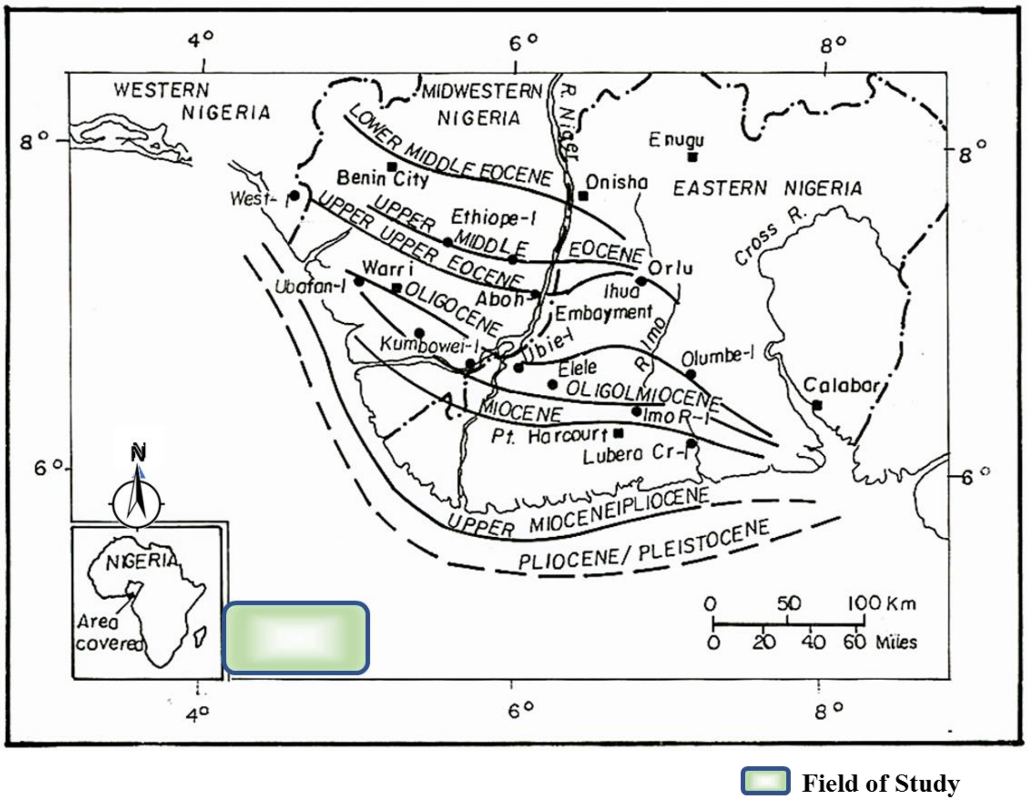

Figure 2.4 Palaeogeography of Tertiary Niger Delta (modified from Short and Stauble, 1967). The approximate location of the field studied is shown.

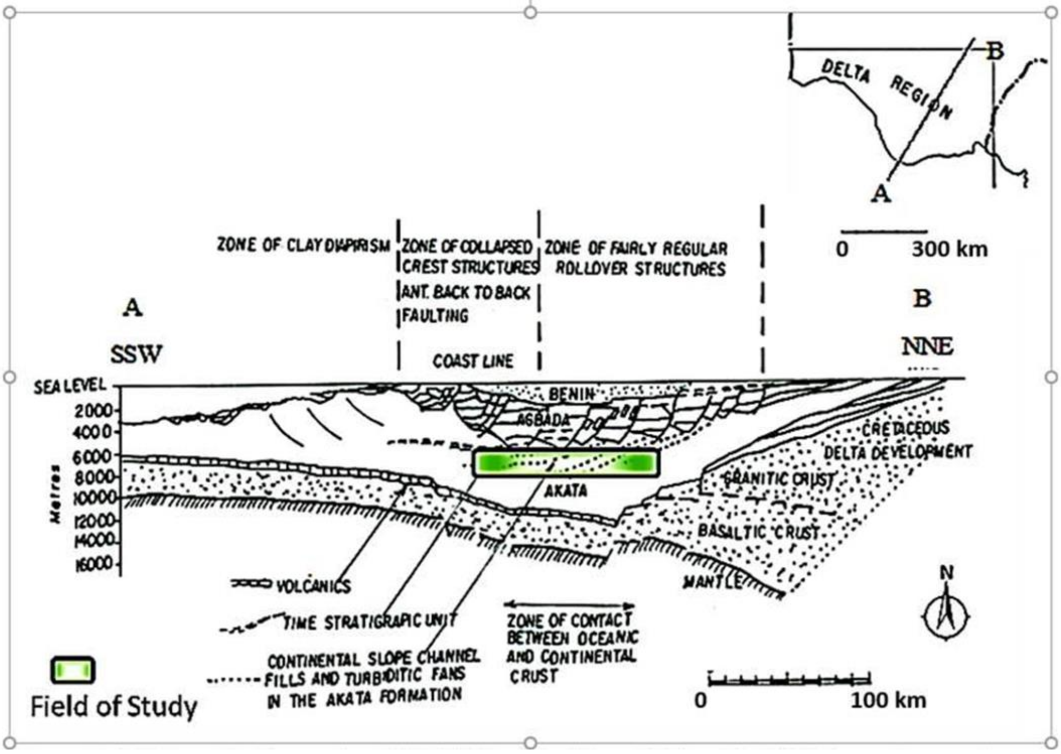

Figure 2.5 Schematic dip section SSW-NNE of the Niger Delta. The NNE formations outcrops as the Imo shale, Awgu shale and Eze Aku shale (modified from Merki, 1972). The approximate location of the field studied is shown.

Table 2.1: Formations in the Niger Delta Area (after Short and Stauble, 1967).

SUBSRFACE			SURFACE OUTCROPS		
YOUNGEST KNOWN AGE		OLDEST KNOWN AGE	YOUNGEST KNOWN AGE		OLDEST KNOWN AGE
RECENT	BENIN FORMATION (AFAM Clay Member)	OLIGOCENE	PLIO/PLEISTOCENE	BENIN FORMATION	MIOCENE
RECENT	AGBADA FORMATION	EOCENE	MIOCENE	OGWASHI-ASABA FORMATION	OLIGOCENE
			EOCENE	AMEKI FORMATION	EOCENE
RECENT	AKATA FORMATION	EOCENE	L. EOCENE	IMO SHALE FORMATION	PALEOCENE
			PALEOCENE	NSUKKA FM	MAESTRICHTIAN
			MAESTRICHTIAN	AJALI FORMATION	MAESTRICHTIAN
			CAMPANIAN	MAMU FORMATION	CAMPANIAN
		CRETACEOUS	CAMP/MAEST.	NKPORO SHALE	SANTONIAN
			CONIACIAN/SANTONIAN	AWGU SHALE	TURONIAN
			TURONIAN	EZE AKU SHALE	TURONIAN
			ALBIAN	ASU RIVER GROUP	ALBIAN

2.5 Sedimentary Environment

The sedimentary deposits of the Niger Delta continue offshore into the continental shelf. This structure is believed to contain sediments of varying lithology; exceeding 12,000 m near Warri. The depositional environments of these sedimentary accumulations vary from near-shore to non-marine, marginal-marine and deep-water deposits. Three major sedimentary environments have been recognized (Short and Stauble, 1967);

a) Continental environment: comprises the alluvial environments, including the braided-stream and meander-belt systems of the upper deltaic plain. The sediments deposited in this zone are predominantly sandy. Feldspar grains are fairly common and sand grains commonly are limonite coated. Finer-grained sediments (silt and clay) are deposited in the adjacent fresh-water back swamps and oxbows, together with large quantity of plant remains.

b) Transitional environment: comprises the brackish-water lower deltaic plain (mangrove swamps, floodplain basin, and marshes) and the coastal area with its beaches, barrier bars, and lagoons. The sediments in this environment are distinctly finer grained than in the continental environment. Feldspar is scarce, and brackish-water faunas may occur.

c) Marine environment: includes the submarine part of the delta, the delta fringe with its fine sand, silt, and clay, and the associated marine faunas. This environment grades laterally into the holo-marine environment that is not affected by deltaic activity. The sediments in the field of study are the deep-water turbiditic marine deposits.

2.6 Structures

Progradation of the delta has been accompanied and helped by formation of growth faults, associated rollover anticlines, and mud diapirism. Rapid sedimentation load and the gravitational instability of the Agbada sediment pile accumulating on the mobile, under-compacted Akata shales generate the growth faults. There is little or no growth faulting extending into the Benin formation. Toe thrusting (Figure 2.6) at the deltaic front occurs in front of the prograding depocenter with paralic sediments. Lateral growth faulting and related extension also account for the diapiric structures of the continental slope of the Niger Delta. Other structures include antithetic and synthetic faults and crestal faults. Series of fault blocks can be grouped to define macrostructures. Macrostructures can be grouped into sets to form megastructures, (Evamy et al., 1978). The megastructures are defined by major breaks in the regional dip of the delta. The southern limit of the structures is commonly marked by structure-building faults, which define the updip limit of major rollovers or counter regional faults. Along the axis of the delta, the megastructures are 30-60 km wide and well defined; whereas along the margins they narrow and coalesce (Evamy et al., 1978).

The environment of deposition in the field of study is the upper slope of the Niger Delta basin, where hydrocarbons are trapped by a complex combination of dip closure, faulting and stratigraphic pinch out. Changes in slope dip due to underlying shale-induced diapirism results in the formation of channelized deep-water turbidites that form excellent hydrocarbon reservoirs. Some faults provide preferential routes for sediment deposition. Sandstones form hydrocarbon traps that can be laterally amalgamated, or aggradationally stacked. Sand lobes can be separated by shales that form permeability barriers within a given reservoir interval. Thus, distinguishing sand lobes within the stacked reservoir can influence reservoir management decisions. The reservoirs are further modified by late-stage erosive sinuous channels that become mud filled on abandonment.

2.7 Hydrocarbon Distribution

The Niger Delta is rich in both oil and gas. Petroleum occurs throughout the Agbada formation of the Niger Delta. However, several directional trends form an "oil-rich belt" having the largest field and lowest gas-oil ratio (Ejedawe, 1981; Evamy et al. 1978; Doust and Omatsola, 1990). The belt extends from the northwest offshore area to the southeast offshore and along a number of north-south trends in the area of Port Harcourt. It roughly corresponds to the transition between continental and oceanic crust and is within the axis of maximum sedimentary thickness (Figure 2.6). This hydrocarbon distribution was originally attributed to timing of trap formation relative to petroleum migration (earlier landward structures trapped earlier migrating oil). Source rocks of the Niger Delta have been discussed in numerous studies. Short and Stauble (1967) suggested that the major source rocks were shales of the Agbada formation, a view supported by Reed (1969) who stated that the high wax content of the oil reflects terrestrial organic sources and thus an Agbada source. However, Weber and Daukoru, (1975) proposed a deep Akata formation hydrocarbon source and a migration route that includes growth faults.

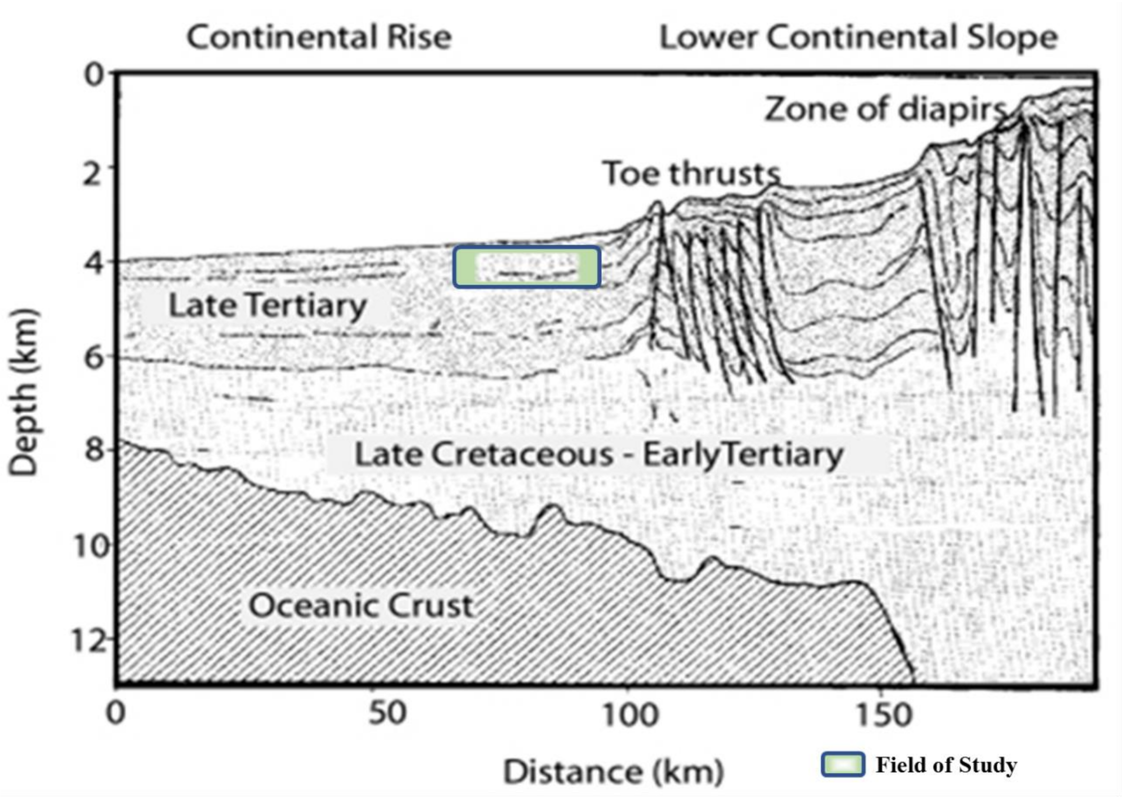

Figure 2.6: Schematic section of depobelt structures. The section from the Niger Delta continental slope and rise showing the result of internal gravity tectonics on sediments at the distal portion of the depobelt. The late Cretaceous-Early Tertiary section has low-velocity gradient, probably marine shales, whereas the Late Tertiary has a normal-velocity gradient, suggesting facies much richer in sand (after Tuttle et al., 1999). The approximate location of the field studied is shown.

2.8 Hydrocarbon Generation and Migration

Several researchers have carried out studies on the hydrocarbon generation and migration in the Niger Delta. Evamy et al., (1978) set the top of the present-day oil window in the Niger Delta at the 240°F (115° C) isotherm. In the northwestern portion of the delta, the oil window (active source-rock interval) lies in the upper Akata formation and the lower Agbada formation as shown in Figure 2.7. To the southeast, the top of the oil window is stratigraphically lower (up to 1,200 ft below the upper Akata/lower Agbada sequence; Evamy et al., 1978). Evamy et al., (1978) argue that generation and migration processes occurred sequentially in each depobelt and only after the entire belt was structurally deformed, implying that deformation in the Northern Belt would have been completed in the Late Eocene. Some researchers (Nwachukwu and

Chukwura, 1986; Doust and Omatsola, 1990; Stacher, 1995) attribute the distribution of the top of the oil window to the thickness and sand/shale ratios of the overburden rock (Benin formation and variable proportions of the Agbada formation.).

The sandy continental sediment (Benin formation) has the lowest thermal gradient (1.3 to 1/8° C/100 m); the paralic Agbada formation has an intermediate gradient (2.7° C/100 m); and the marine, over-pressured Akata formation has the highest (5.5° C/100 m) (Ejedawe et al., 1984). In the youngest depobelts, the effects of shale diapirism becomes increasingly important. Complexly faulted "whale back" features lie above shale ridges in the present coastal swamp and offshore; whereas in the distal belt on the continental slope, diapirs and basins appear to be as important as growth faulting.

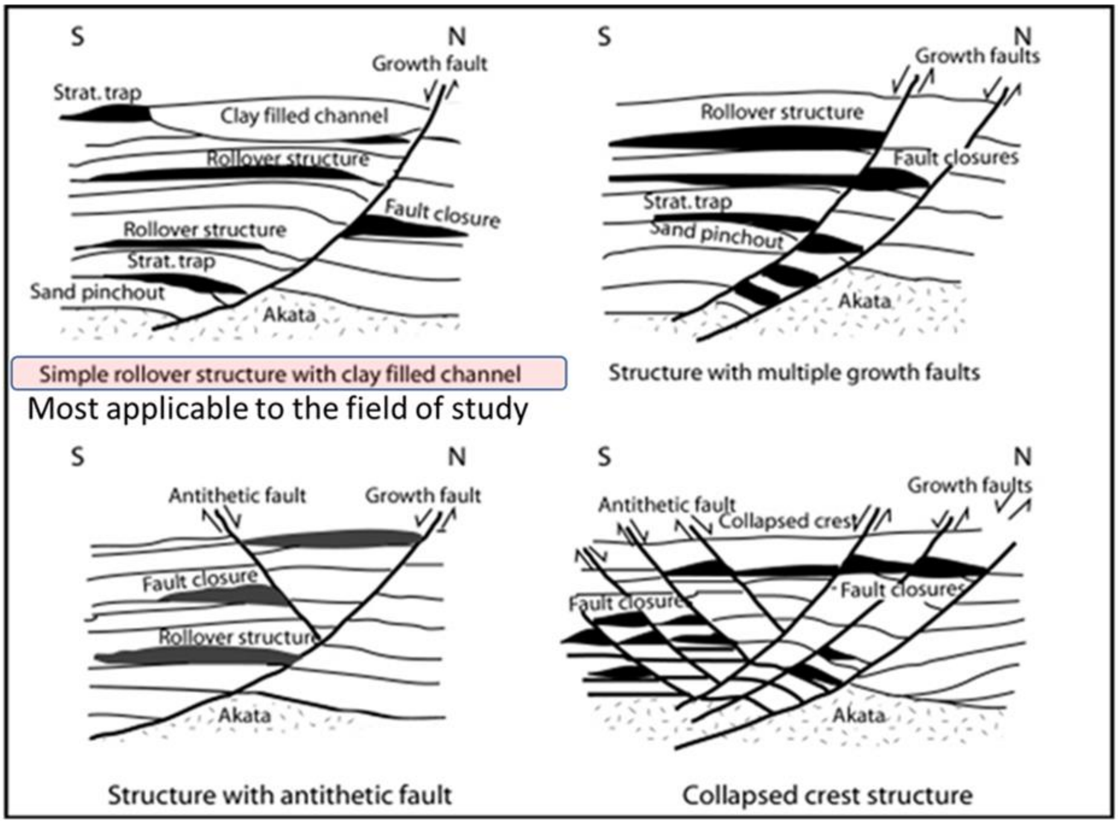

Figure 2.7: Principal types of oilfield structures and associated traps in the Niger-Delta [modified from Weber (1971), Doust and Omatsola (1990) and Stacher (1995)]. The field studied here corresponds to the first trap type.

CHAPTER THREE

SPARSE-LAYER INVERSION

3.1 Introduction

A simple layer is defined as having two reflection coefficients – one at the top and one at the base of the layer. If the reflection coefficients are equal and opposite, they constitute an odd impulse pair. If they are equal and of the same sign, they are an even impulse pair. A single reflection can be represented as an even impulse pair with zero thickness. If the reflection coefficients at top and base of the layer are unequal, they can be uniquely defined as the sum of an even impulse pair and an odd impulse pair (Bracewell, 1965). Any sparse reflectivity series can be represented as the sum of a limited number of odd and even impulse pairs. Sparse-layer inversion essentially extends the seismic bandwidth by inverting for impulse pairs that sum to form the reflectivity series, and harmonically extrapolating the impulse-pair frequency responses.

Within the assumptions of the convolutional model, ignoring such complications as internal multiples and other noises (which are assumed to be otherwise dealt with), the seismic waveform produced by an impulse pair is the convolution of the seismic wavelet and the impulse pair. The seismic waveform produced by any simple layer is thus the sum of even and odd impulse pairs that are convolved with a wavelet. By the principle of superposition, any reflection seismogram, can thus be represented as the sum of even and odd layer responses. Zhang and Castagna (2011) use a wavelet dictionary of pre-defined layer responses and basis pursuit to decompose the seismic trace into the sum of a sparse number of even and odd layer responses. The sum of the corresponding impulse pairs is the inverted reflectivity series. Liang and Castagna (2017) show that this reflectivity series can be filtered to a desired bandwidth, thereby achieving bandwidth extension. The band that can be achieved is determined by trading off validation error against well control and desired resolution.

As discussed by Zhang and Castagna (2011), the advantage of this method is that, unlike sparse-spike inversion, the sparsity constraint does not inherently produce a bias against thin layers. This can be understood by considering the tradeoff between reflection magnitude and layer thickness that can be varied to achieve the same seismic amplitude. A very thin layer with strong reflection coefficients may produce the same amplitude response as a thicker layer with smaller reflection coefficients (Widess, 1973). If sparsity is invoked in the inversion by minimizing the L1 norm (average magnitude) of the inverted reflectivity series, solutions with greater thickness and smaller reflection coefficients will be favored over those with smaller thickness and larger reflection coefficients. In other words, the thin layers with large reflection coefficients have a reflectivity series with a greater average magnitude than thicker layers with smaller reflection coefficients. By minimizing the reflection coefficient magnitude in the inverse solution, thicker layers are favored over thinner layers. Sparse-spike inversion, thus, has difficulty resolving thin layers, and may in fact become unstable laterally when trying to do so.

Sparse-layer inversion, on the other hand, applies the sparsity constraint to the magnitude of the layer responses, not the reflection coefficients. The method thus biases the inversion towards a sparse number of layers – and does not favor any layer thickness over another. Constraints on the layer thickness permitted by the inversion is achieved by limiting the wavelet dictionary to allowable layer thicknesses. It can be readily seen that such an inversion implicitly assumes a blocky earth model. Liang and Castagna (2017) show that violation of this assumption results in erroneous bandwidth extension. However, to the degree that this assumption holds, they conclude that some seismic bandwidth extension is achievable; the amount that can be achieved being a function of the seismic data quality and the blocky impedance structure of the earth.

3.2 Synthetic Tie

For this dataset in the deep offshore Niger Delta, bandwidth extension via sparse-layer inversion seriously degrades the correlation coefficient of the synthetic tie (Figure 3.1). A variety of factors may explain this reduction (a) noise amplification (b) deviation from a blocky earth impedance structure (c) errors in well log reflectivity becoming more significant at higher frequencies (d) deviation from the convolutional model (e) imperfect wavelet estimation, and (f) errors in the time-depth function and well position having a greater influence on the correlation at higher frequency. Given the lack of an adequate well tie for the bandwidth-extended data – it is unlikely that the data would be amenable to accurate quantitative seismic inversion. For our purposes of delineation, it will be enough to determine if the bandwidth-extended data can better reveal and resolve thin oil-bearing sands for interpretation purposes.

(a)

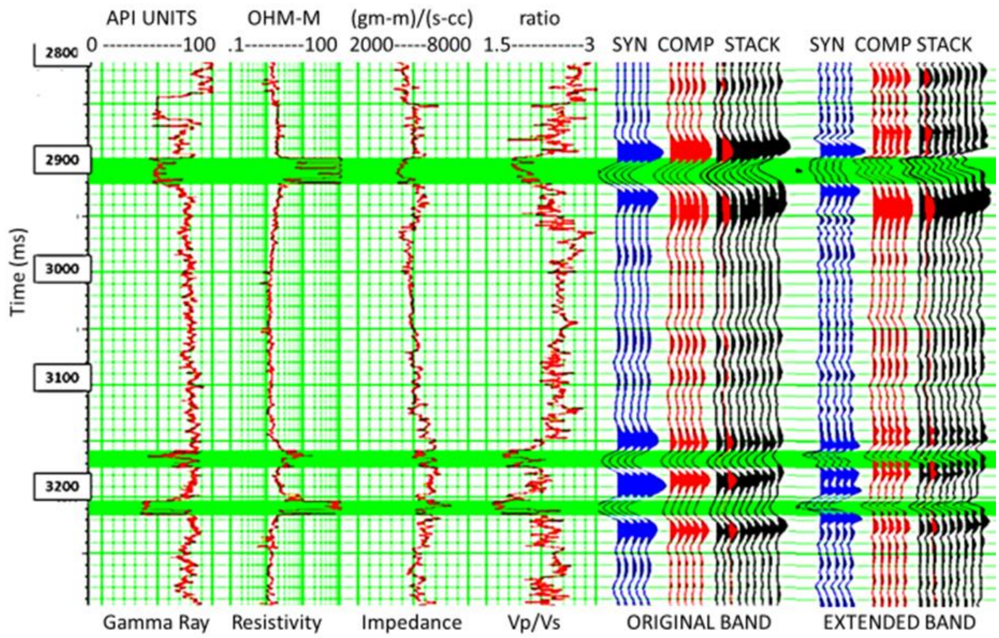

Figure 3.1(a) Well logs and synthetic ties for original and bandwidth-extended near-trace stacks that have been integrated to approximate band-limited seismic impedance. Wavelets used are shown in Figure 3.2. Dark green vertical intervals are interpreted reservoir intervals. Synthetic traces are shown in blue and labelled SYN, extracted average of nearest neighbor traces are shown in red and labelled COMP, and real stacked seismic bandlimited impedance traces in the vicinity of the well are in black.

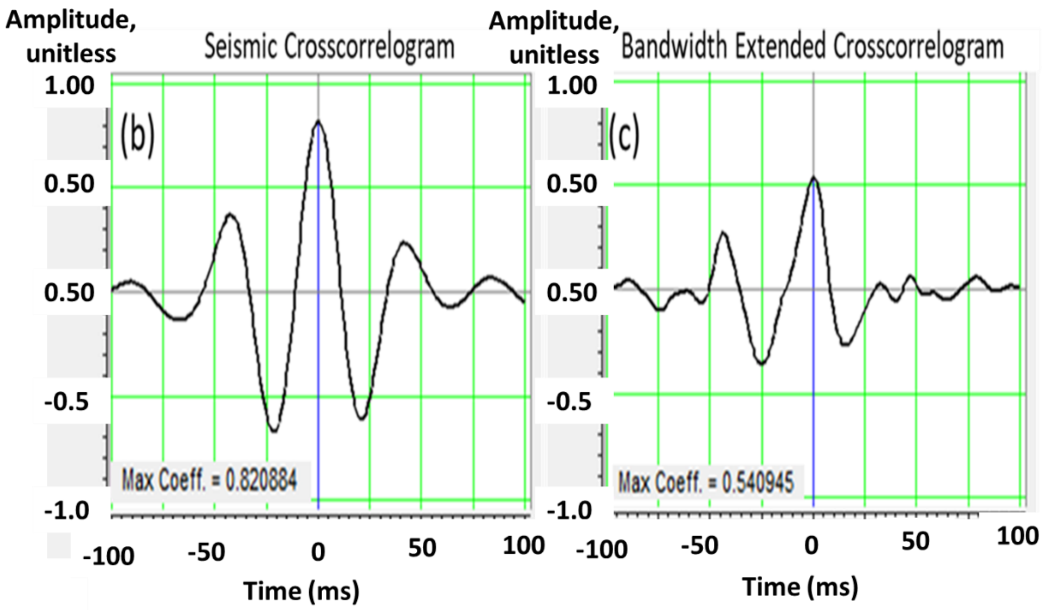

Figure 3.1 (b) Original seismic and (c) bandwidth-extended crosscorrelograms for the entire seismic window. Time equal to zero corresponds to no time shift between the synthetic and the composite seismic trace.

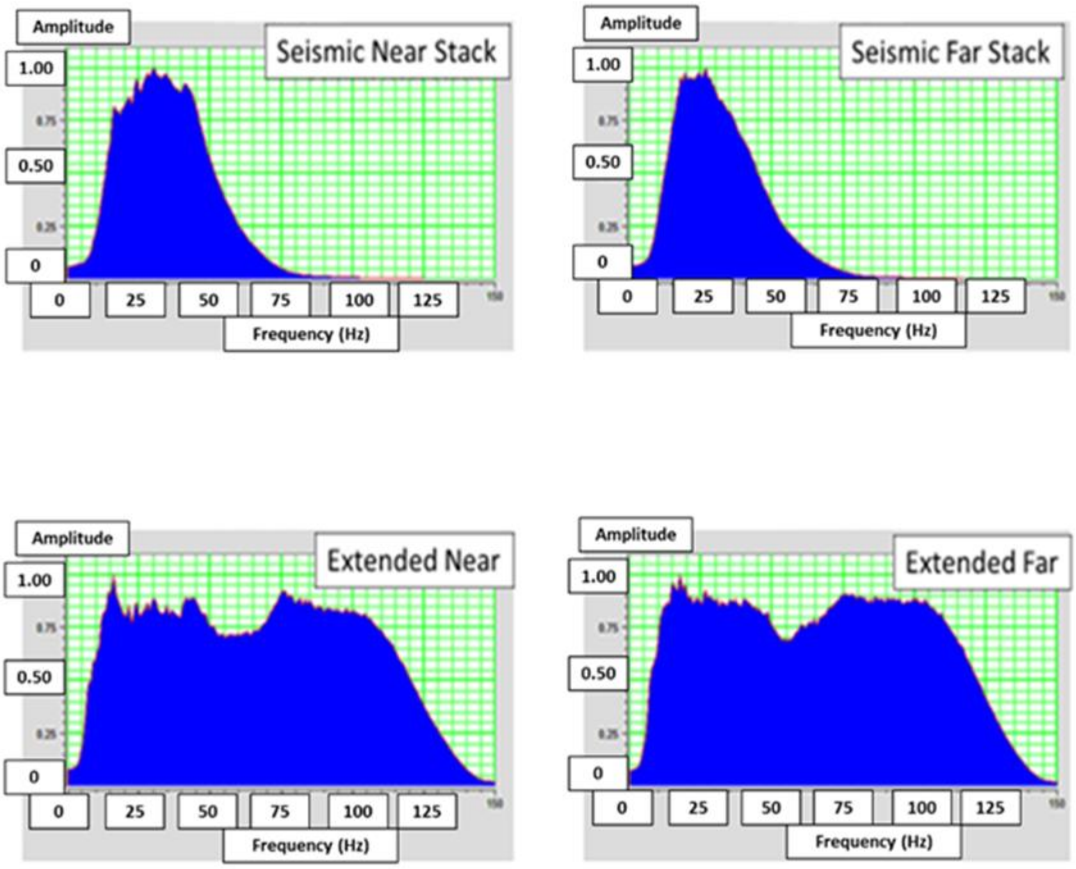

Figure 3.2: Average spectra over the seismic volumes for a time-window from 2.5 s to 3.5 s for near stack, far stack, bandwidth-extended near stack and bandwidth-extended far stack.

3.3 Resolvability of target bodies

The reservoir sandstone in a typical well in the field of study has an approximate average velocity of 9,000 ft/sec (Figure 3.3). At the position of the B02 sandstone, the dominant frequency on conventional seismic was about 25 Hz (Figure 3.1), while it can be significantly increased on the bandwidth-extended data (Figure 3.2). At the conventional band with 25 Hz dominant frequency, this 40 ft sandstone is below the tuning thickness of 90 ft. However, by increasing the dominant frequency in the bandwidth-extended data, this sandstone was resolved.

The Widess tuning-thickness is thus: ¼*(9000 ft/s / 25 Hz) = 90 ft. Consider a 40 ft thickness to be equal to the quarter wavelength, ʎ/4, accurate resolution of a layer with this velocity would require a dominant frequency of 9000 ft/s / (4 *40 ft) = 56.25 Hz.

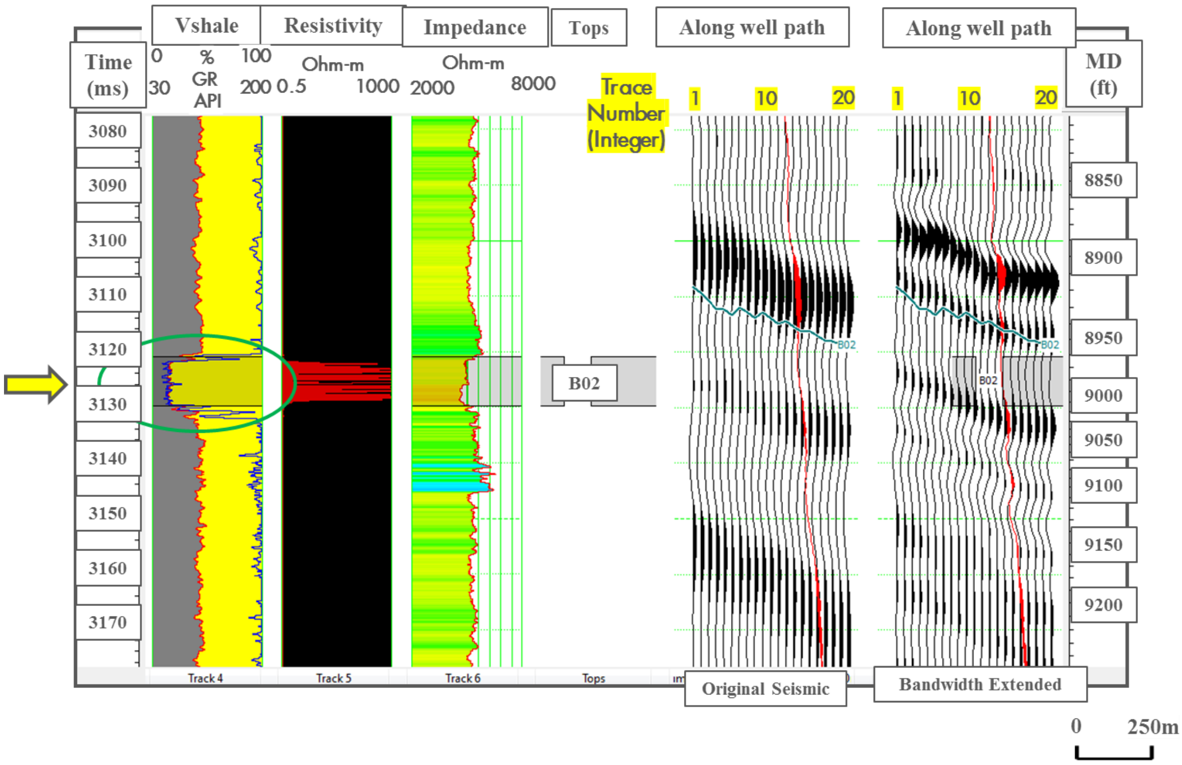

Figure 3.3: Comparing resolvability of B02 sandstone in original seismic and bandwidth extended seismic data.

3.4 Results

The value of bandwidth extension for reservoir characterization in this field is well illustrated in Figures 3.4a and 3.4b which shows near-and far stack data before and after bandwidth extension for a pay interval that was not resolved on the original seismic. There is no indication of the multiple sands seen in logs evident on the seismic but clearly two sand lobes on gamma-ray and resistivity logs. On the other hand, the bandwidth extension readily indicates thin layer responses from each of the two dominant sands. In fact, the bandwidth extended reflection from the upper sand is dimmer at the well, corresponding to it being the thinner of the two intervals, but brightens away from the well; suggesting that thickening and/or better reservoir quality of that unit could potentially be found in an alternative location.

Furthermore, as the two events associated with the reservoir are tracked up-dip to the right, the reflections coalesce as overall amplitudes dim, suggesting that the upper sand pinches out up-dip. Clearly, such a detailed interpretation of the internal reservoir architecture would not be possible on the single event evident on seismic data prior to bandwidth extension.

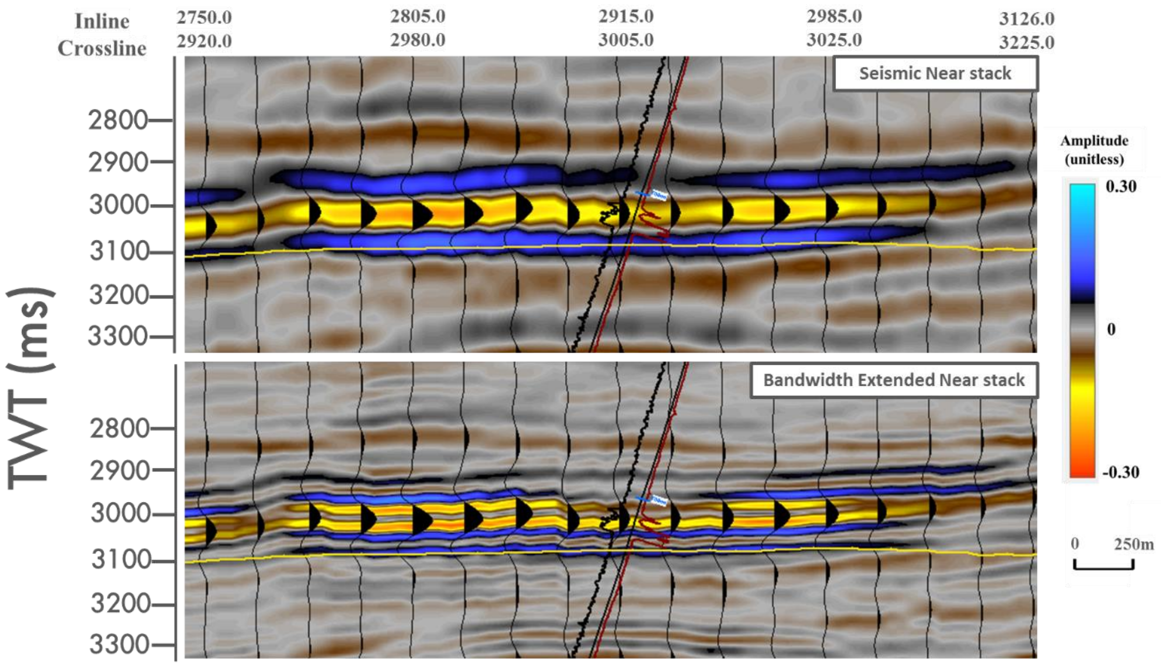

Figure 3.4a: Near-stack data before (top and variable area wiggles) and after (bottom) bandwidth extension for a reservoir interval seen on well logs. The well logs are gamma-ray (black) and resistivity (brown). The color scale is relative.

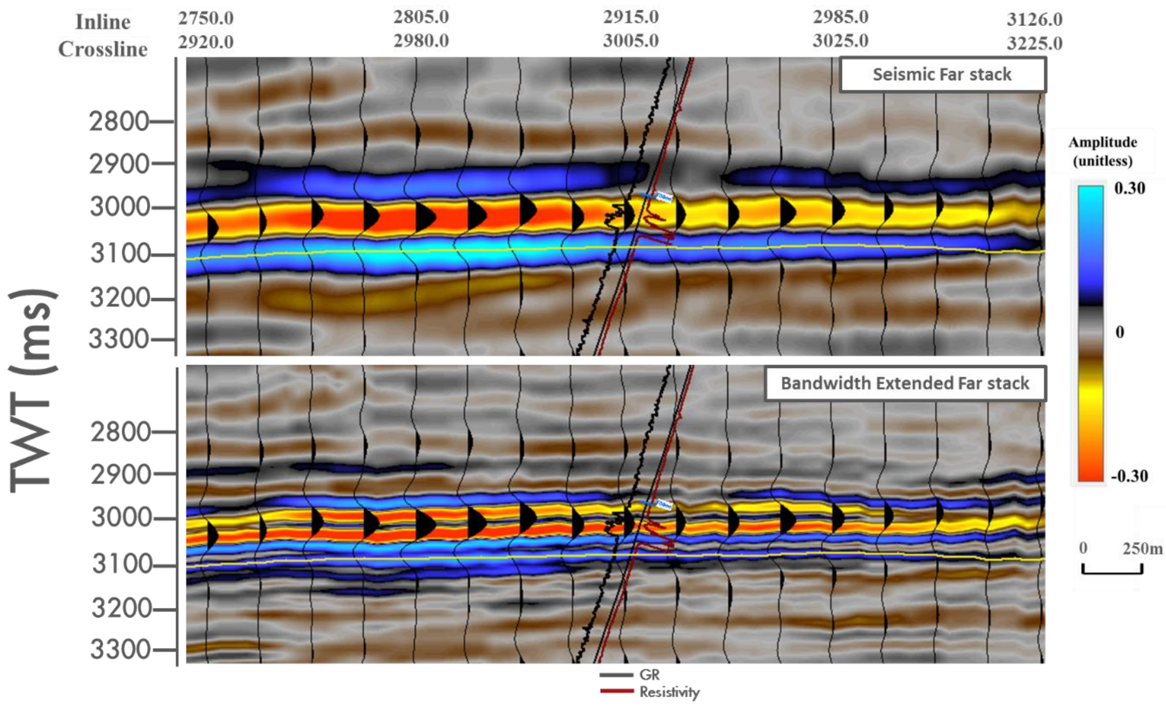

Figure 3.4b: Far-stack data before (top and variable area wiggles) and after (bottom) bandwidth extension for a reservoir interval seen on well logs. The well logs are gamma-ray (black) and resistivity (brown). The color scale is relative.

The black diagonal line represents the exact well position. The resistivity log (brown curve) increases to the right and the gamma-ray log (black curve) decreases to the left. The logs show a single reservoir interval with a thin unit at the top and a thicker one at the bottom separated by a thin shale. The original seismic data shows no indication of two sands while this is evident on the spectrally-broadened data. An interpreted slight time-depth error not apparent at the original seismic frequency between the logs and seismic is not corrected to preserve the integrity of the data.

Figure 3.5 illustrates the relationship between reservoir thickness and seismic response for both original seismic and spectrally broadened data. Figure 3.5a shows the original near trace stack and well logs for a deviated well with multiple pay intervals. The deepest and thickest pay interval is readily seen on resistivity and gamma-ray logs. The sand thickness evident on the well logs is less than a half period and thus, sub-tuning. The seismic response is the classic soft-over-hard response one would expect from such a thin layer in this area. Shallower near-offset amplitudes are not always obviously related to overlying thin pay intervals.

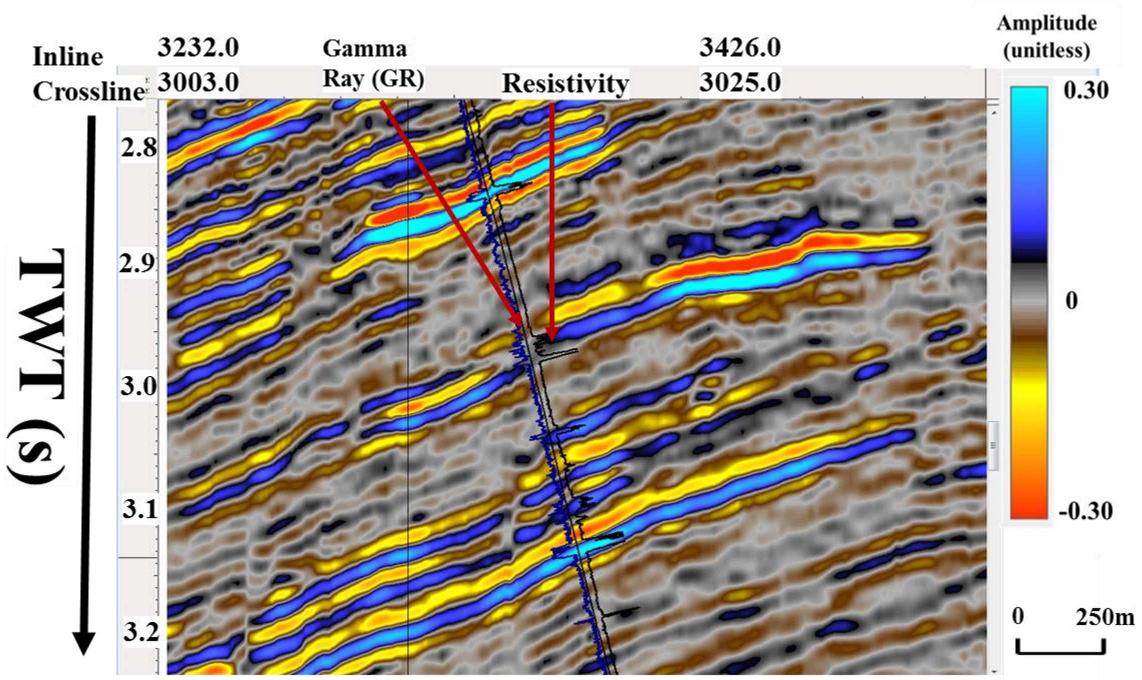

Figure 3.5a: Near-offset stack and deviated well with several reservoir levels. The well bore position is the straight black solid line between the well logs. The rightmost well log is resistivity, with high resistivities indicative of pay being excursions to the right. The gamma-ray log is on the left, with low gamma-ray counts being excursions to the left. On the seismic line, reds and yellows are soft reflections and blues are hard reflections. The amplitude scale is relative and unitless.

The conventional seismic far offset stack (Figure 3.5b) has a clearer relationship between amplitude and reservoir sands, which all exhibit soft-over-hard responses. Notably, no events appear where no reservoir is evident on the logs.

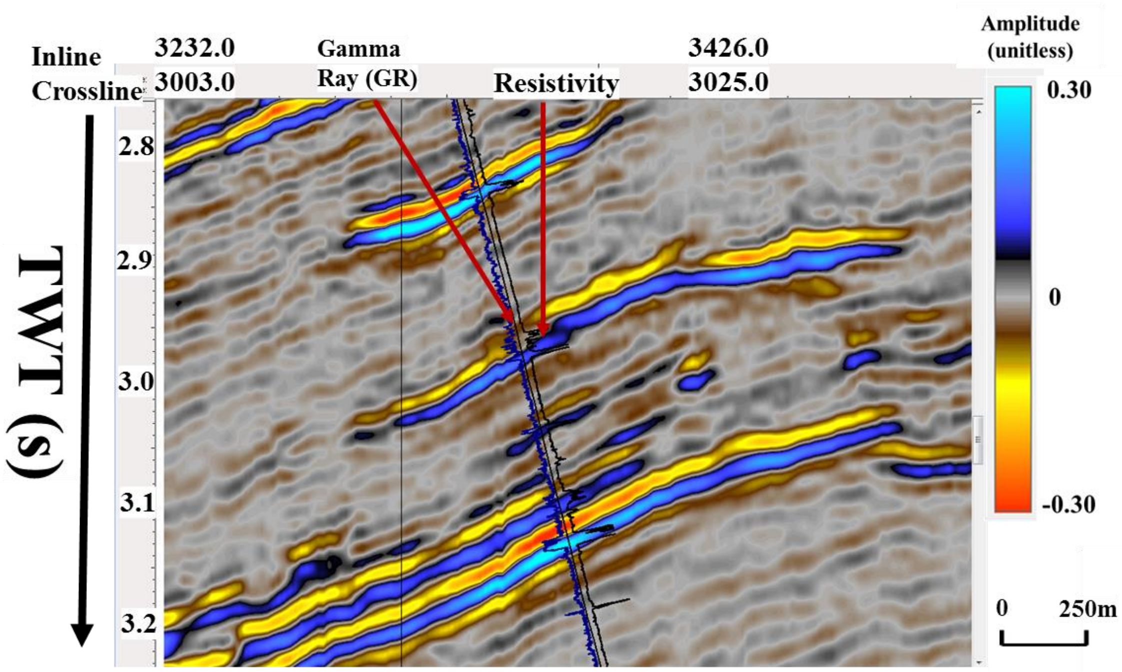

Figure 3.5b: Far-offset stack and deviated well with several reservoir levels. The well bore position is the straight black solid line between the well logs. The rightmost well log is resistivity, with high resistivities indicative of pay being excursions to the right. The gamma-ray log is on the left, with low gamma-ray counts being excursions to the left. On the seismic line, reds and yellows are soft reflections and blues are hard reflections. The amplitude scale is relative and unitless.

The bandwidth-extended near stack (Figure 3.5c) shows a distinct soft (red and yellow) event near the top of the deepest reservoir sand and a strong hard event (light blue) at the base of the sand. These lose amplitude updip suggesting that the sand has thinned updip to below the high-frequency tuning thickness. Overlying thin reservoirs have associated reflectivity which increases away from the well – suggesting perhaps an unfortunate well position relative to these shallower reservoir units.

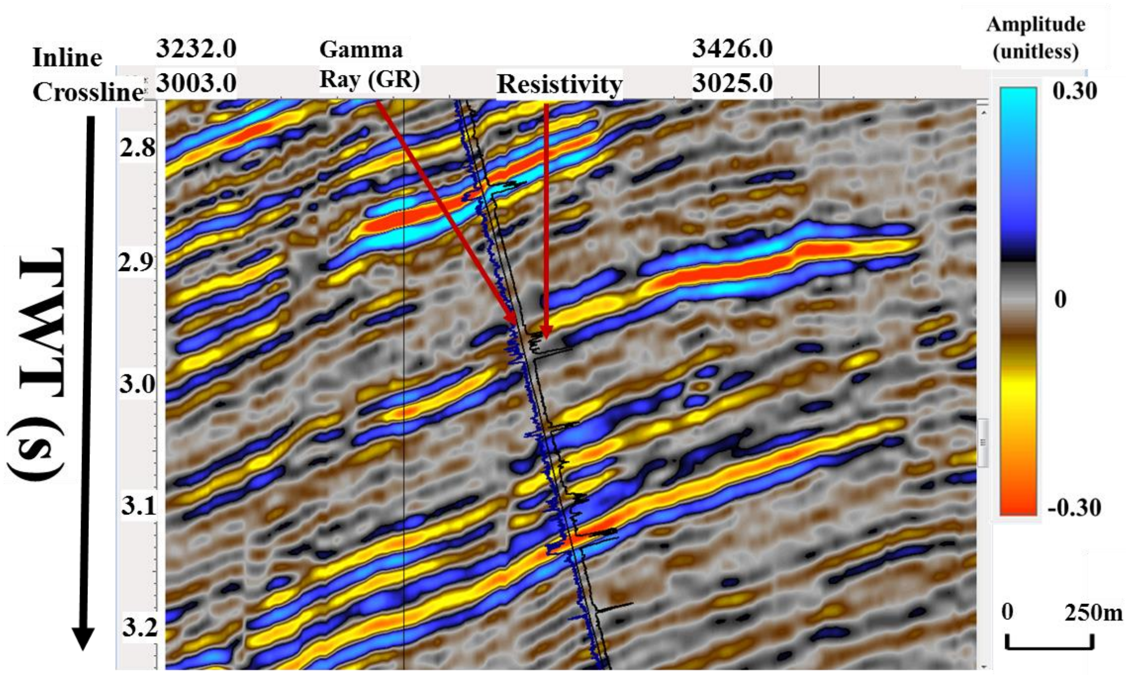

Figure 3.5c: Bandwidth extended near-offset stack and deviated well with several reservoir levels. The well bore position is the straight black solid line between the well logs. The rightmost well log is resistivity, with high resistivities indicative of pay being excursions to the right. The gamma-ray log is on the left, with low gamma-ray counts being excursions to the left. On the seismic line, reds and yellows are soft reflections and blues are hard reflections. The amplitude scale is relative and unitless.

The bandwidth-extended far-offset stack (Figure 3.5d) shows strong soft-over-hard amplitudes associated with every thin pay zone. As with the near-offset stack, a strong soft reflection (red) occurs at the top of the deepest pay and a strong hard reflection (light blue) occurs at the base; however, relative to the logs, the time thickness seems to be over-estimated. It is unclear whether this is due to an inadequate time-depth function or a failure of the sparse-layer inversion to resolve the layer. Nevertheless, the distinct events at top and base appear to be coalescing to a single soft-over-hard response updip as would occur if the interval were thinning.

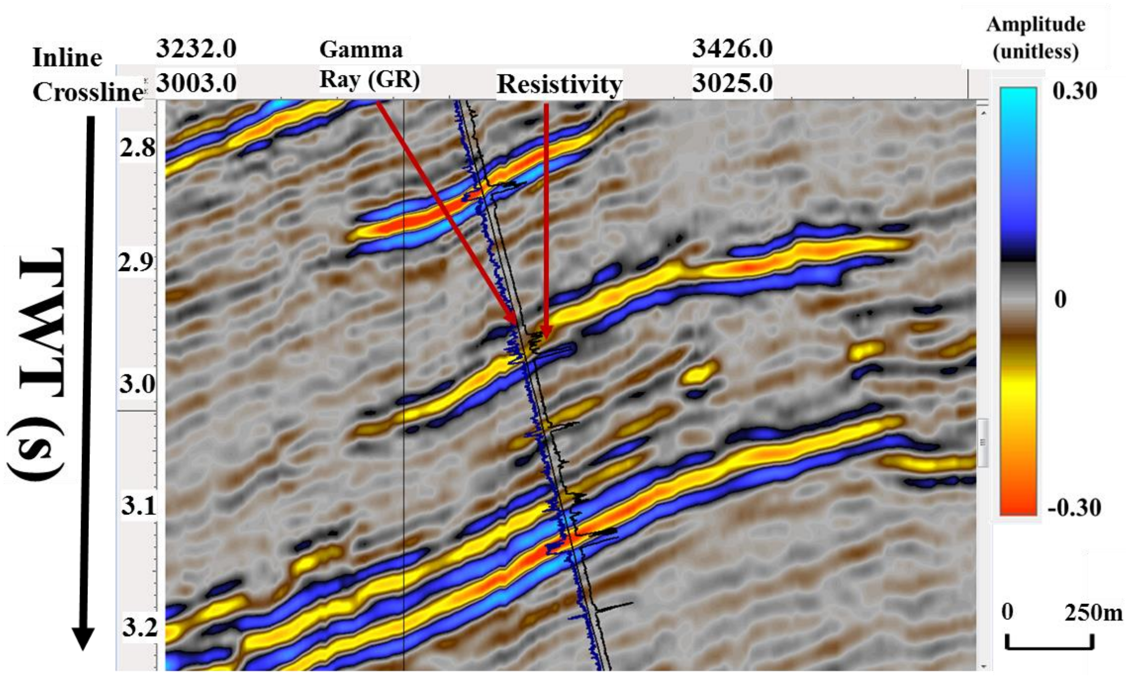

Figure 3.5d: Bandwidth-extended far-offset stack and deviated well with several reservoir levels. The well bore position is the straight black solid line between the well logs. The rightmost well log is resistivity, with high resistivities indicative of pay being excursions to the right. The gamma-ray log is on the left, with low gamma-ray counts being excursions to the left. On the seismic line, reds and yellows are soft reflections and blues are hard reflections. The amplitude scale is relative and unitless.

CHAPTER FOUR

PHASE DECOMPOSITION

4.1 Introduction

One of the objectives of phase decomposition is to better identify hydrocarbon related anomalous behavior. Theoretically, a sub-tuning isolated low-impedance reservoir interval should be particularly anomalous on the -90° phase component. For a zero-phase seismic wavelet, an isolated step interface should appear on the zero (hard) or 180° (soft) phase components.

Castagna et al., (2016) introduced phase decomposition as a direct hydrocarbon indicator. Figure 4.1 from their paper shows a seismogram decomposed into a phase gather where amplitude is mapped as a function of seismic record time and event response phase. The phase gather traces sum to reproduce the original seismic trace. A hydrocarbon reservoir at 1400 ms record time is a bright spot (high negative amplitude) caused by the low impedance of the reservoir relative to surrounding shales. The phase decomposition shows the amplitude of these events occurring at -100° phase.

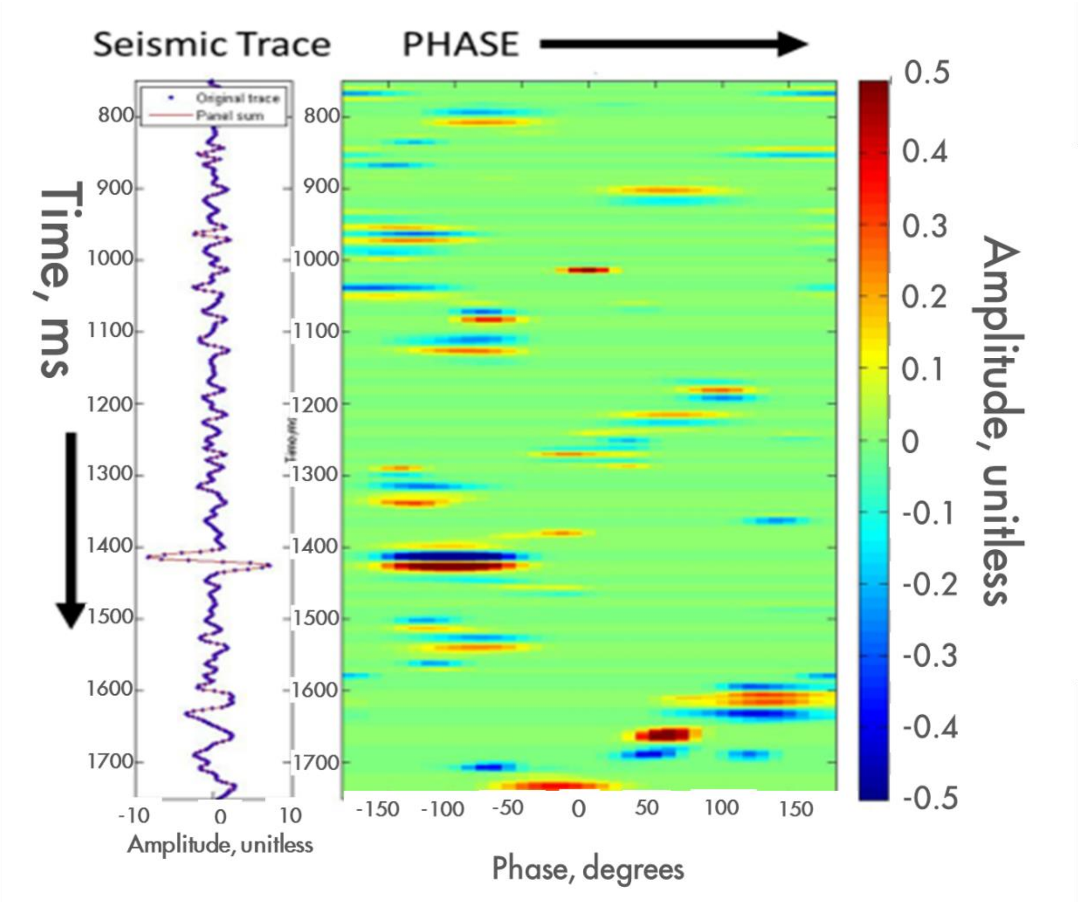

Figure 4.1: A seismic trace (blue points in left track) is decomposed into a time-phase analysis (phase gather) where amplitude is mapped as a function of time and event response phase (modified from Castagna et al., 2016). The phase gather sums to form the seismic trace (red line).

The difference between the hydrocarbon response, and the response of the same rock frame filled entirely with brine, is called the hydrocarbon effect, ΔH. As shown schematically in Figure 4.2, no matter what the phase of the reservoir (gas or light oil) and non-reservoir (brine) responses, the hydrocarbon effect is -90° for thin layers at and below seismic tuning because the reservoir impedance is always less than the impedance of the same rock filled completely with brine.

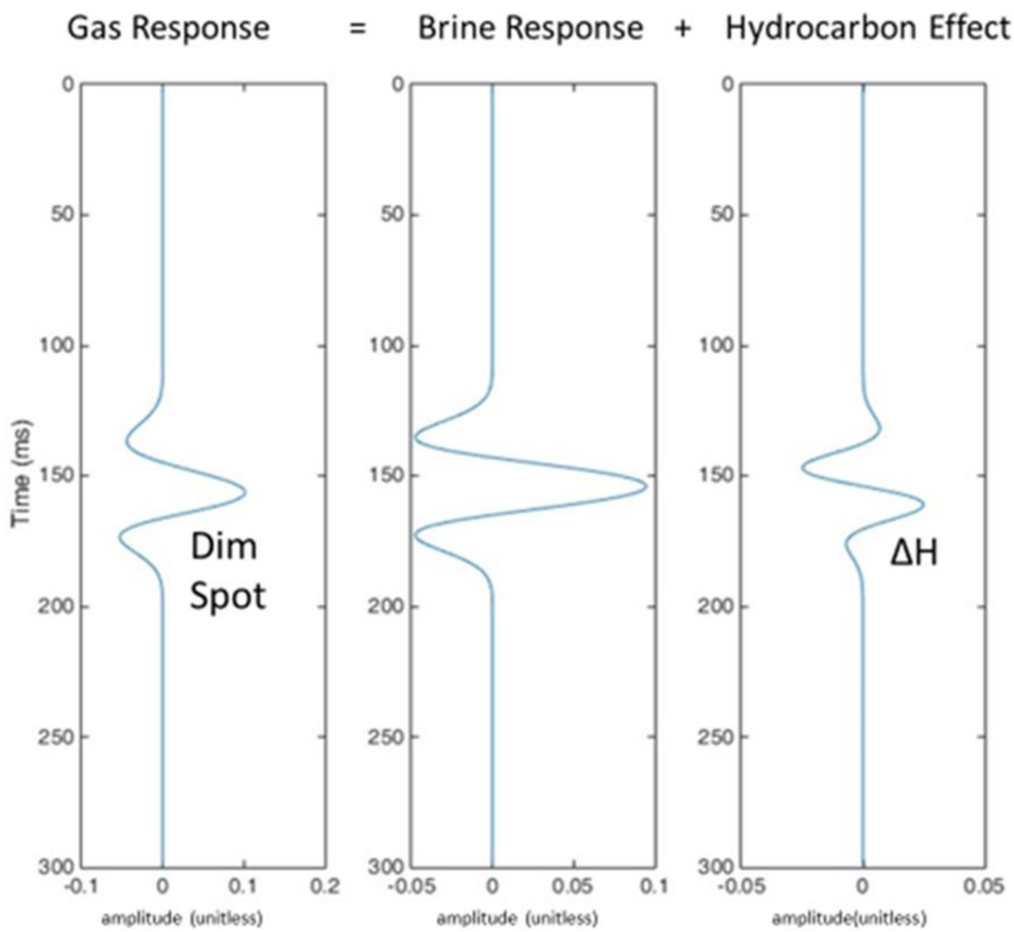

Figure 4.2: Schematic illustration of the hydrocarbon effect ΔH which is the gas-sand response minus the brine-sand response and is always -90° for thin layers.

As a result, the -90° phase component makes an effective attribute to discriminate bright spots that have the correct phase to be caused by hydrocarbons from high amplitudes with the wrong phase to be caused by hydrocarbons. This is evident in Figure 4.3 modified from Castagna, et al., 2016, where, for bright spots, the -90° phase component eliminates amplitudes that cannot be hydrocarbon-filled reservoir and passes only amplitudes that have the right phase to be caused by hydrocarbons.

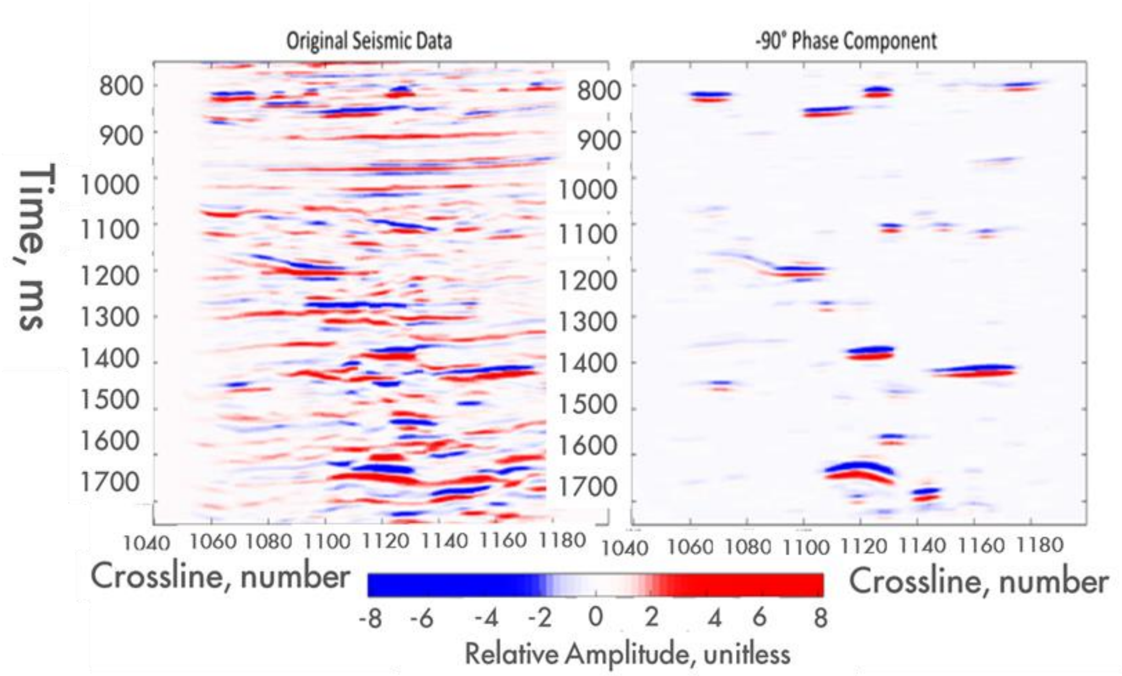

Figure 4.3: Phase decomposition in a Gulf of Mexico shelf gas field. The -90° phase component passes amplitude responses that could potentially be caused by hydrocarbons (modified from Castagna et al., 2016).

The hydrocarbon effect is always -90° because the change in the phase of the layer reflectivity is always -90°. This is shown in Figures 4.4a, 4.4b, and 4.4c for various reservoir and non-reservoir reflection coefficient pairs for the case of bright spots, dim spots, and polarity reversals.

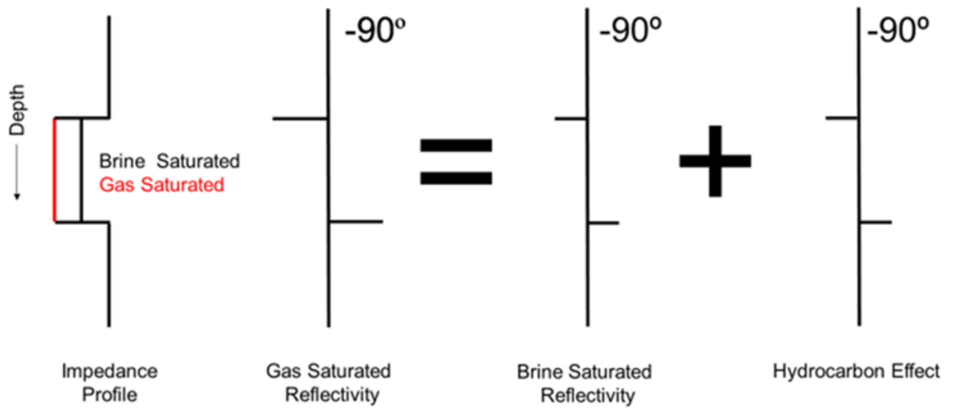

Figure 4.4a: Schematic diagram showing bright-spot hydrocarbon effect for thin layer reflectivity. Scales are all relative and unitless.

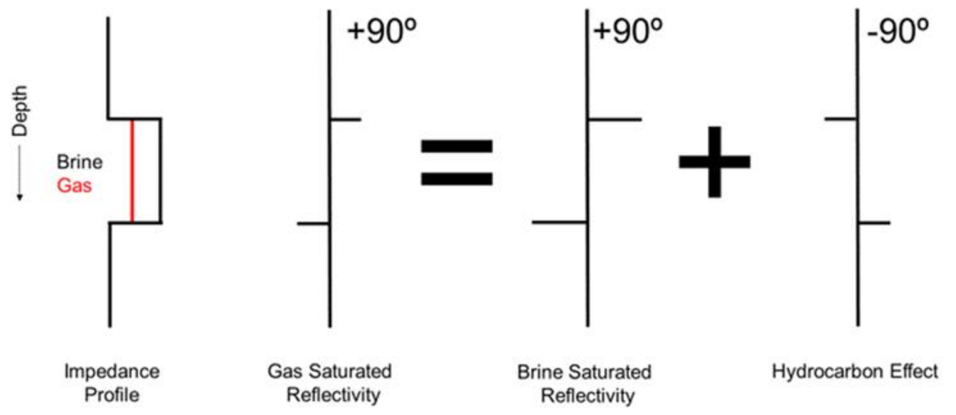

Figure 4.4b: Schematic diagram showing dim-spot hydrocarbon effect for thin-layer reflectivity. Scales are all relative and unitless.

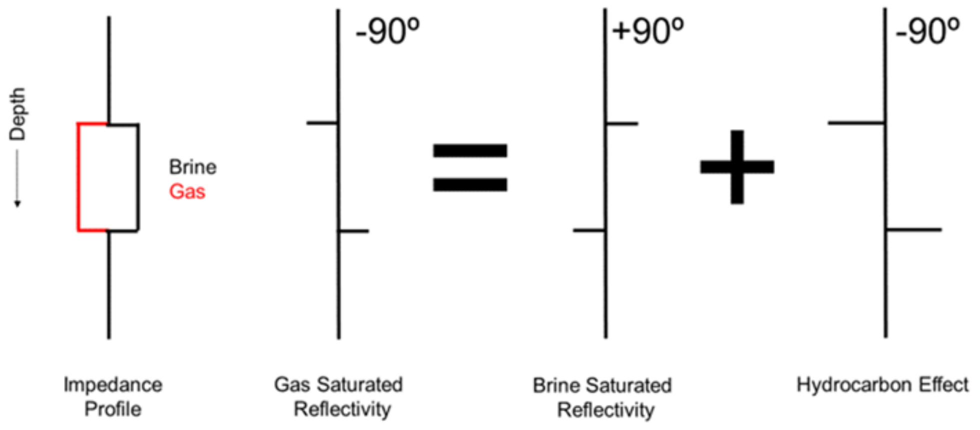

Figure 4.4c: Schematic diagram showing polarity-reversal hydrocarbon effect for thin-layer reflectivity. Scales are all relative and unitless.

4.2 Well Synthetics

The concept of phase decomposition on original and bandwidth-extended dataset in two different well logs are as shown in Figures 4.5 & 4.6. Figure 4.5a depicts the phase decomposition analysis on original seismic data while Figure 4.5b shows the phase decomposition analysis on the same well on a bandwidth-extended seismic data. Similarly, Figures 4.6a and 4.6b illustrate phase decomposition analysis on another well B for original seismic data and bandwidth-extended seismic data respectively. The hydrocarbon effect is always -90° because the change in the phase of the layer reflectivity is always -90°.

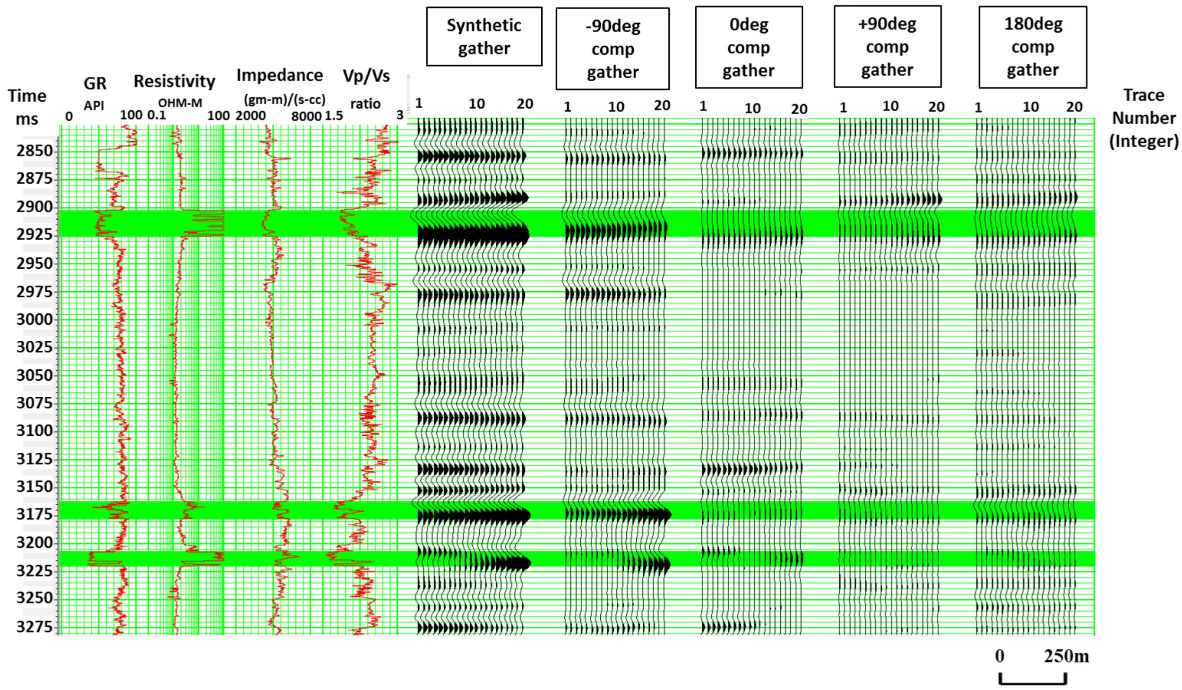

Figure 4.5a: Phase Decomposition Analysis on original seismic data of Well type A.

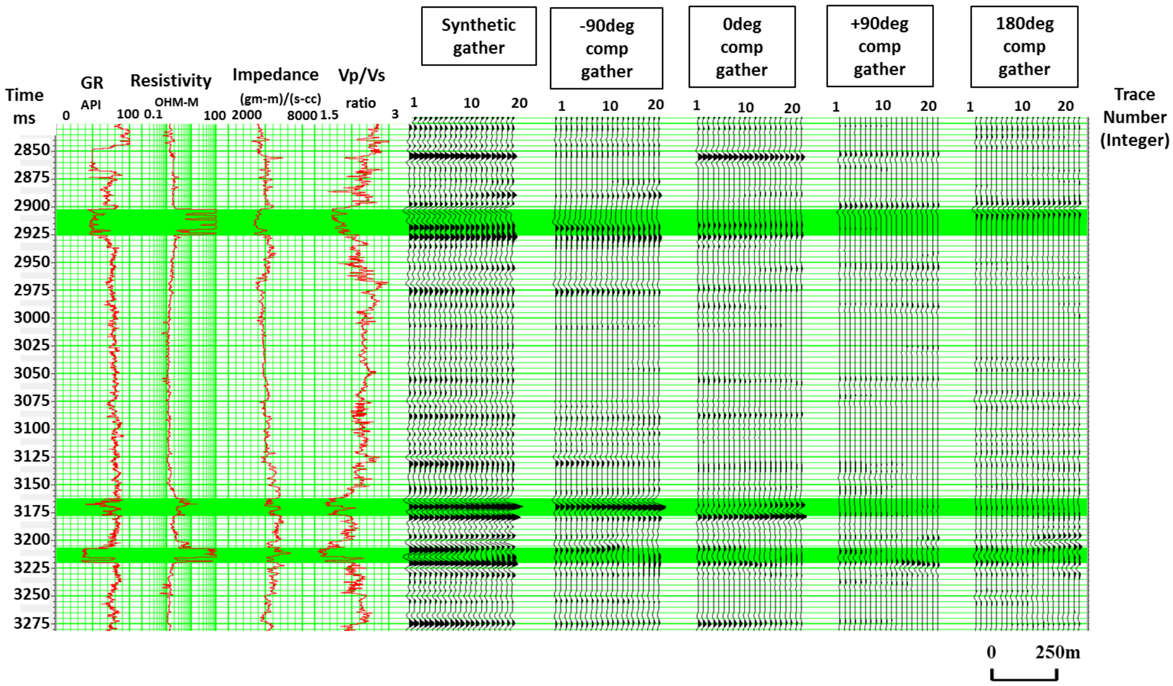

Figure 4.5b: Phase Decomposition Analysis on bandwidth-extended seismic data of Well type A.

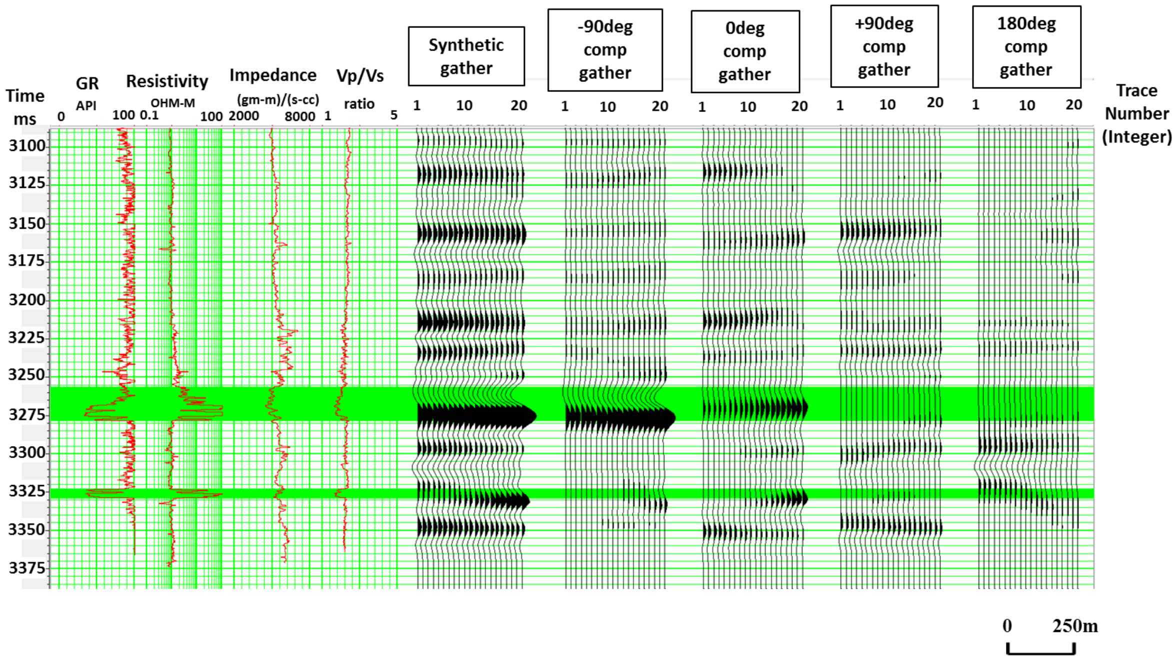

Figure 4.6a: Phase Decomposition Analysis on original seismic data of Well type B.

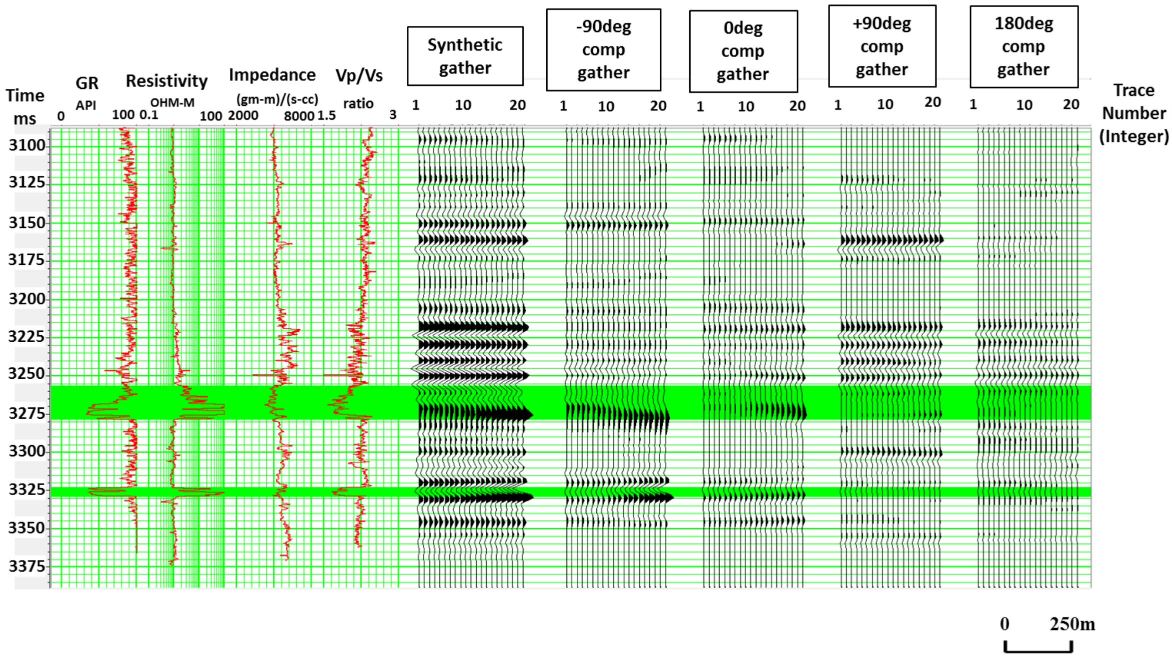

Figure 4.6b: Phase Decomposition Analysis on bandwidth-extended seismic data of Well type B.

4.3 Results

Figure 4.7b shows the zero-phase component (hard symmetrical responses) for the original seismic data near stack. Except the bases of the shallowest and deepest reservoir interval, there is little indication of hard step increases in impedance. Similarly, there is little indication of soft step decreases in impedance on the 180° phase component (Figure 4.7a). This is consistent with the geological picture of thin low-impedance sands encased in shale. However, the -90° response responds strongly to the deepest reservoir at the well (Figure 4.7d). The very thin shallower reservoirs seen in the well do not have associated -90° responses at the well; but the -90° component exhibits stronger nearby responses suggesting possibly more optimal well locations to exploit these units. The +90° component (Figure 4.7c) suggests only minor localized thin hard layers in this window.

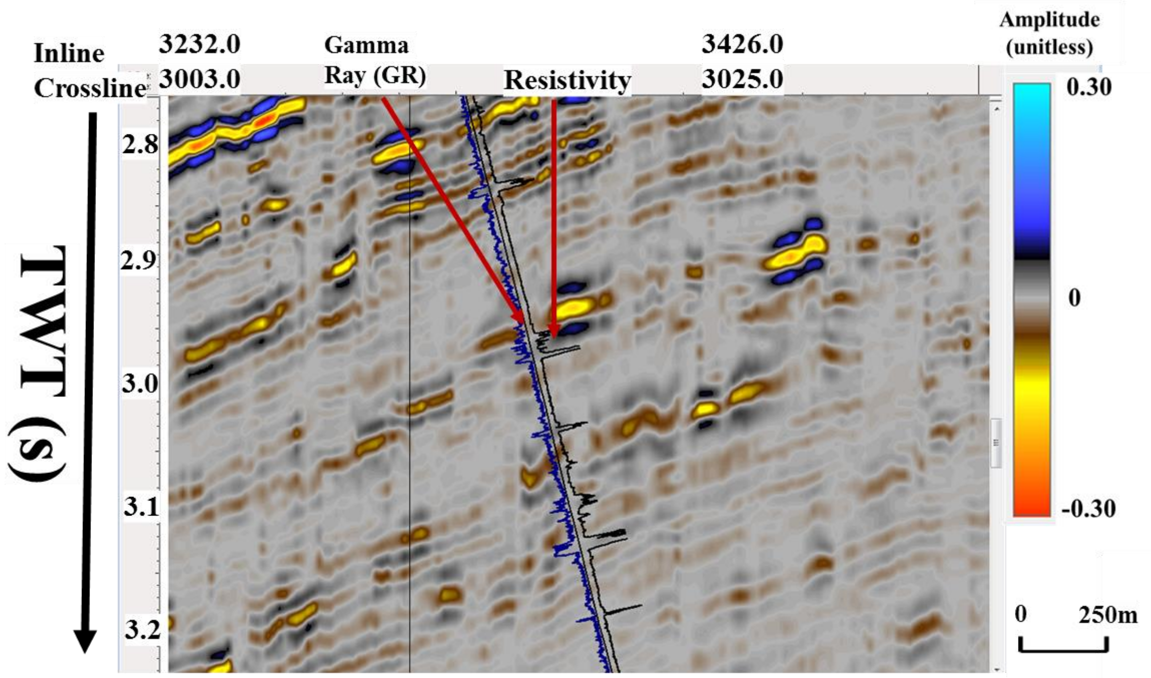

Figure 4.7a: 180° phase component of the original near stack. There are only localized apparent strong step decreases in impedance. The amplitudes are relative and unitless.

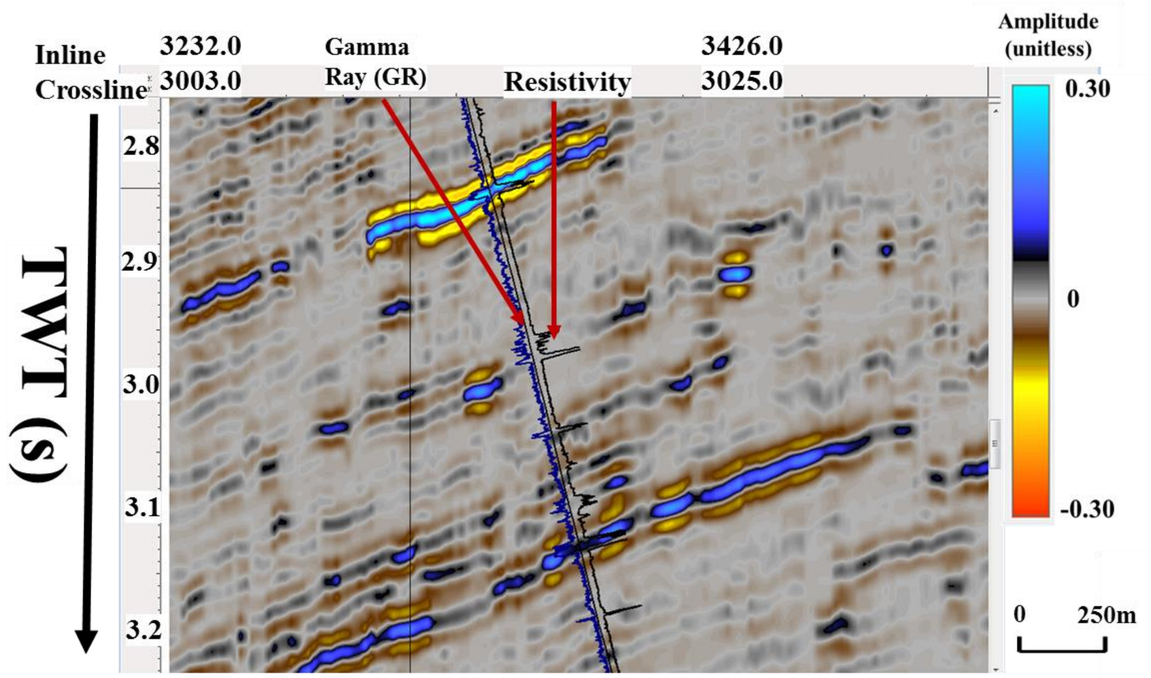

Figure 4.7b: 0° phase component of the original near stack. The base of the shallowest and deepest reservoirs are the only significant step increases in impedance that have significant lateral extent. The amplitudes are relative and unitless.

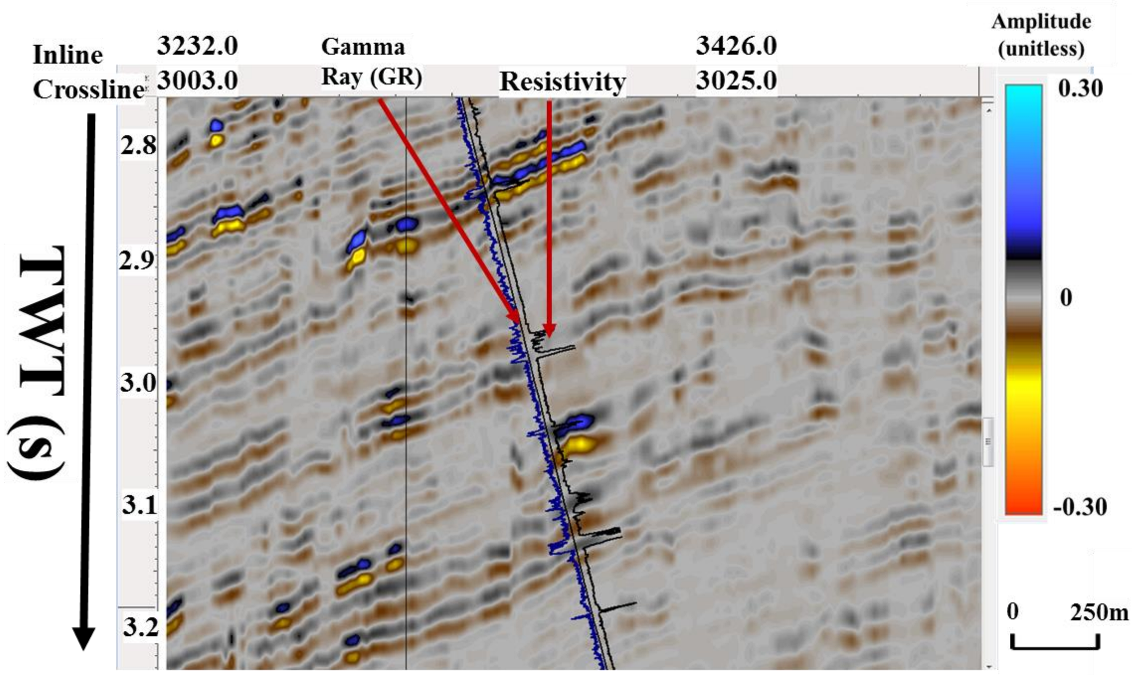

Figure 4.7c: +90° phase component of the original near stack. At the well, this phase attribute only highlights the deepest (and thickest) pay interval. However, for the very thin overlying layers it suggests more optimal nearby well locations that may encounter more significant pay. The amplitudes are relative and unitless.

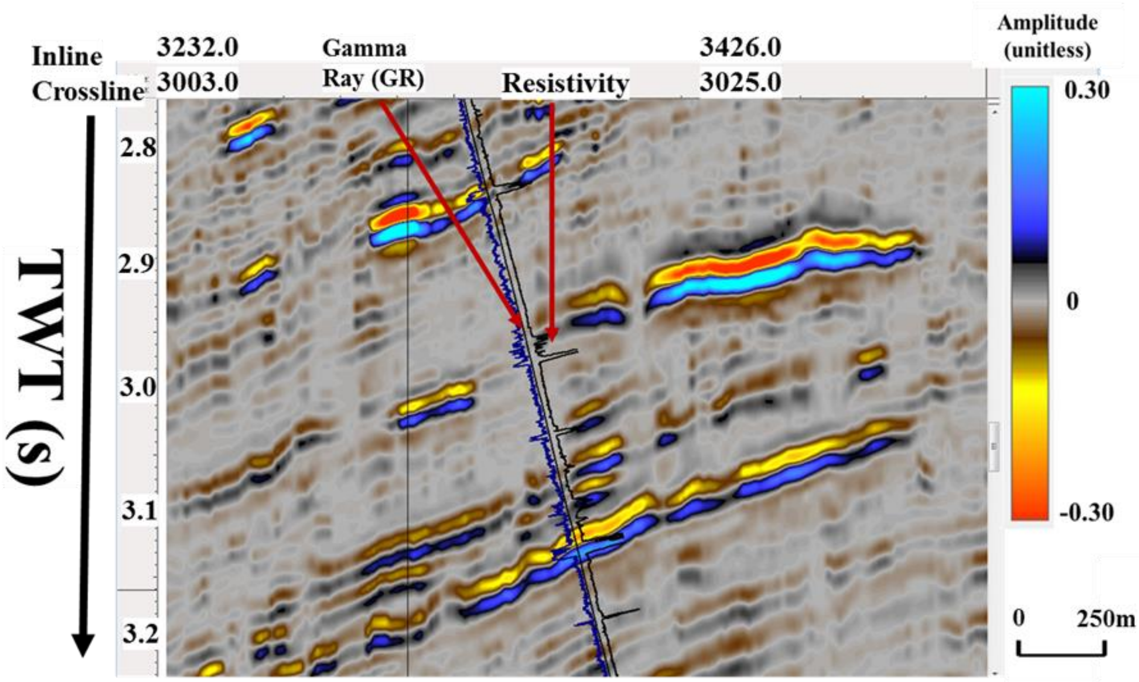

Figure 4.7d: -90° phase component of the original near stack suggesting only minor or highly localized thin hard layers. The amplitudes are relative and unitless.

Similar observations can be made on the far-offset stack phase components where the -90° phase component (Figures 4.8a-d) shows a strong response to hydrocarbons. Notably, at the well location, only known reservoirs exhibit significant amplitudes.

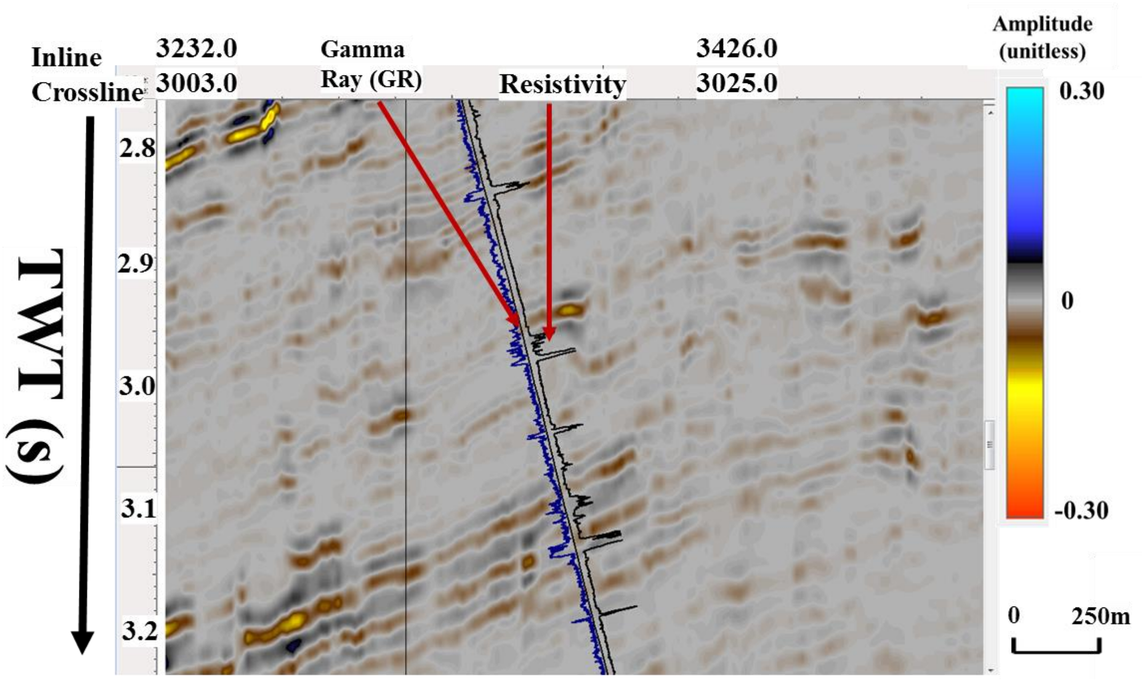

Figure 4.8a: 180° phase component of the original far stack. There are only localized apparent strong step decreases in impedance. The amplitudes are relative and unitless.

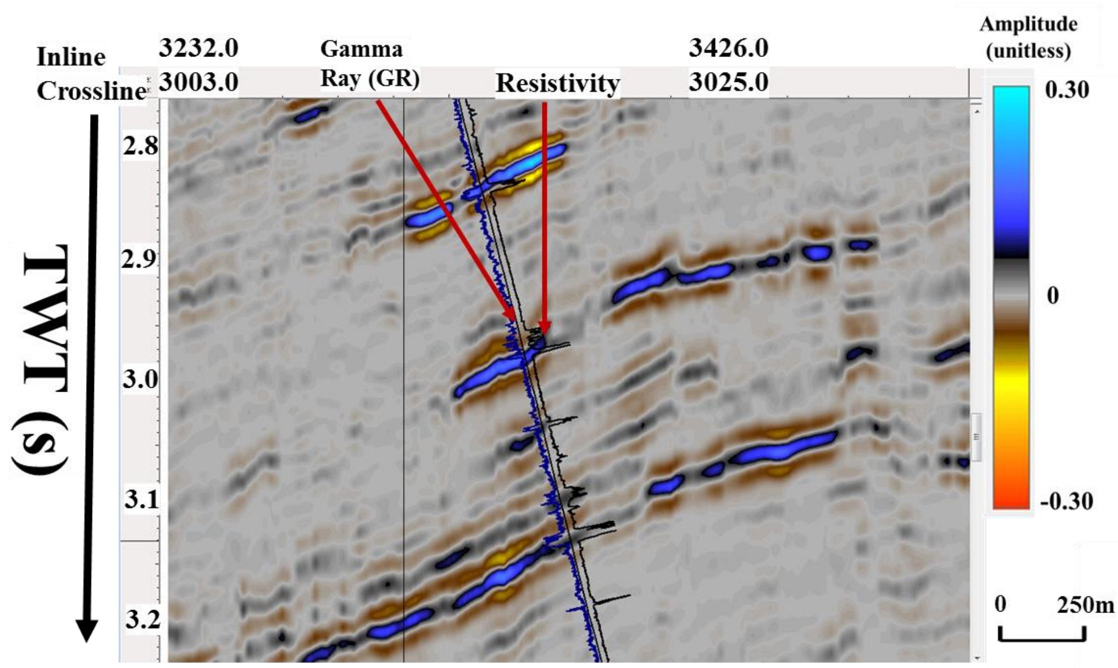

Figure 4.8b: 0° phase component of the original far stack. There are only localized apparent strong step decreases in impedance. The amplitudes are relative and unitless.

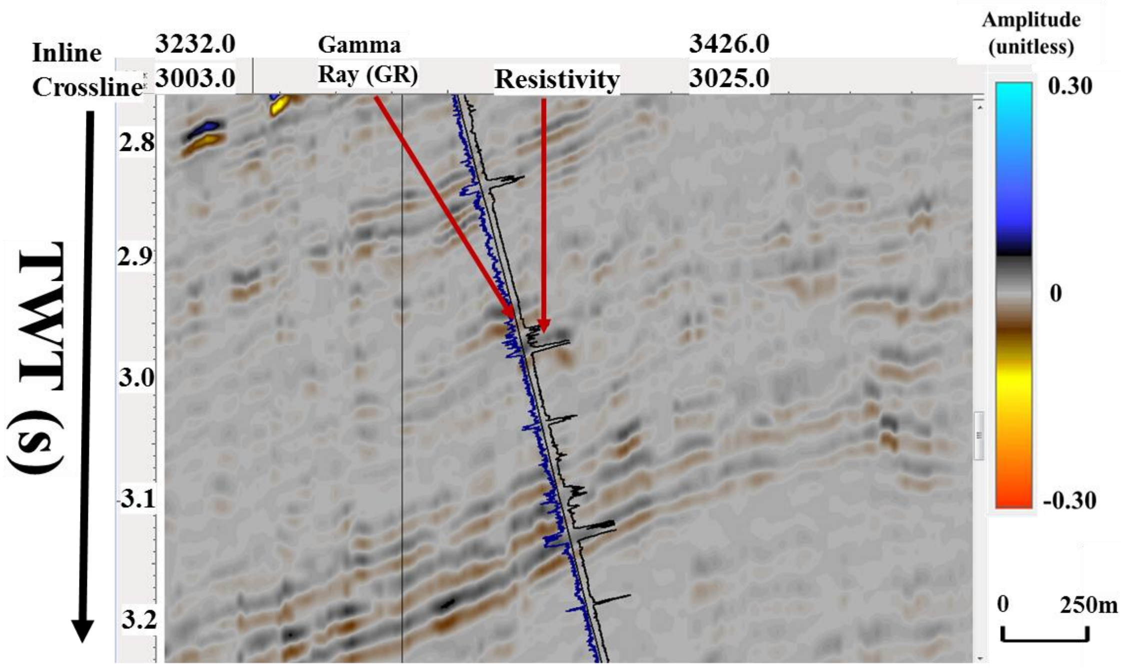

Figure 4.8c: +90° phase component of the original far stack. At the well, this phase attribute only highlights the deepest (and thickest) and shallowest pay intervals. However, for the very thin intervening layers it suggests more optimal nearby well locations that may encounter greater pay thickness. The amplitudes are relative and unitless.

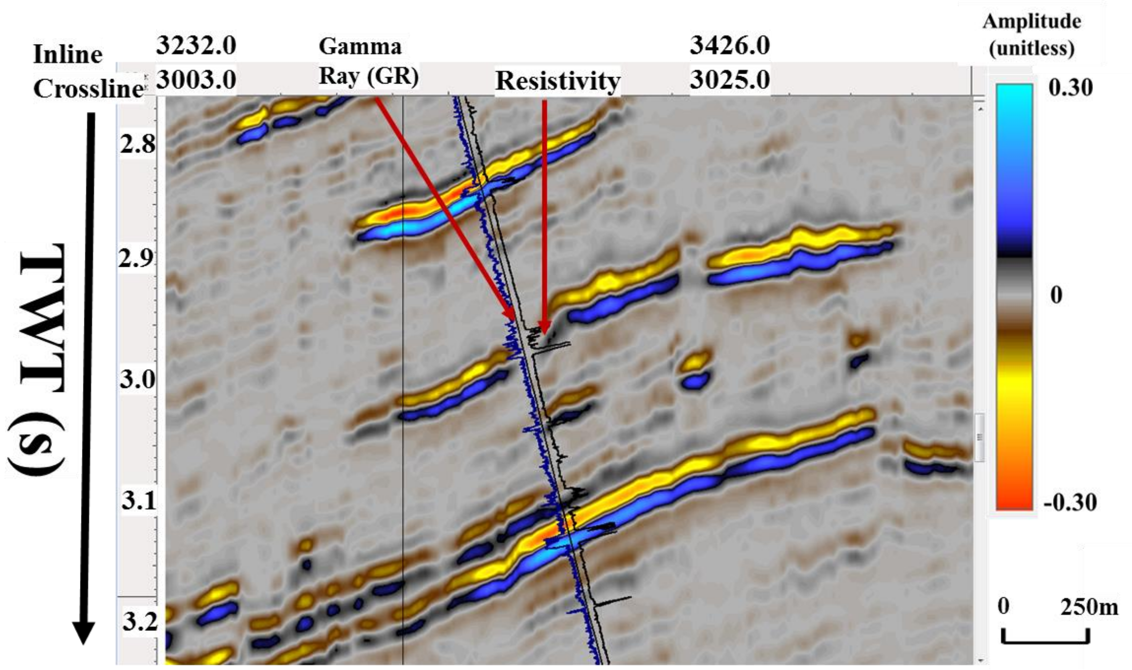

Figure 4.8d: -90° phase component of the original far stack suggesting only minor or highly localized thin hard layers. The amplitudes are relative and unitless.

4.4 Phase Decomposition of Bandwidth-extended data

Figures 4.9a-d and 4.10a-d are 180°, 0°, +90° and -90° phase components for the near and far bandwidth-extended data. Figures 4.10c and 4.10d show +90° and -90° phase components for the bandwidth-extended far stack data respectively. The shallowest and deepest reservoir units are now resolved, with a soft reflection at the top of the layer (Figure 4.10a) and a hard reflection at the base (Figure 4.10b).

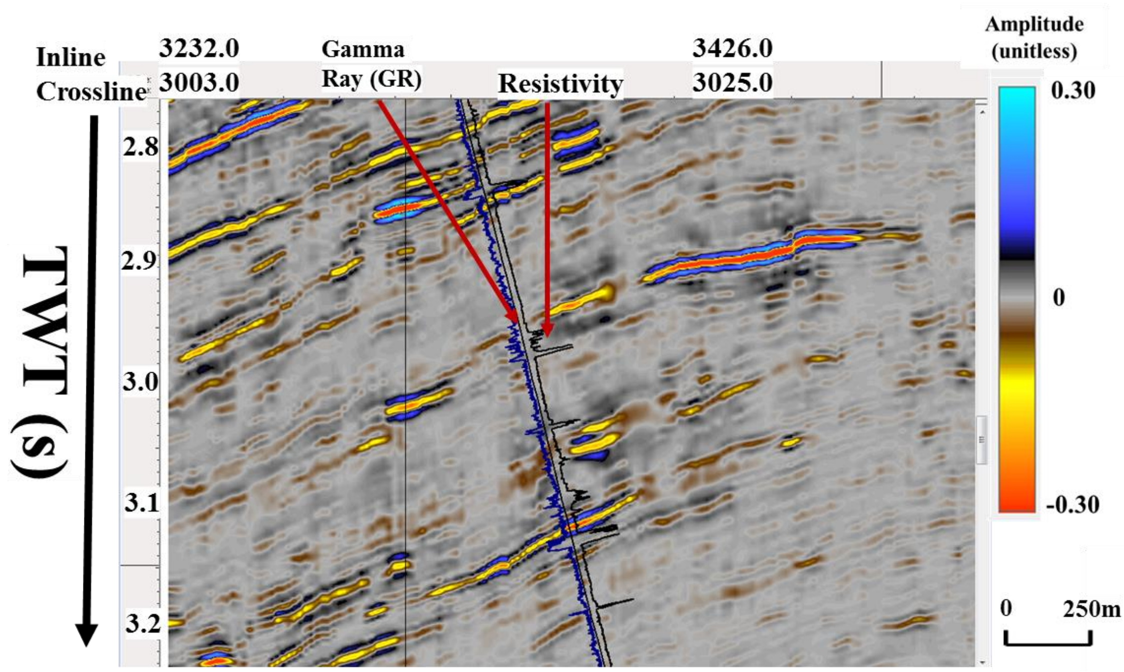

Figure 4.9a: 180° phase component of the bandwidth-extended near-stack. The amplitudes are relative and unitless.

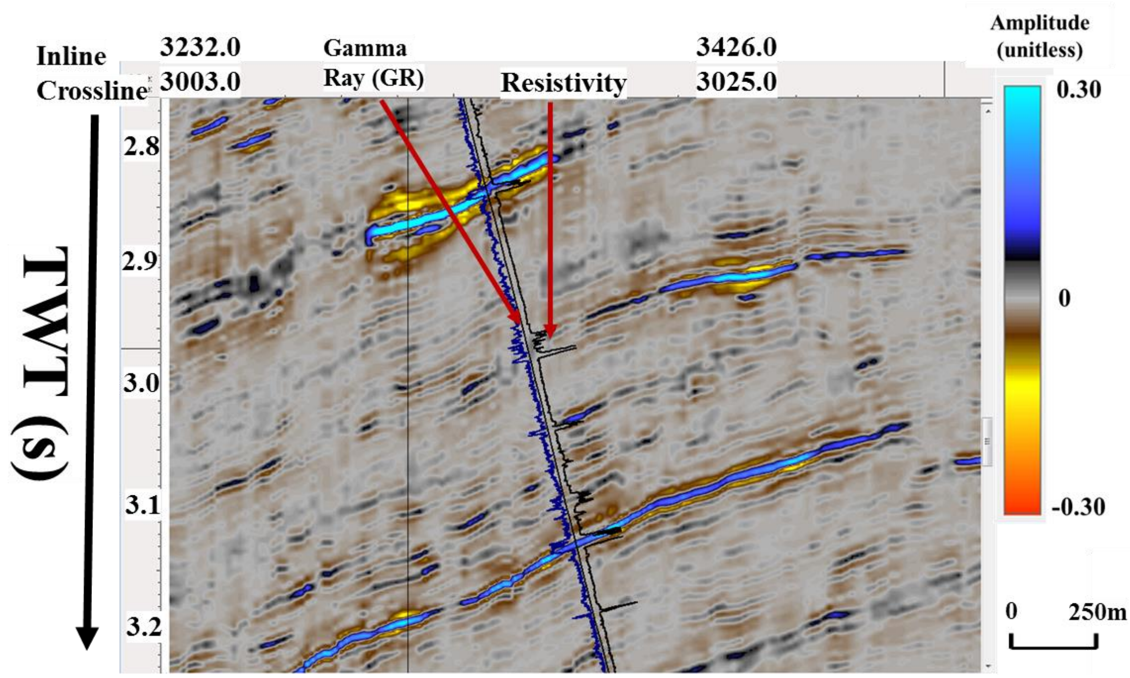

Figure 4.9b: 0° phase component of the bandwidth-extended near stack. The amplitudes are relative and unitless.

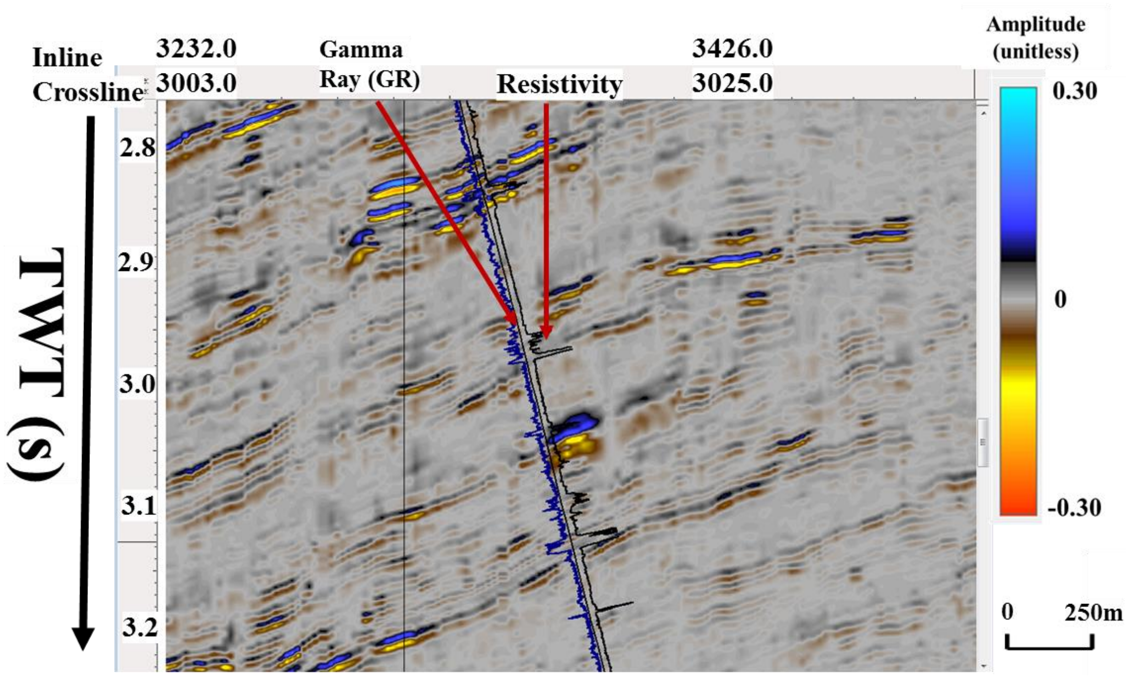

Figure 4.9c: +90° phase component of the bandwidth-extended near stack. The amplitudes are relative and unitless.

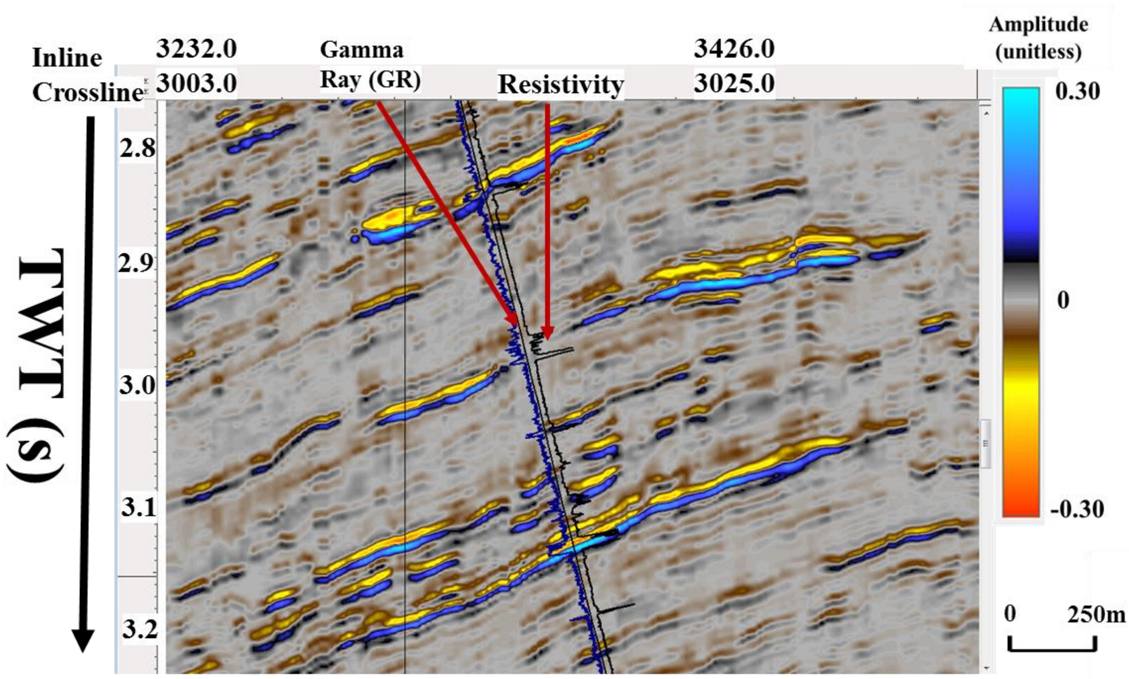

Figure 4.9d: -90° phase component of the bandwidth-extended near stack. The amplitudes are relative and unitless.

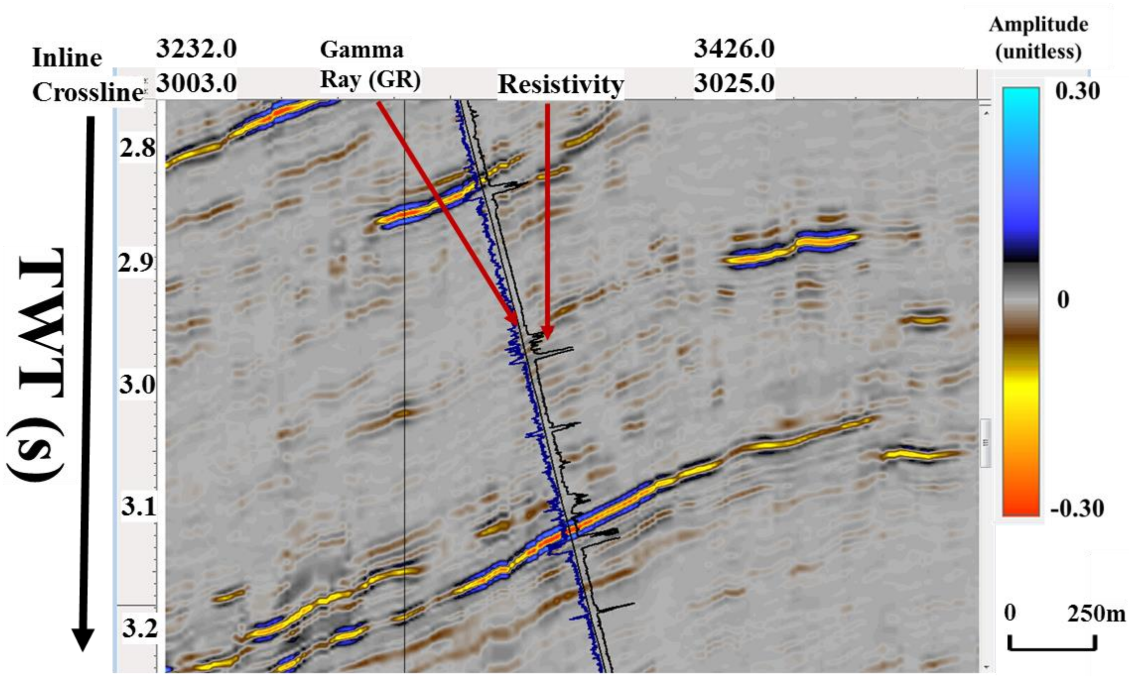

Figure 4.10a: 180° phase component of the bandwidth-extended far stack. The tops of the shallowest and deepest reservoirs exhibit significant step decrease in impedance at the well. The amplitudes are relative and unitless.

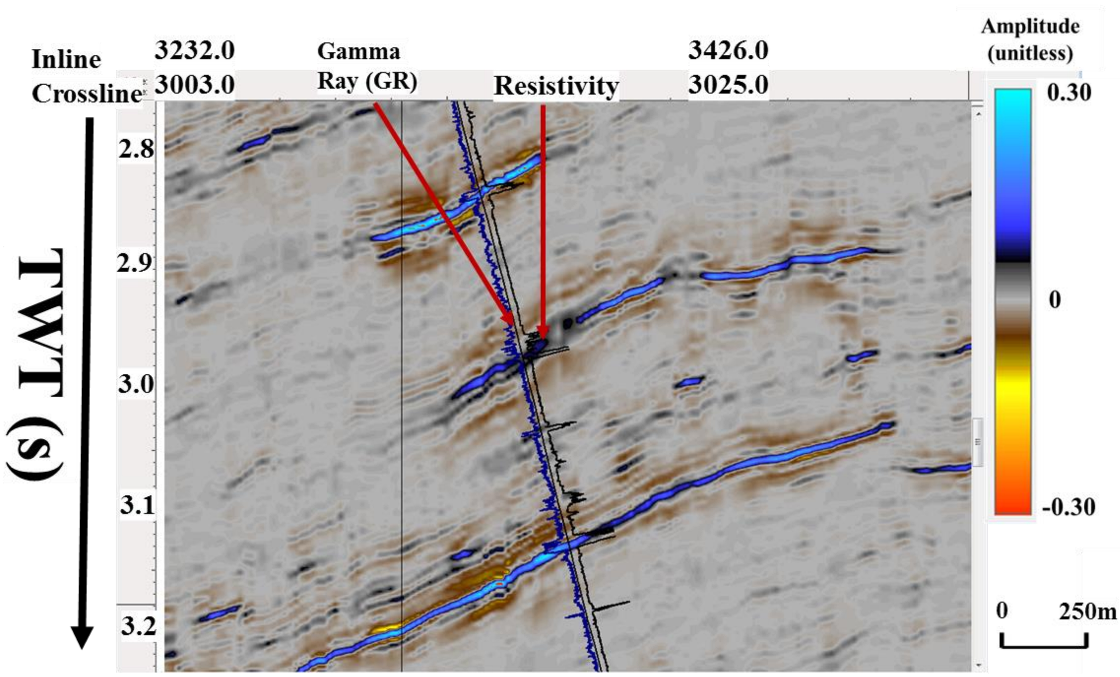

Figure 4.10b: 0° phase component of the bandwidth-extended far stack. The bases of the shallowest and deepest reservoirs are the most significant resolved step increases in impedance at the well. The amplitudes are relative and unitless.

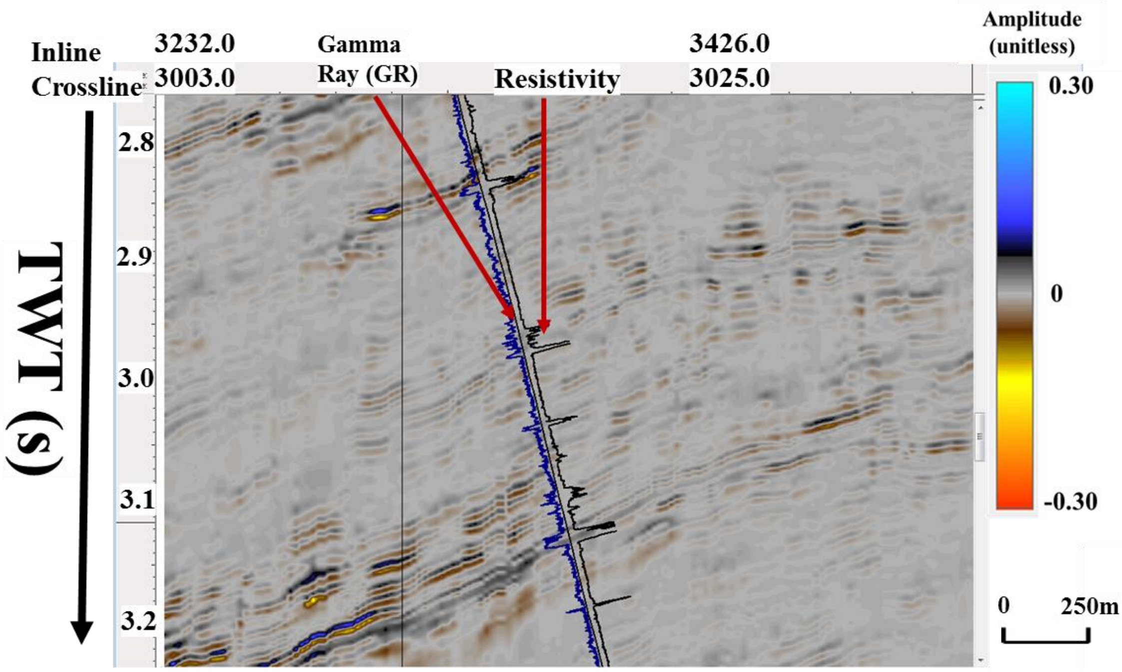

Figure 4.10c: +90° phase component of the bandwidth-extended far stack. The amplitudes are relative and unitless.

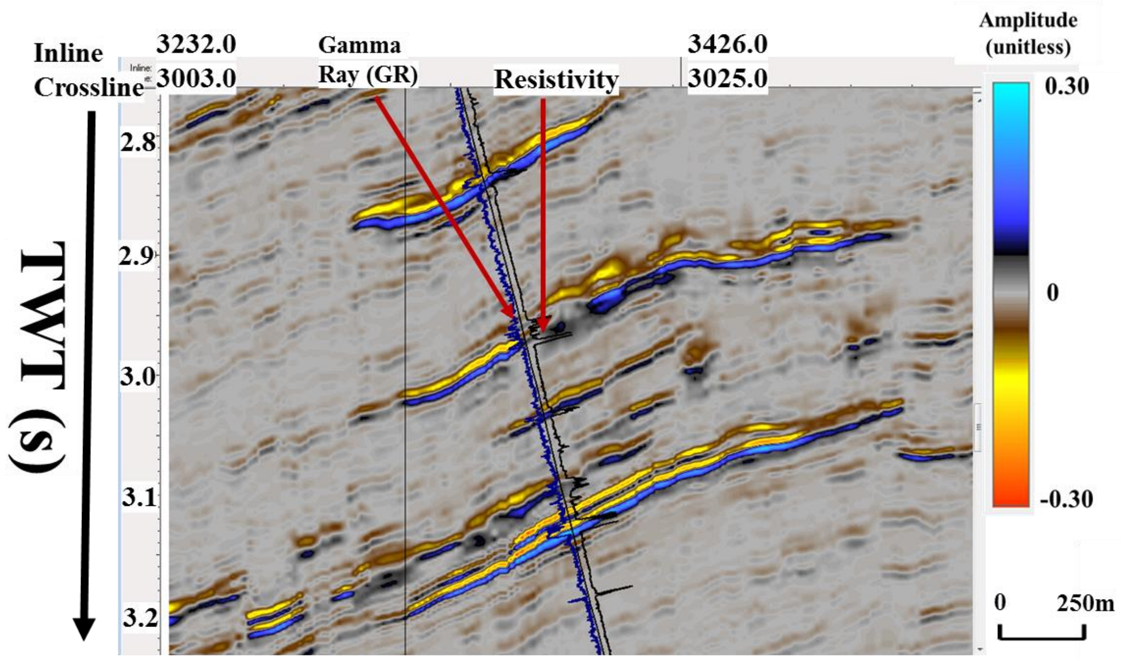

Figure 4.10d: -90° phase component of the bandwidth-extended far stack. The amplitudes are relative and unitless.

4.5 Hydrocarbon Detection

The apparently improved vertical resolution of the bandwidth-extended data has the advantage of allowing shorter window lengths to be used for attribute analysis in some cases.

For example, on the original seismic data a 30 ms window was required to span the event associated with a given pay interval, while the same event could be spanned by a 15 ms window on the bandwidth-extended data. The short window and better layer resolution after spectral broadening resulted in a crisper relative amplitude map with expanded areal extent of the reservoir (Figures 4.11a and 4.11b). The increased map areas are a result of partial mitigation of sub-tuning amplitude loss resulting from destructive interference from top and bottom layer reflections. By collapsing the wavelet breadth and reducing side lobes, the destructive tuning effects are reduced and greater apparent lateral extent of the reservoirs results.

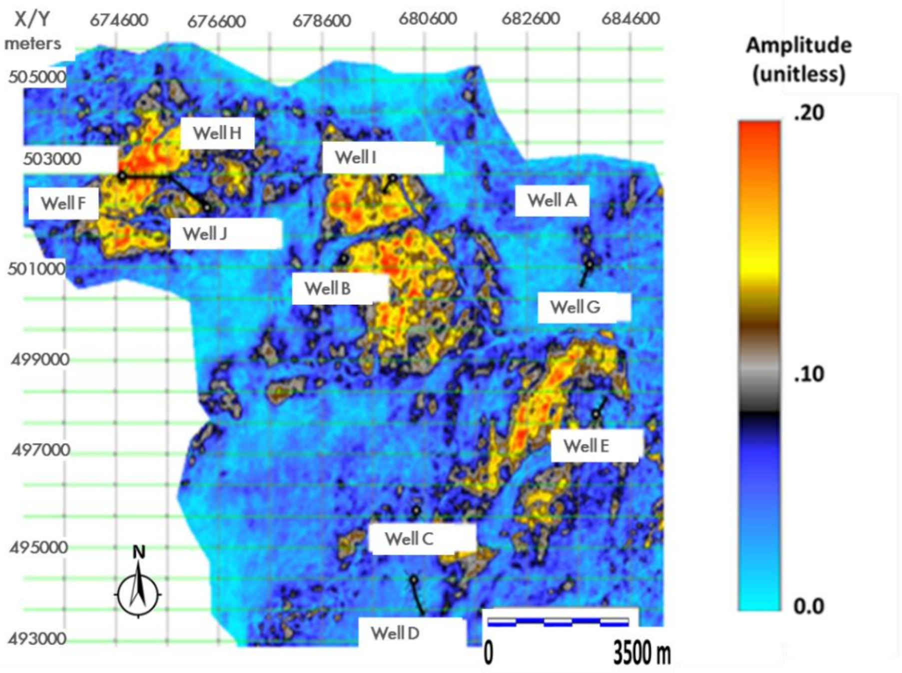

Figure 4.11a: RMS amplitude map on original stack for a 30 ms window centered on a single reservoir unit. Red is high relative amplitude and light blue is low relative amplitude. Black lines are well paths. Solid black circles are bottom hole well locations. The amplitudes are relative and unitless.

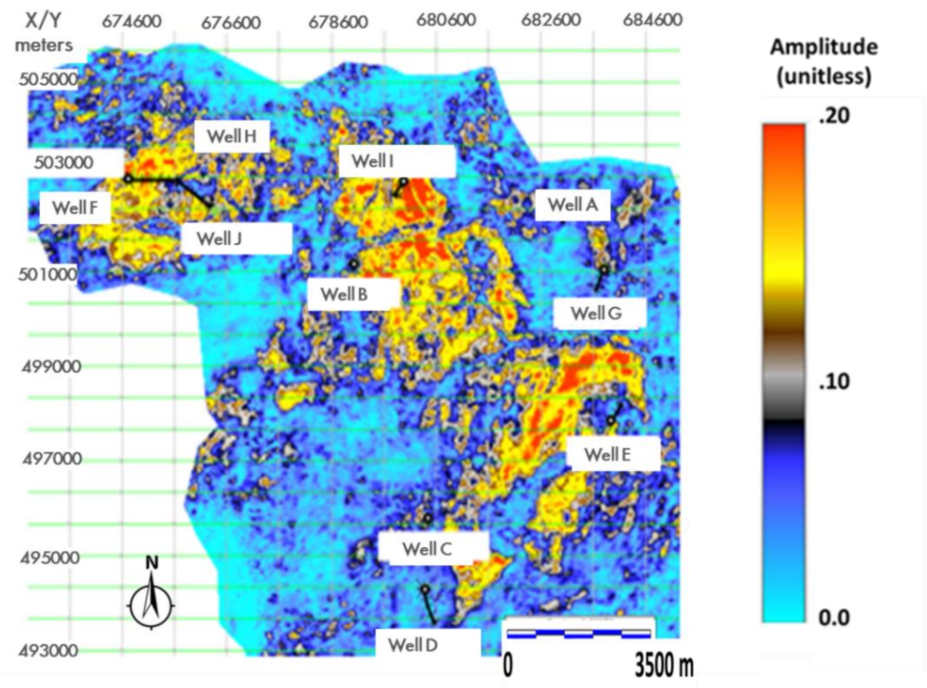

Figure 4.11b: RMS amplitude map on bandwidth-extended stack for a 15 ms window centered on a single reservoir unit. Red is high relative amplitude and light blue is low relative amplitude. Black lines are well paths. Solid black circles are bottom hole well locations. The amplitudes are relative and unitless.

Furthermore, amplitude extractions of original near and far stacks were made for a single reservoir (Figures 12a -b) as well as a bandwidth-extended near and far seismic data for comparison (Figures 12c -d) to further understand the hydrocarbon distribution at existing well locations and beyond well location. Similar extraction was done for additional reservoirs as shown in Appendix B.

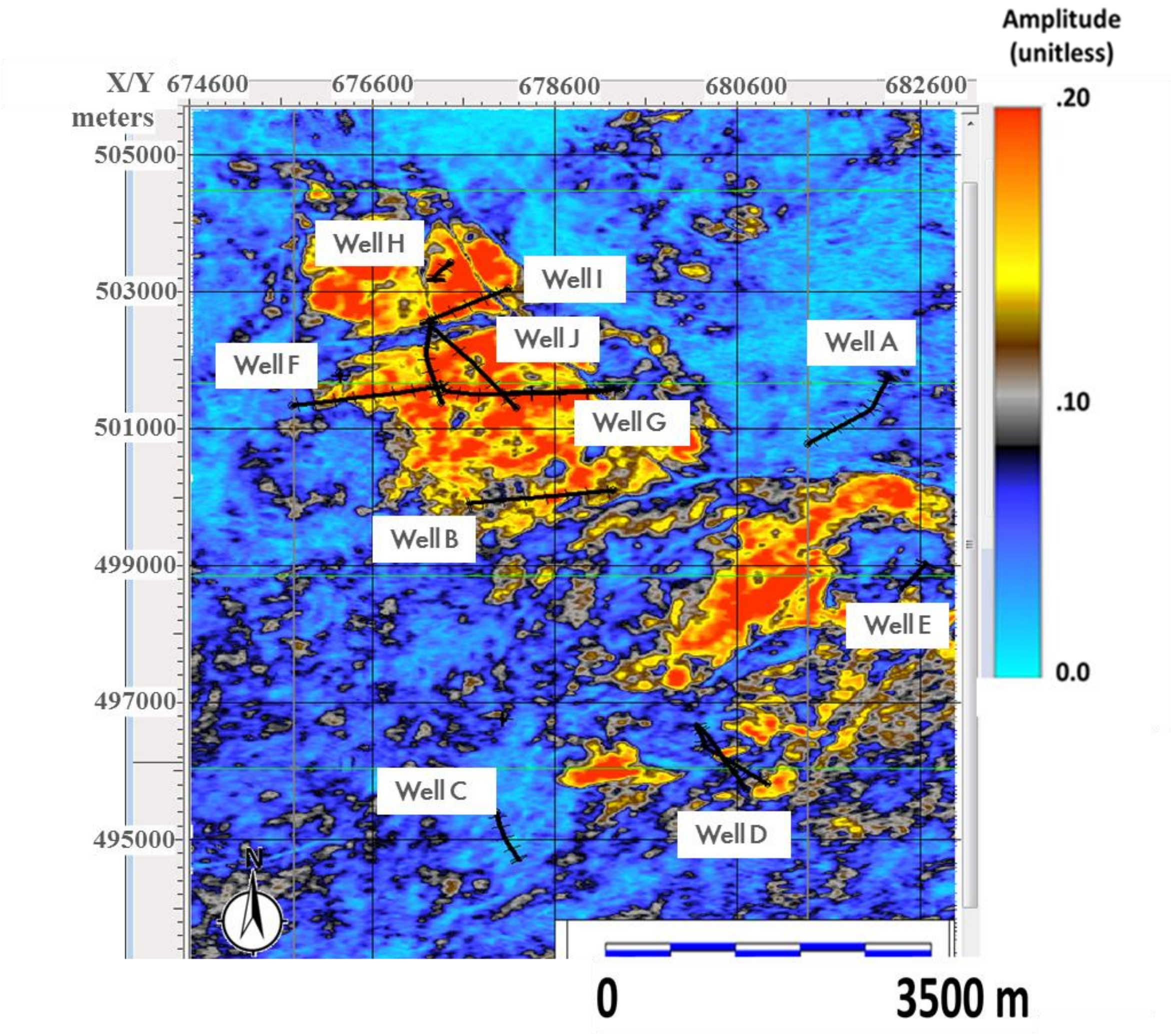

Figure 4.12a: RMS amplitude map of original near stack on a single reservoir unit. Red is high relative amplitude and light blue is low relative amplitude. Black lines are well paths. Solid black circles are bottom hole well locations. The amplitudes are relative and unitless.

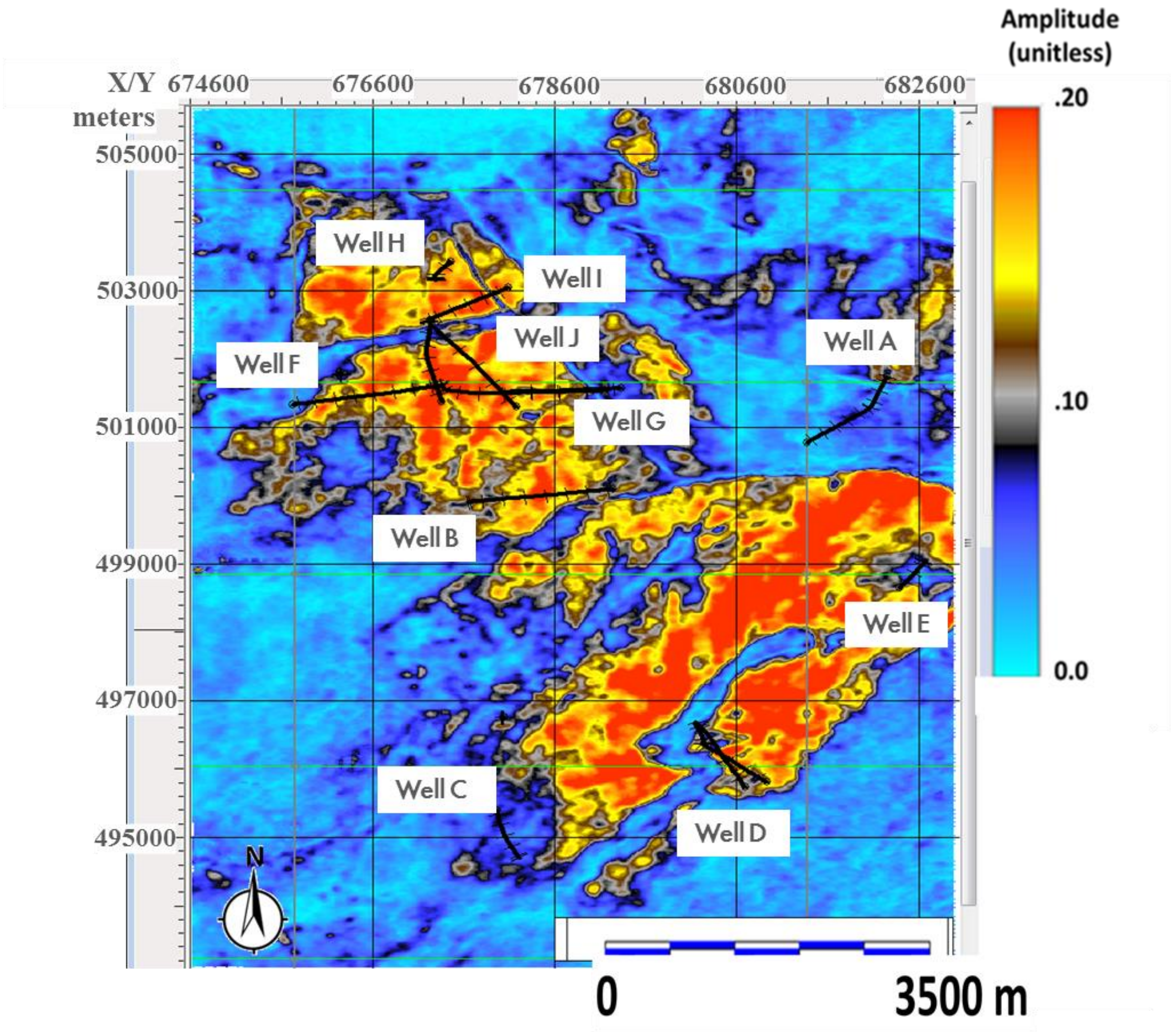

Figure 4.12b: RMS amplitude map of original far stack on a single reservoir unit. Red is high relative amplitude and light blue is low relative amplitude. Black lines are well paths. Solid black circles are bottom hole well locations. The amplitudes are relative and unitless.

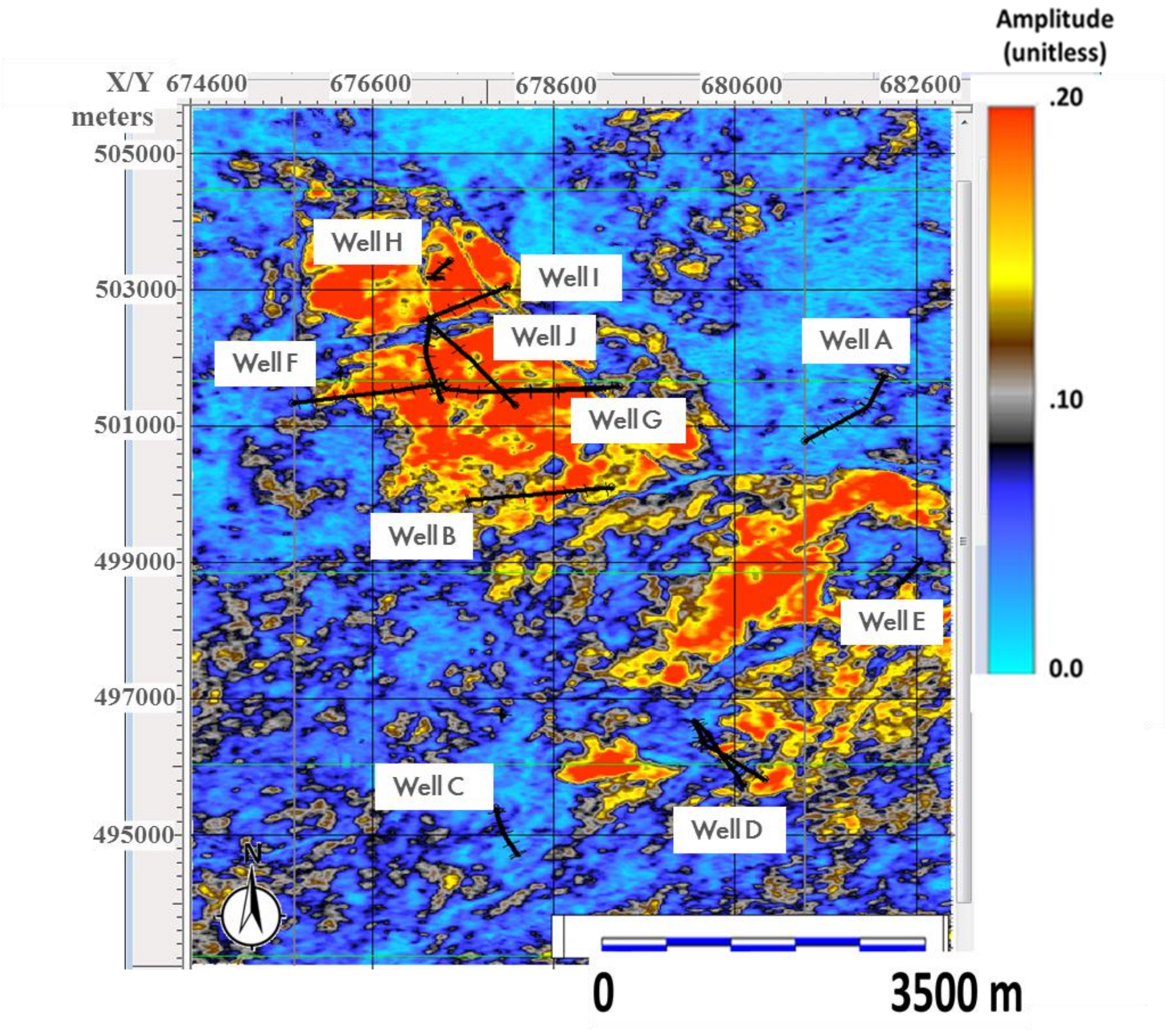

Figure 4.12c: RMS amplitude map of bandwidth-extended near stack on a single reservoir unit. Red is high relative amplitude and light blue is low relative amplitude. Black lines are well paths. Solid black circles are bottom hole well locations. The amplitudes are relative and unitless.

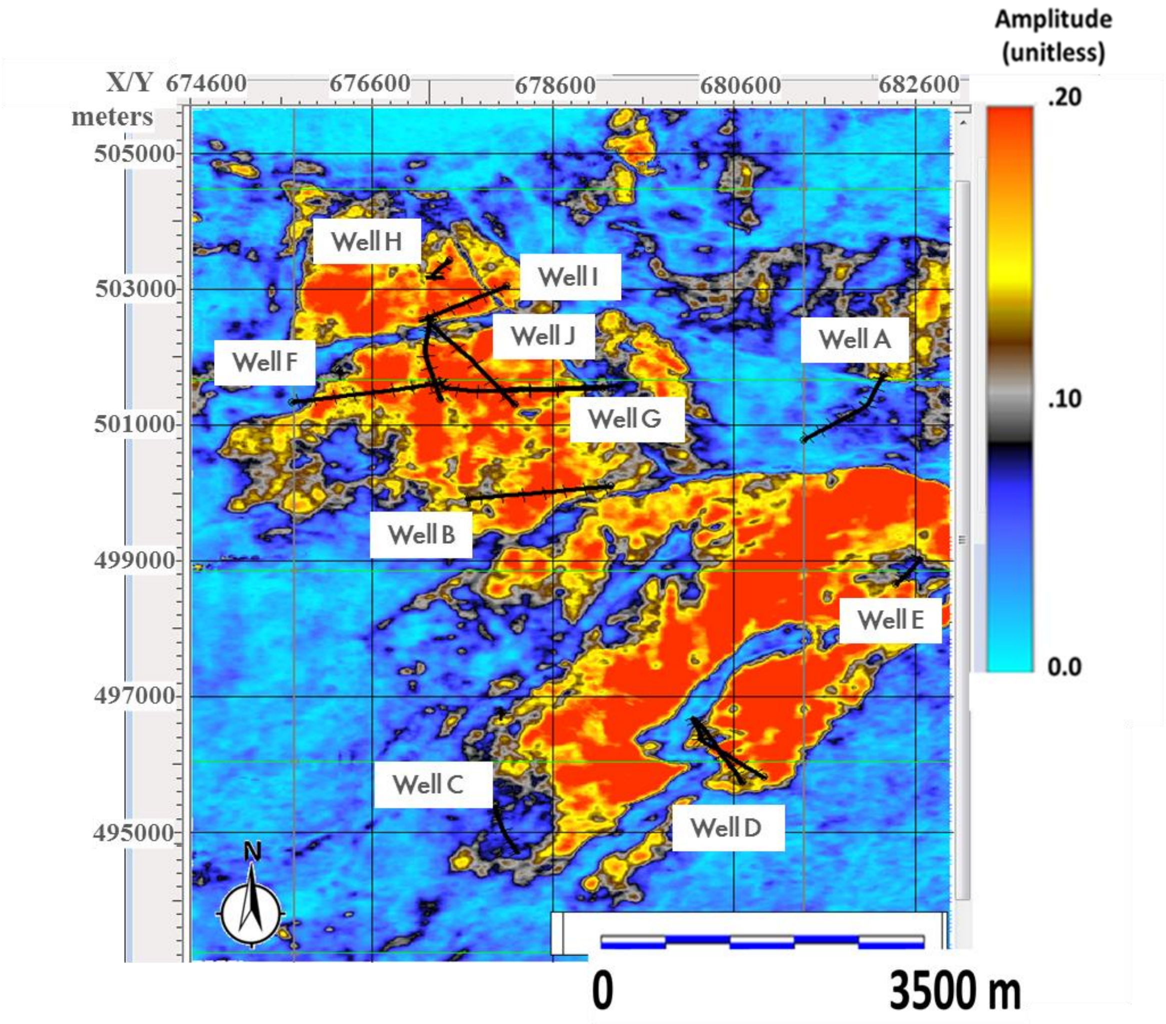

Figure 4.12d: RMS amplitude map of bandwidth-extended far stack on a single reservoir unit. Red is high relative amplitude and light blue is low relative amplitude. Black lines are well paths. Solid black circles are bottom hole well locations. The amplitudes are relative and unitless.

Figures 4.13 (a -d) and 4.14 (a -d) illustrate the different phase components of the original near and extended banded near stacked data, while the different phase components of the original far and extended banded far stacked data are as displayed in Figures 4. 15 (a -d) and 4.16 (a d). The significant pay at existing well locations have excellent correlation with amplitudes of the -90° phase components of the original far-offset seismic data (Figure 4.14d) while for very thin layers, phase decomposition, though weak at well locations, shows possible thicker reservoir slightly updip or down dip of well locations (Figure 4.16d).

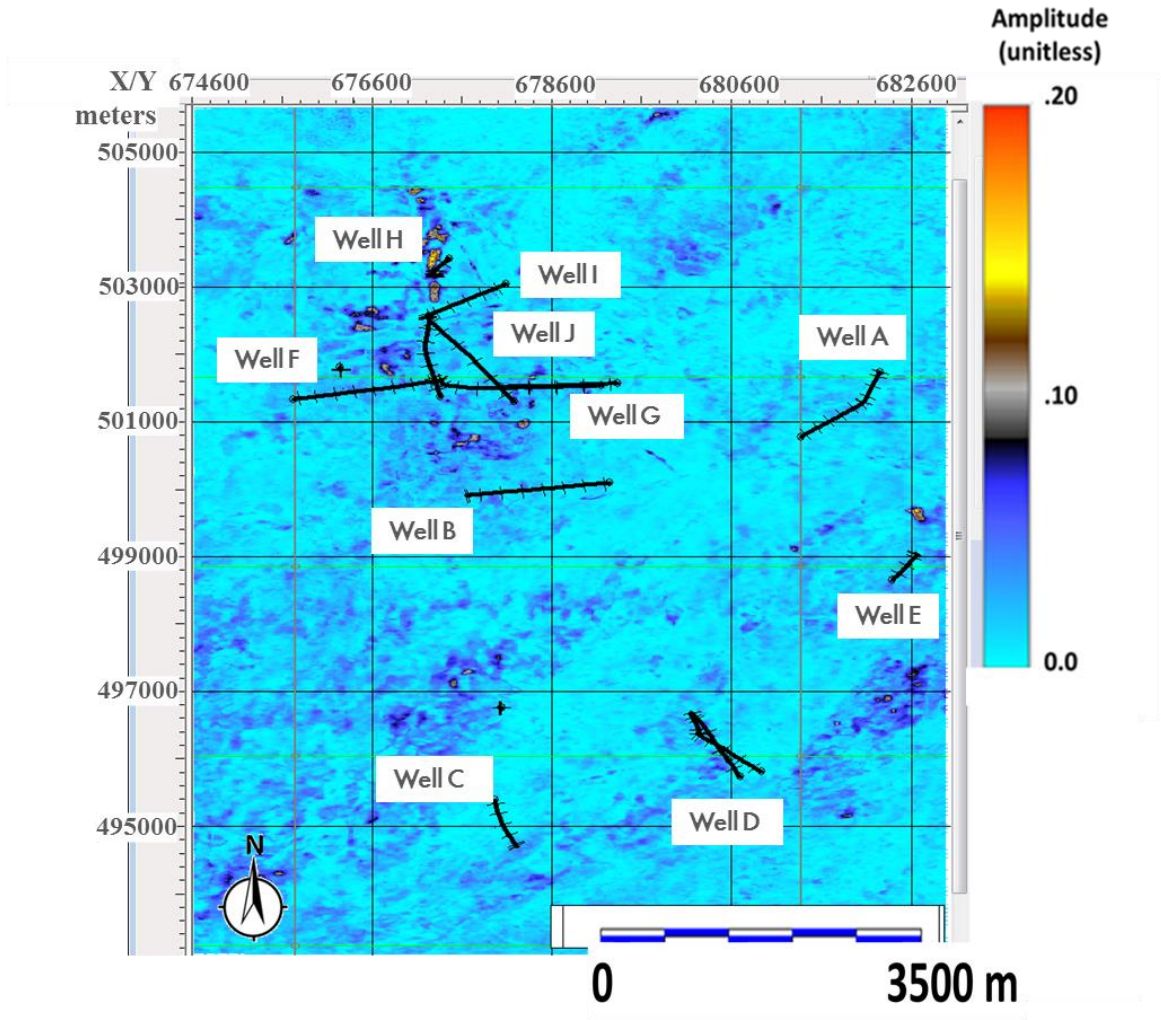

Figure 4.13a: RMS amplitude map on 0°phase component of the original seismic near stack. Red is high relative amplitude and light blue is low relative amplitude. Black lines are well paths. Solid black circles are bottom hole well locations. The amplitudes are relative and unitless.

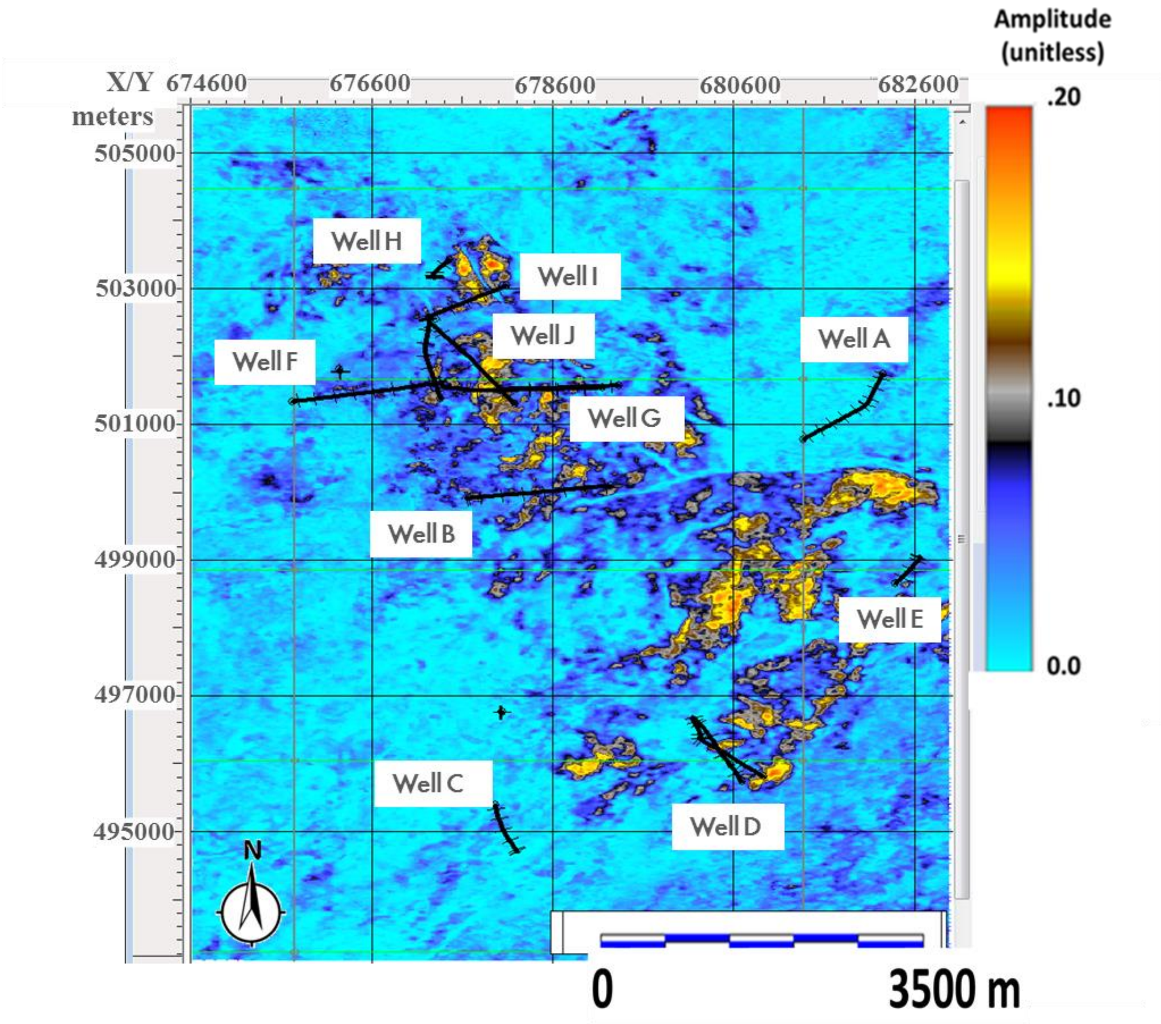

Figure 4.13b: RMS amplitude map on 180° phase component of the original seismic near stack data. Red is high relative amplitude and light blue is low relative amplitude. Black lines are well paths. Solid black circles are bottom hole well locations. The amplitudes are relative and unitless.

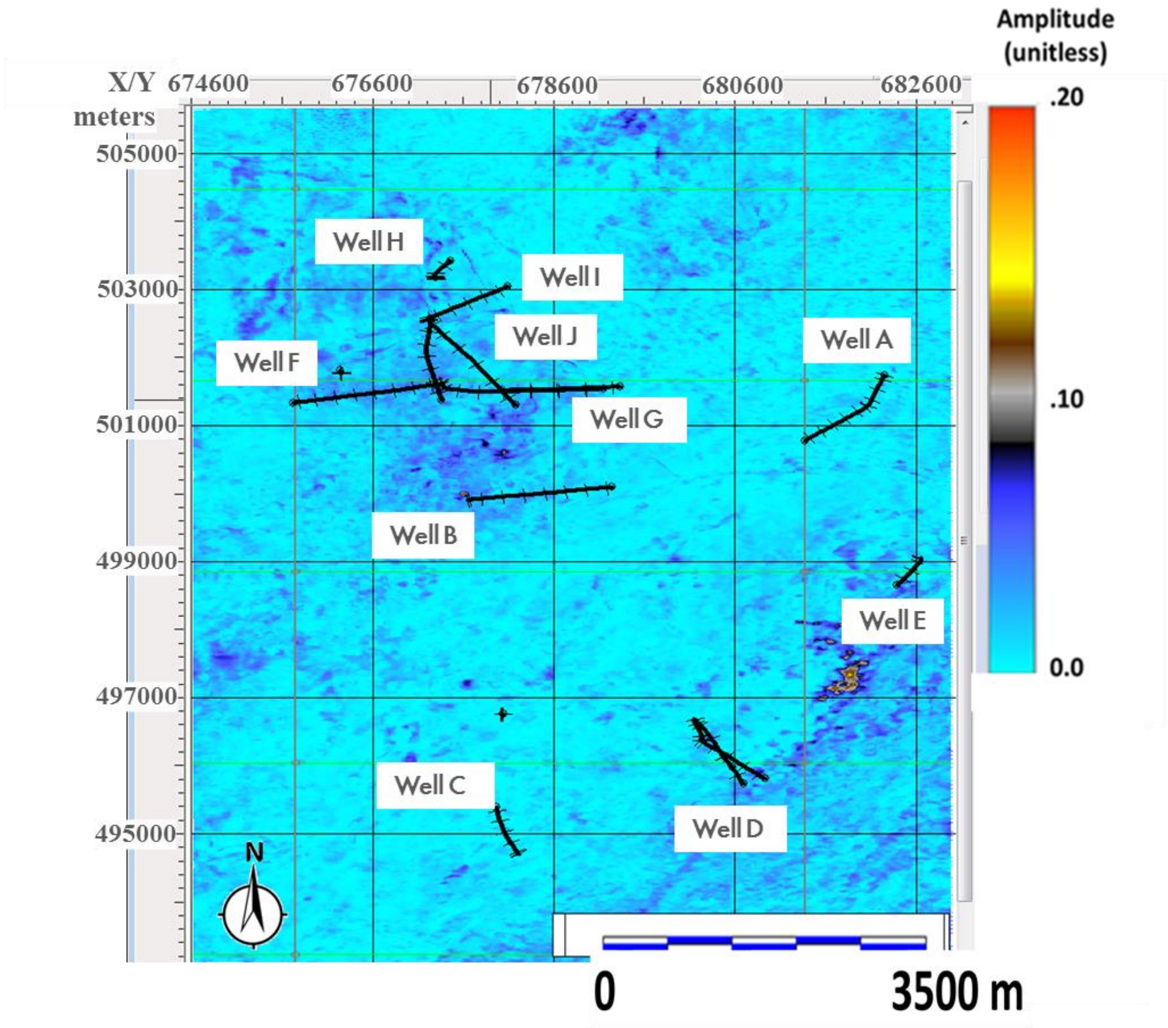

Figure 4.13c: RMS amplitude map on +90° phase component of the original seismic near stack. Red is high relative amplitude and light blue is low relative amplitude. Black lines are well paths. Solid black circles are bottom hole well locations. The amplitudes are relative and unitless.

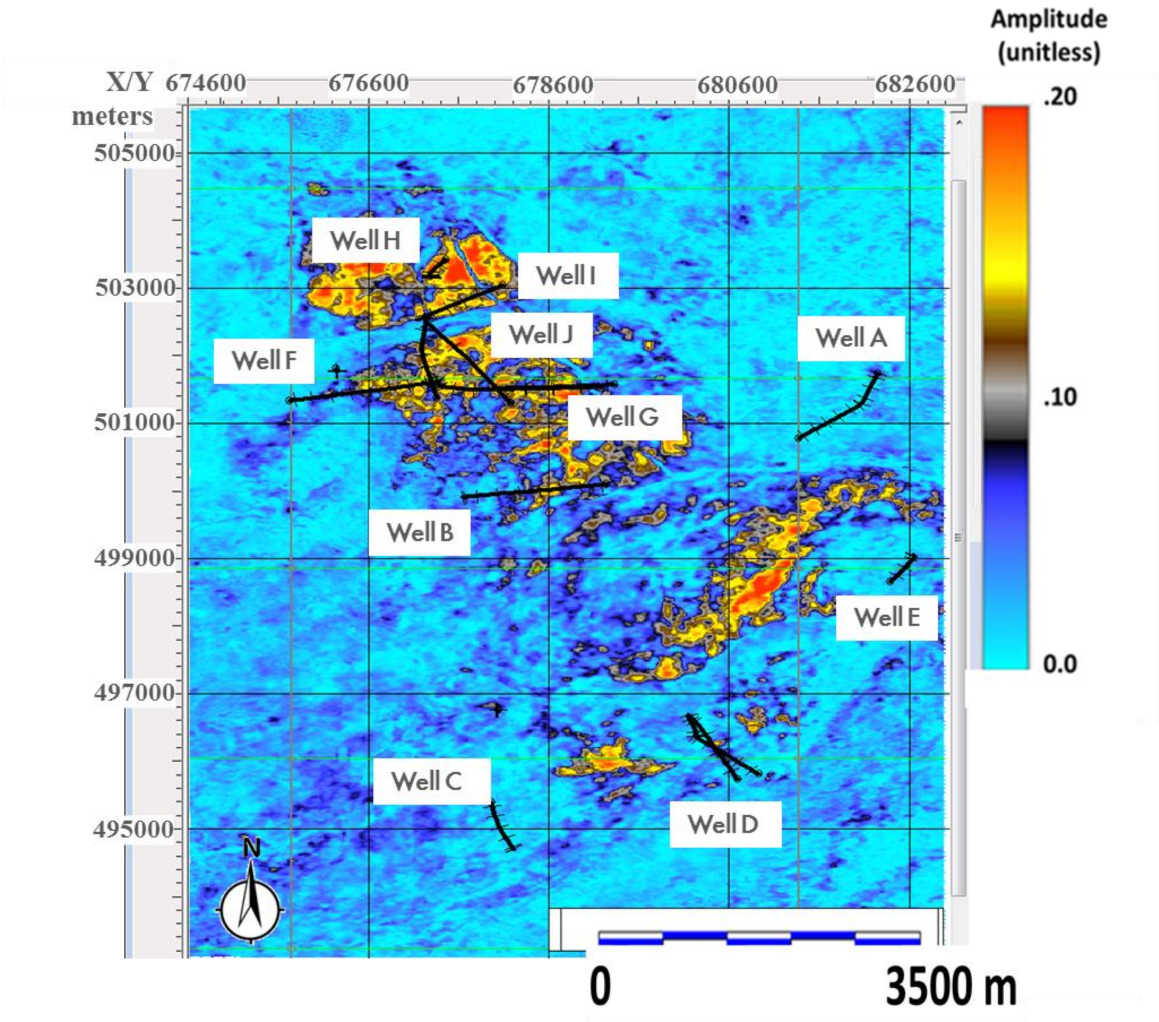

Figure 4.13d: RMS amplitude map on -90° phase component of the original seismic near stack. Red is high relative amplitude and light blue is low relative amplitude. Black lines are well paths. Solid black circles are bottom hole well locations. The amplitudes are relative and unitless.

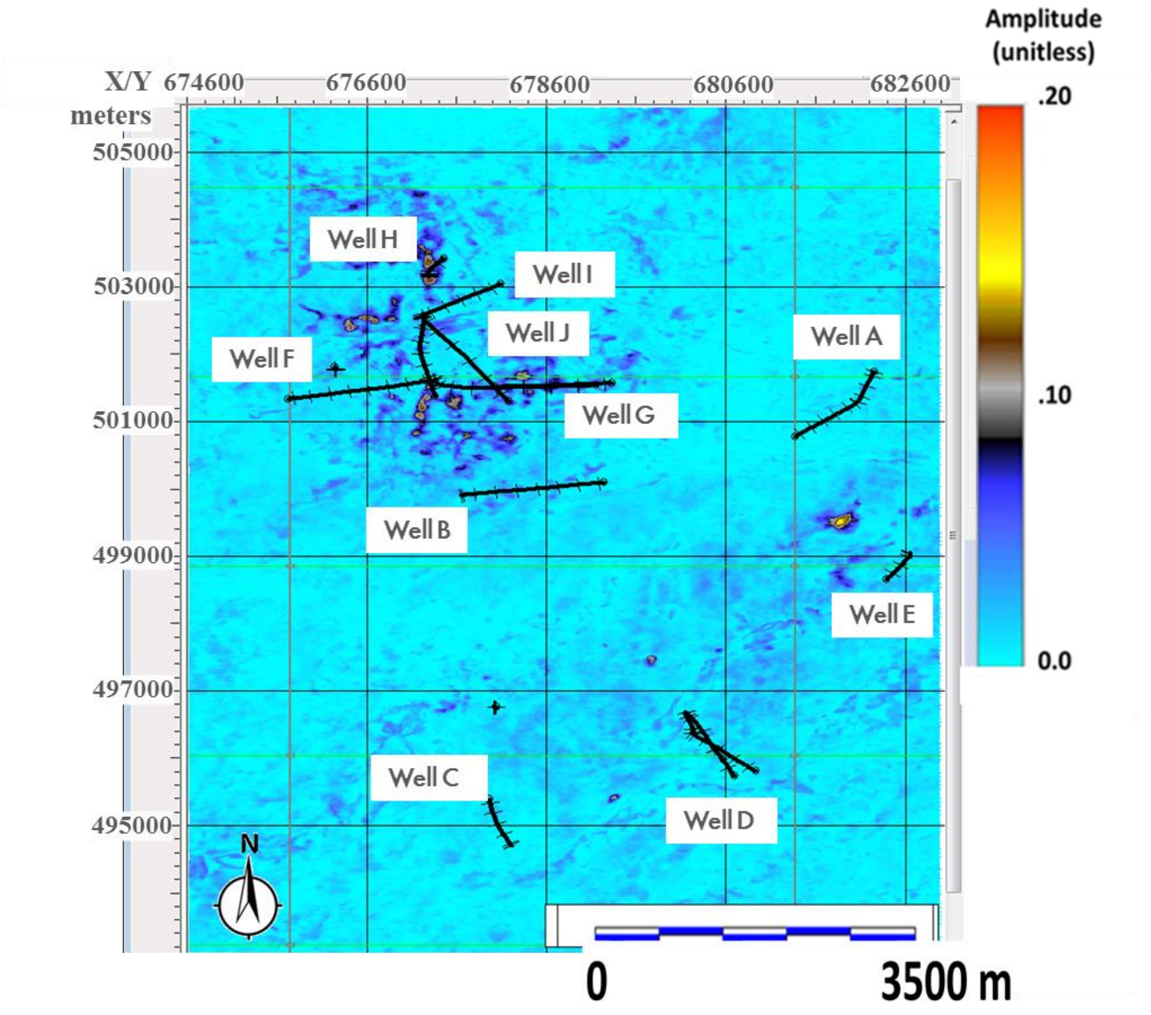

Figure 4.14a: RMS amplitude map on 0° phase component of the original seismic far stack. Red is high relative amplitude and light blue is low relative amplitude. Black lines are well paths. Solid black circles are bottom hole well locations. The amplitudes are relative and unitless.

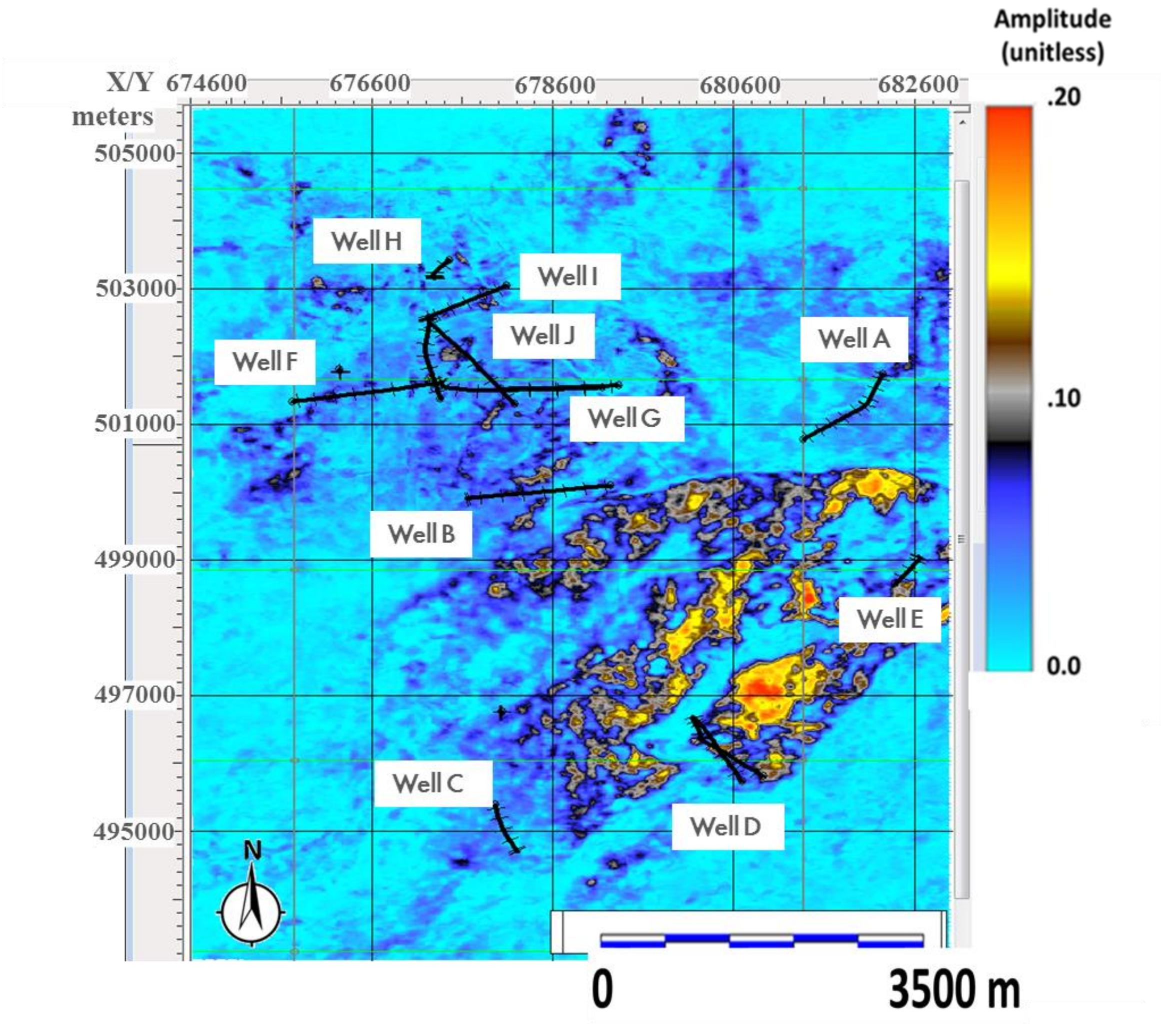

Figure 4.14b: RMS amplitude map on 180° phase component of the original seismic far stack. Red is high relative amplitude and light blue is low relative amplitude. Black lines are well paths. Solid black circles are bottom hole well locations. The amplitudes are relative and unitless.

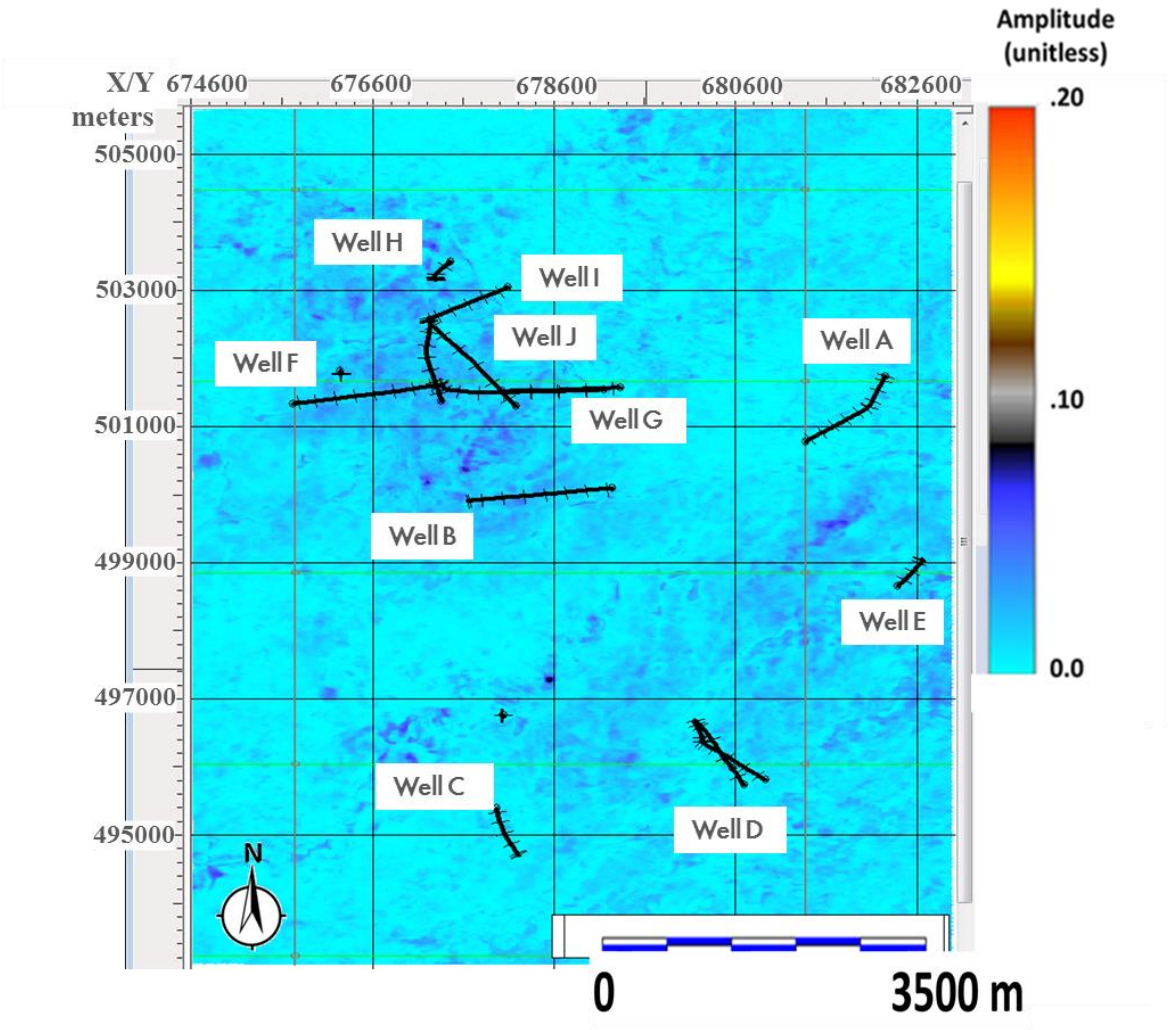

Figure 4.14c: RMS amplitude map on +90° phase component of the original seismic far stack. Red is high relative amplitude and light blue is low relative amplitude. Black lines are well paths. Solid black circles are bottom hole well locations. The amplitudes are relative and unitless.

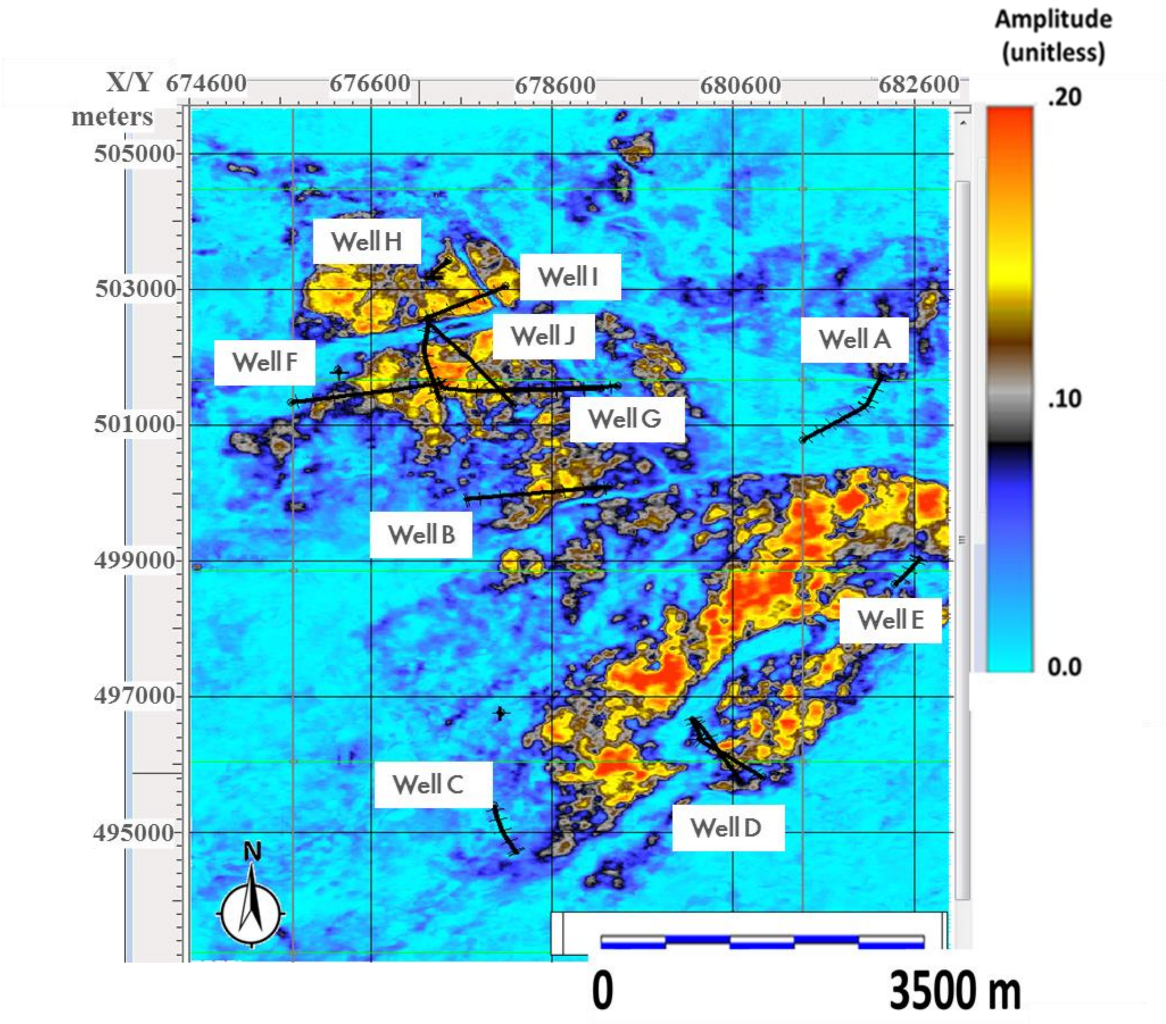

Figure 4.14d: RMS amplitude map on -90° phase component of the original seismic far stack. Red is high relative amplitude and light blue is low relative amplitude. Black lines are well paths. Solid black circles are bottom hole well locations. The amplitudes are relative and unitless.

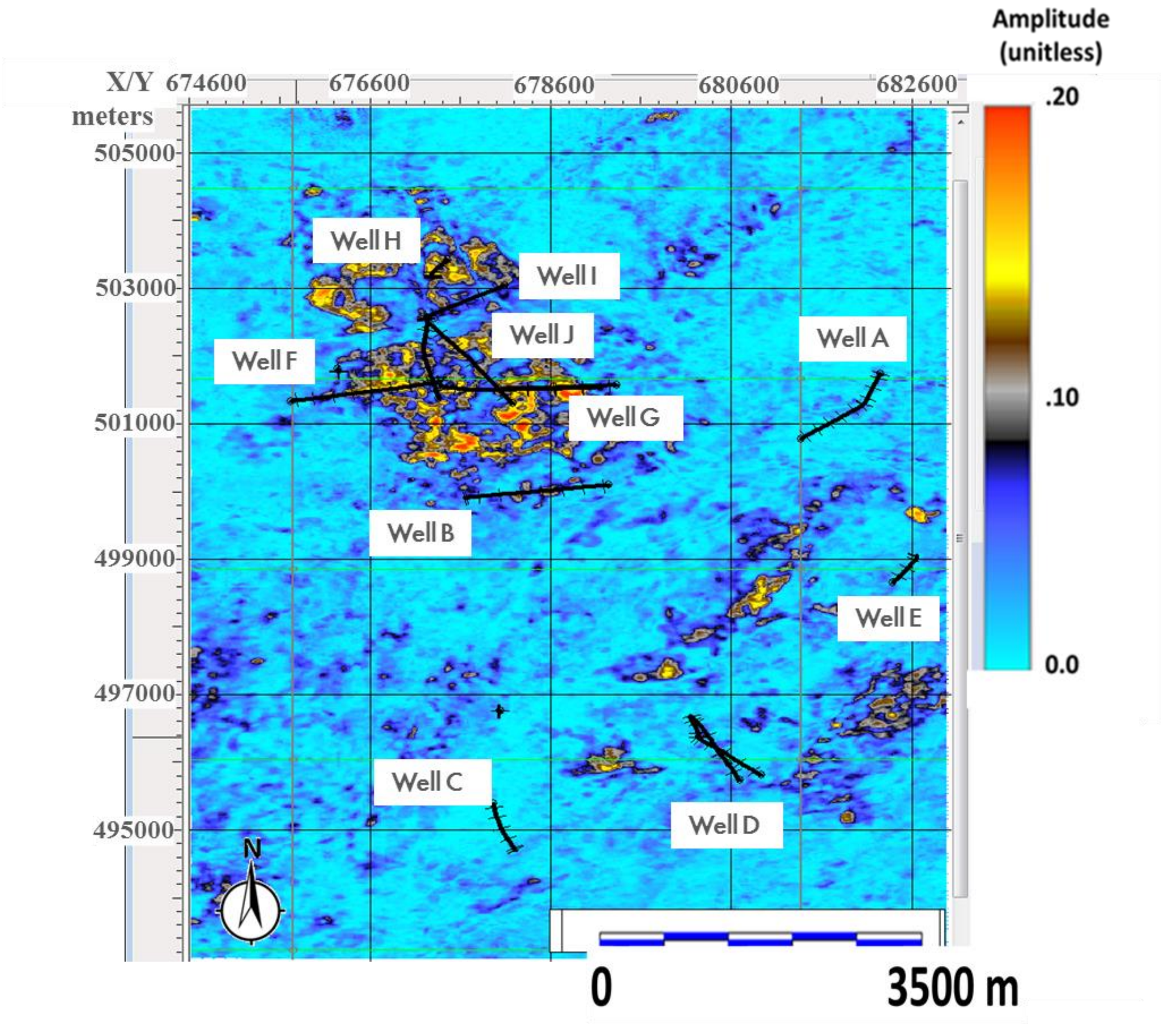

Figure 4.15a: RMS amplitude map on 0° phase component of the bandwidth-extended near stack. Red is high relative amplitude and light blue is low relative amplitude. Black lines are well paths. Solid black circles are bottom hole well locations. The amplitudes are relative and unitless.

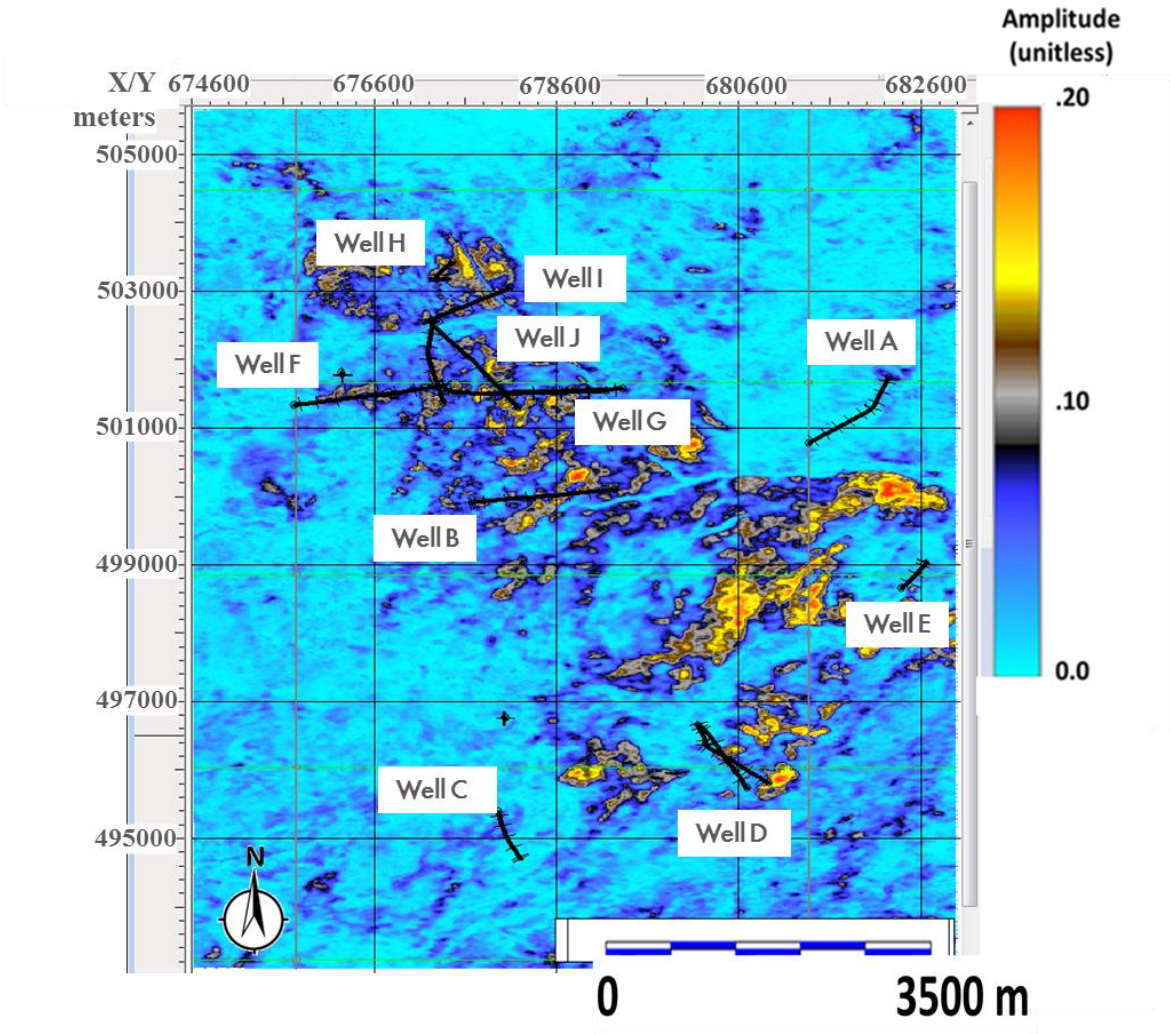

Figure 4.15b: RMS amplitude map on 180° phase component of the bandwidth-extended near stack. Red is high relative amplitude and light blue is low relative amplitude. Black lines are well paths. Solid black circles are bottom hole well locations. The amplitudes are relative and unitless.

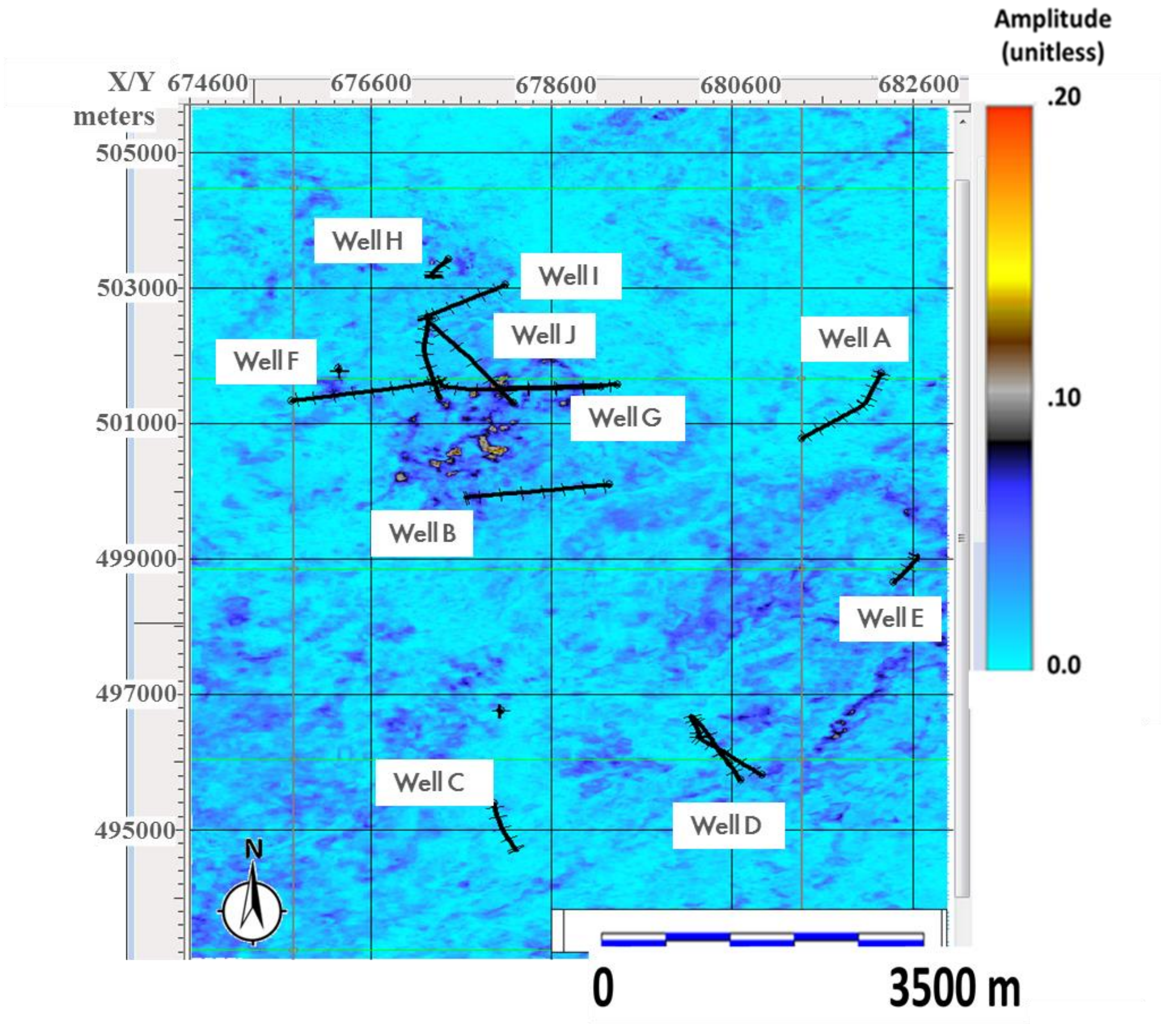

Figure 4.15c: RMS amplitude map on +90° phase component of the bandwidth-extended near stack. Red is high relative amplitude and light blue is low relative amplitude. Black lines are well paths. Solid black circles are bottom hole well locations. The amplitudes are relative and unitless.

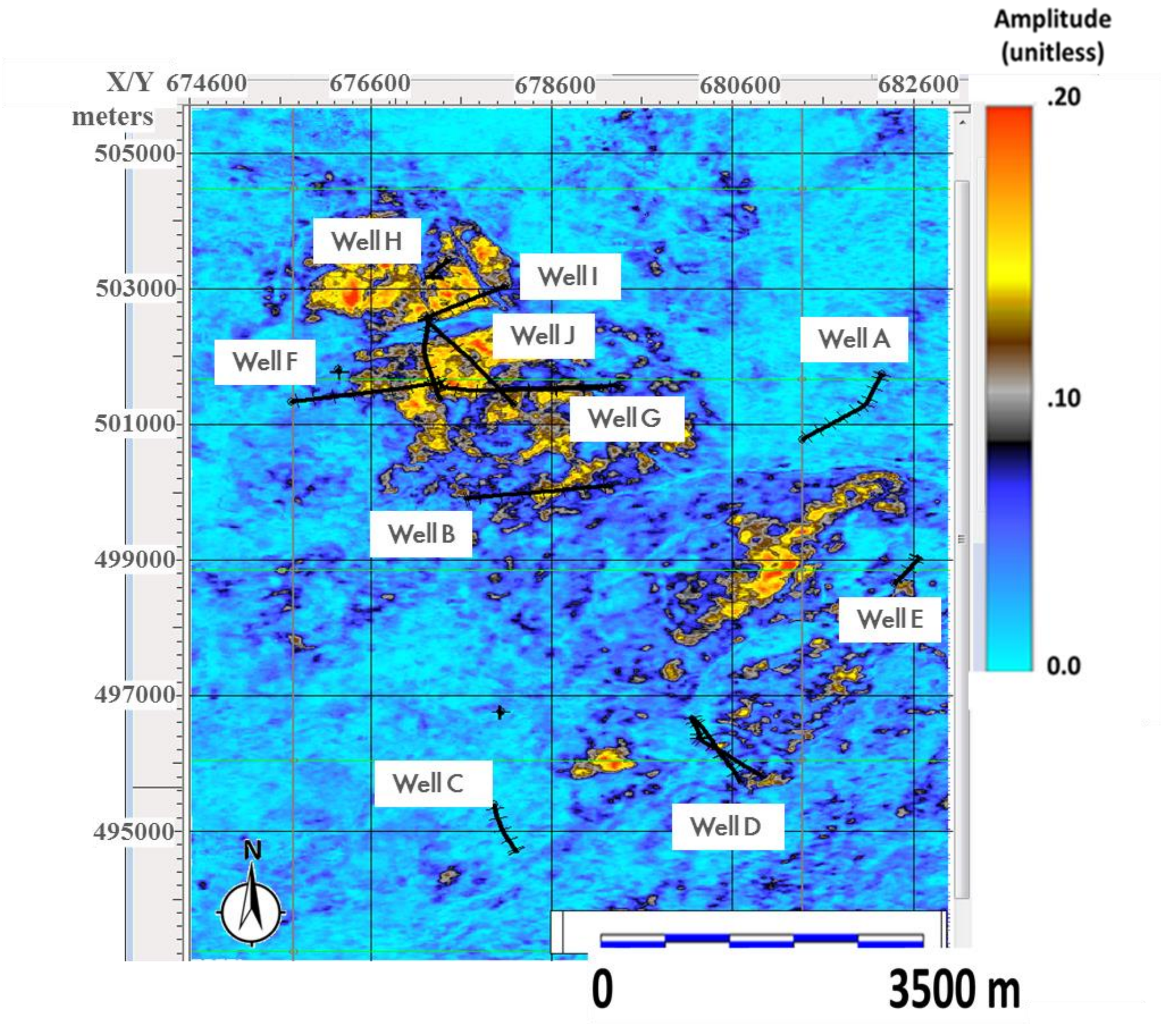

Figure 4.15d: RMS amplitude map on -90° phase component of the bandwidth-extended near stack. Red is high relative amplitude and light blue is low relative amplitude. Black lines are well paths. Solid black circles are bottom hole well locations. The amplitudes are relative and unitless.

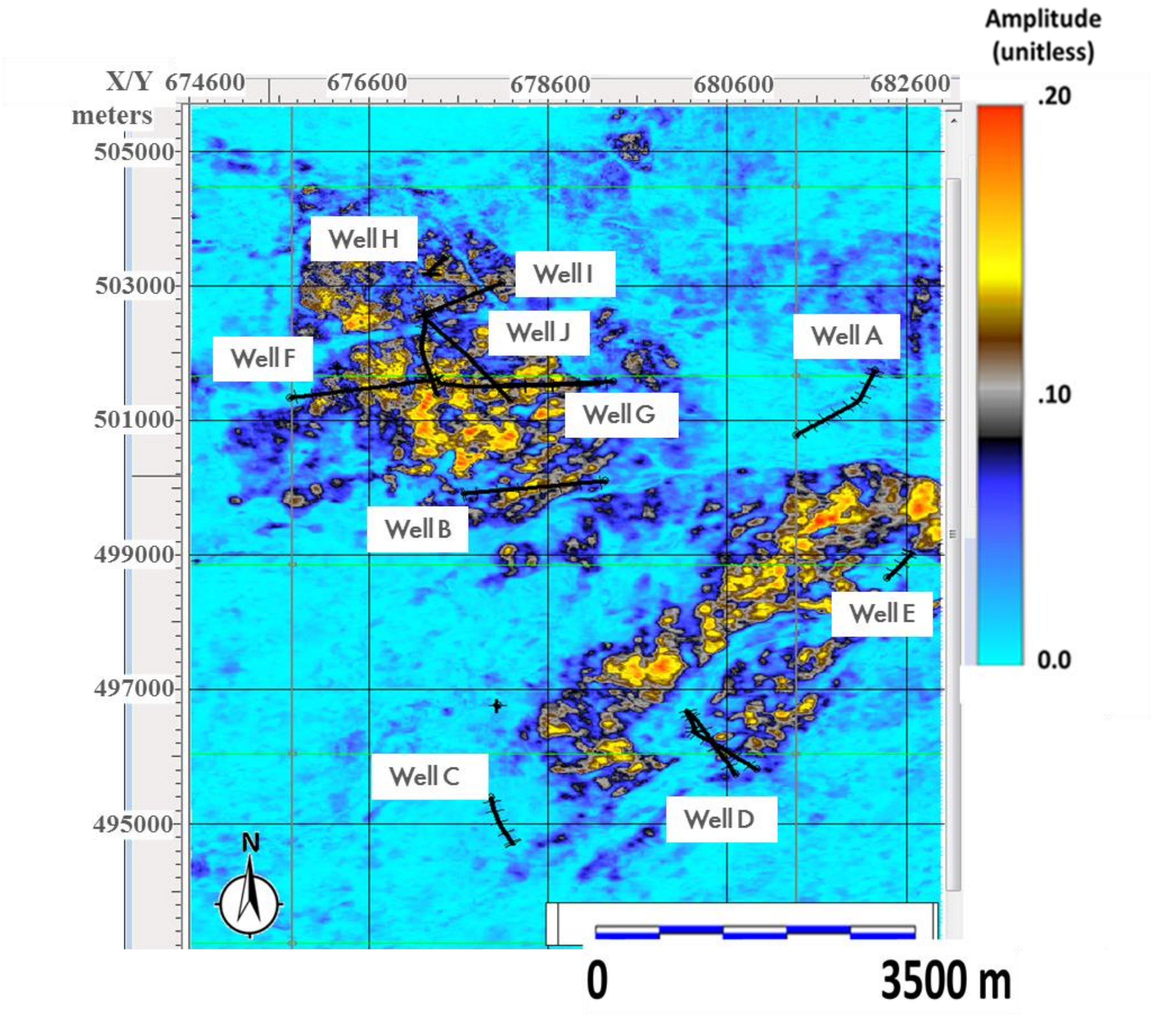

Figure 4.16a: RMS amplitude map on 0° phase component of the bandwidth-extended far stack. Red is high relative amplitude and light blue is low relative amplitude. Black lines are well paths. Solid black circles are bottom hole well locations. The amplitudes are relative and unitless.

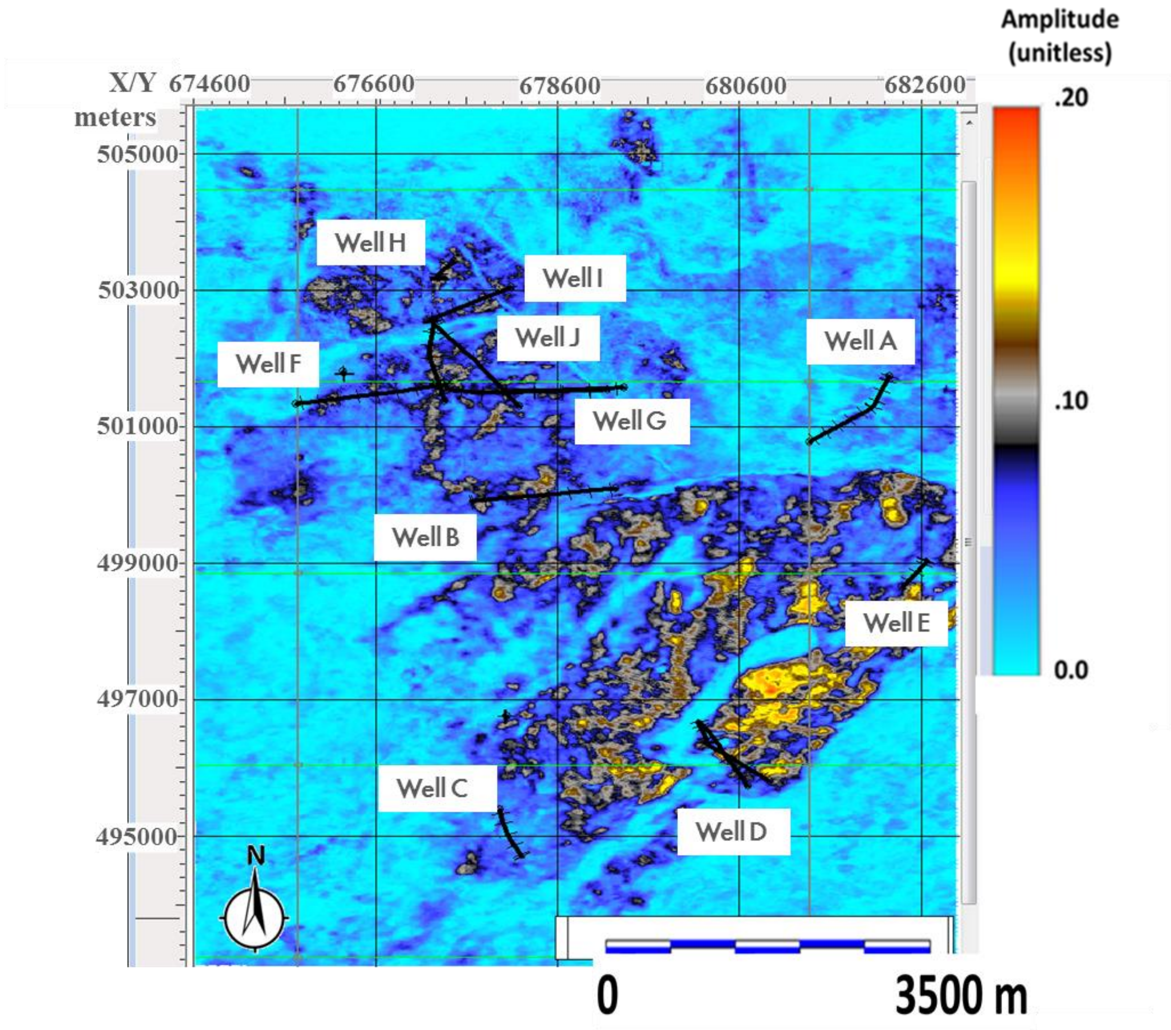

Figure 4.16b: RMS amplitude map on 180° phase component of the bandwidth-extended far stack. Red is high relative amplitude and light blue is low relative amplitude. Black lines are well paths. Solid black circles are bottom hole well locations. The amplitudes are relative and unitless.

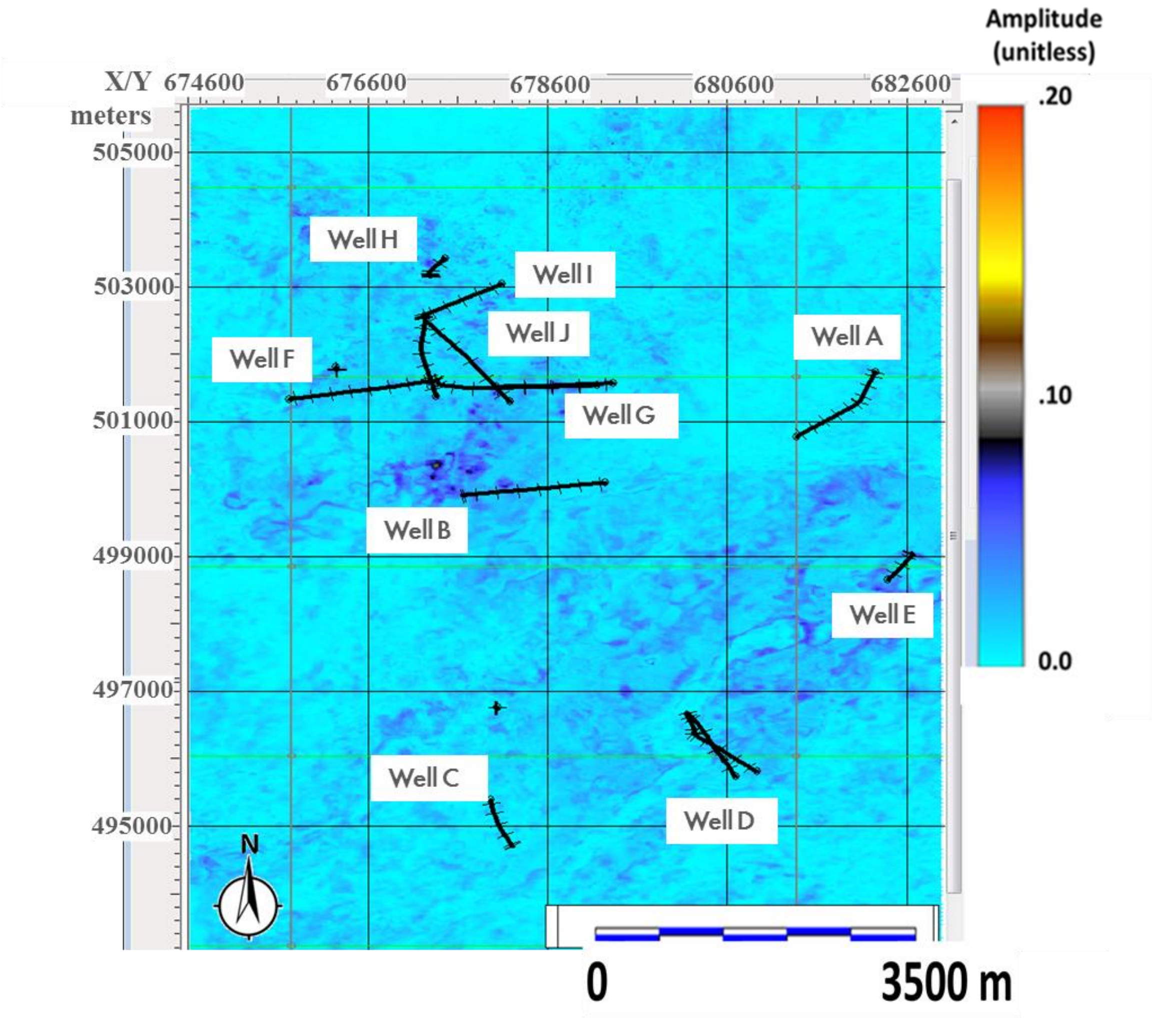

Figure 4.16c: RMS amplitude map on +90° phase component of the bandwidth-extended far stack. Red is high relative amplitude and light blue is low relative amplitude. Black lines are well paths. Solid black circles are bottom hole well locations. The amplitudes are relative and unitless.

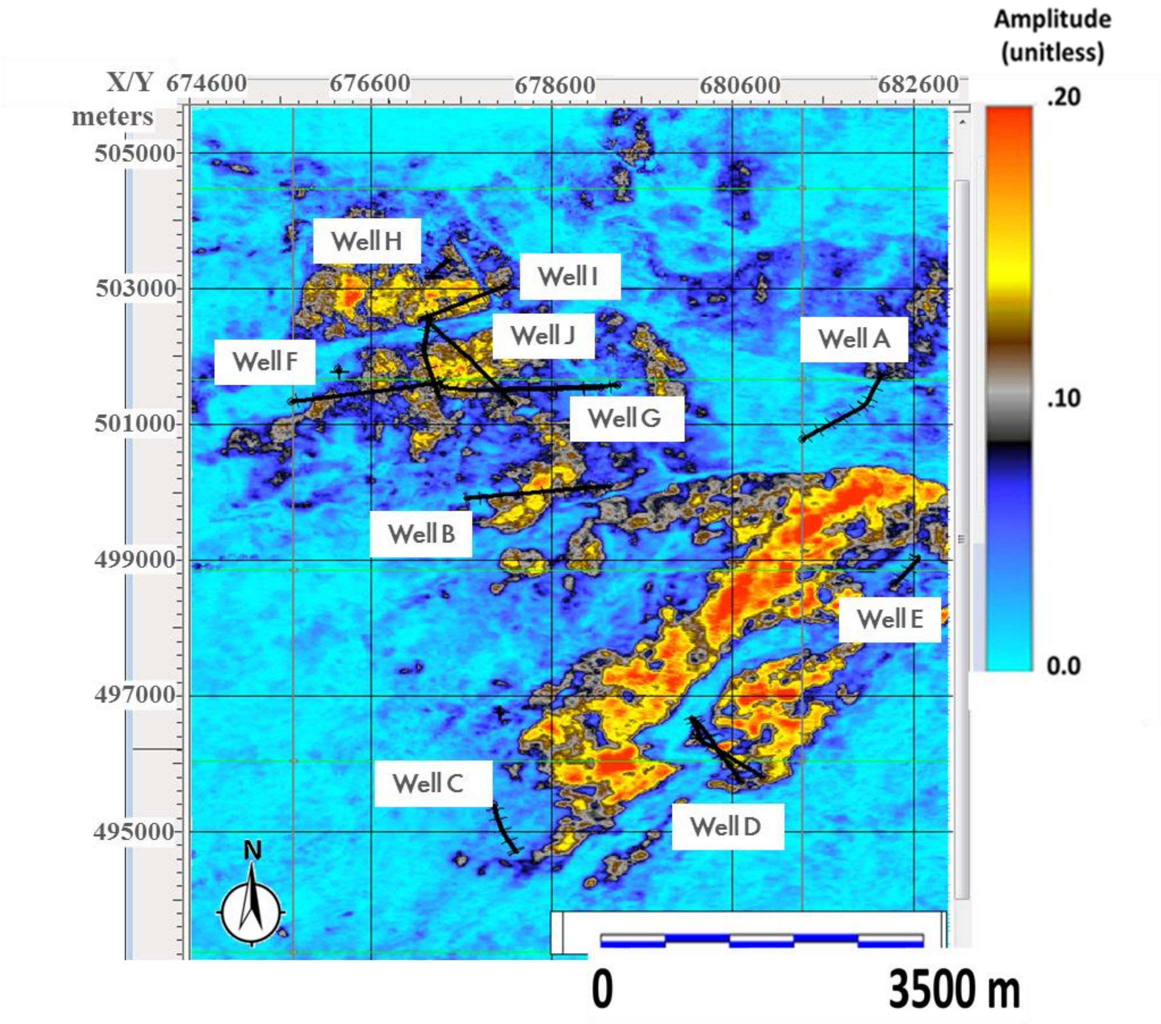

Figure 4.16d: RMS amplitude map on -90° phase component of the bandwidth-extended far stack. Red is high relative amplitude and light blue is low relative amplitude. Black lines are well paths. Solid black circles are bottom hole well locations. The amplitudes are relative and unitless.

CHAPTER FIVE

CONCLUSION

5.1 Sparse-Layer Inversion

Bandwidth extension of seismic data improves reservoir delineation in an offshore Niger Delta oil field. Sparse-layer reflectivity inversion increases the bandwidth and center frequency of the data, thereby compacting the wavelet and reducing side lobe interference. The process also helps to balance frequency spectra between near and far offsets.

Although bandwidth extension degraded well ties, top and base reflectors for previously sub-tuning layers could be identified and interpreted independently, revealing possible thickness changes and prospective drilling locations away from well control (Figures 4.11b and 12d). However well ties are poorer on the bandwidth-extended data than on the original seismic data. Causes for the degradation could be due to a variety of reasons (1) well log errors impacting high frequencies more severely, (2) time-depth and well positioning/projection errors being more significant at high frequencies, with time-depth stretching and squeezing applied to the original seismic data to maximize correlations and not re-adjusted to similarly force ties at high frequency, (3) deviation of the earth impedance structure from a true sparse blocky-earth structure, (4) difficulty in characterizing spectral periodicities for very thin layers within the original seismic band, and (5) general inversion non-uniqueness. Despite these difficulties, the bandwidth-extended data allowed more detailed interpretation of several reflectors in this case study. The effectiveness of the bandwidth extension here, is consistent with the case of anomalously low-impedance sand reservoirs encased in shale satisfying, for the most part, the blocky earth assumption of sparse-layer inversion.

5.2 Phase Decomposition

Amplitudes of the -90° phase component of the original far-offset seismic data show excellent correlation to presence or absence of significant pay at wells (Figure 4.14d). For very thin layers, phase decomposition, though weak at well locations, shows possible thicker reservoir slightly updip or downdip of well locations (Figure 4.16d). Some reservoir layers that are below seismic resolution on the original seismic data are resolved as distinct events from step interfaces after spectral broadening. Furthermore, the very thin layers are readily isolated and extracted by phase decomposition of the bandwidth-extended data. In some instances, sub-tuning pay intervals containing two distinct sands appear as a single seismic event on the original data but as two distinct layer responses on the bandwidth-extended data. This allows independent interpretation of lateral changes in the thicknesses of these previously unresolved sands. Amplitude maps after bandwidth extension reveal greater lateral extent of soft amplitudes suggesting larger reservoir areas than might be interpreted on original amplitude maps (comparing Figure 4.14d with Figure 4.16d). This is presumably due to reduction of tuning related destructive interference for thinner portions of the reservoir.

BIBLIOGRAPHY

Adeoye, T.O., and Enikanselu, P. A., 2009, Hydrocarbon reservoir mapping and volumetric analysis using seismic and borehole data over “Extreme” field, Southwestern Niger Delta: Ozean. J Appl Sci 2(4): p. 429–441

Allen, J.R.L., 1965, Late Quaternary Niger Delta and Adjacent Areas: Sedimentary Environments and Lithofacies: Bull. AAPG., 48, p. 547-600

Backus, M. M., and Chen, R. L., 1975, Flat Spot Exploration: Geophysical Prospecting, 23, no., 3, p. 533-755

Barbato, U., O. Portniaguine, B. Winkelman, and J. Castagna, 2017, Phase decomposition as a DHI in bright-spot regimes - A Gulf of Mexico case study: SEG Technical Program Expanded Abstracts 2017: p. 3976-3980

Burke, K., 1972, Longshore drift, submarine canyons, and submarine fans in development of Niger Delta: American Association of Petroleum Geologists, v. 56, p. 1975-1983

Bracewell, R. N., 1965, The Fourier Transform and its Applications., McGraw-Hill

Brown, A. R., 2011, Interpretation of Three-Dimensional Seismic Data., AAPG Memoir 42 and SEG Investigations in Geophysics, No. 9, AAPG and SEG

Burke, K.C.B., Dessauvagie, T.F.J., and Whiteman, A.J., 1971, The opening of the Gulf of Guinea and the Geological History of the Benue Depression and Niger-Delta: Nature phys. Sci., 233 (38), p. 51-55

Castagna, J., A. Oyem, O. Portniaguine, and U. Aikulola, 2016, Phase decomposition: Interpretation, 4, no. 3, SN1-SN10

de Abreu, E. S., Castagna, J. P., Gil, F., in press, Case study: Phase component amplitude variation with angle: accepted by Geophysics

Domenico, S. N., 1977, Elastic properties of unconsolidated porous sand reservoirs: GEOPHYSICS 42, No. 7, p. 1339-136

Doust, H., and Omatsola, E., 1990, Niger Delta, in, Edwards, J. D., and Santogrossi, P.A., eds., Divergent/passive Margin Basins, AAPG Memoir 48: Tulsa, American Association of Petroleum Geologists, p. 239-248

Ejedawe, J.E., 1981, Patterns of incidence of oil reserves in Niger Delta Basin: American Association of Petroleum Geologists, v. 65, p. 1574-1585

Ejedawe, J.E., Coker, S.J.L., Lambert-Aikhionbare, D.O., Alofe, K.B., and Adoh, F.O., 1984, Evolution of oil-generative window and oil and gas occurrence in Tertiary Niger Delta Basin: American Association of Petroleum Geologists, v. 68, p. 1744-1751

Ekweozor, C. M., and Daukoru, E.M, 1994, Northern delta depobelt portion of the Akata-Agbada(!) petroleum system, Niger Delta, Nigeria, in, Magoon, L.B., and Dow, W.G., eds., The Petroleum System--From Source to Trap, AAPG Memoir 60: Tulsa, American Association of Petroleum Geologists, p. 599-614

Evamy, B.D., Haremboure, J., Kamerling, P., Knaap, W.A., Molloy, F.A., and Rowlands, P.H., 1978, Hydrocarbon habitat of Tertiary Niger Delta: American Association of Petroleum Geologists Bulletin, v. 62, p. 277-298

Hill, S. J., 2005, Inversion-based thickness determination: The Leading Edge, Vol. 24, No. 5, p. 477-480

Hilterman, F. J., 2001, Seismic Amplitude Interpretation., SEG Distinguished Instructor Short Course Notes

Kallweit, R. S., and L. C. Wood, L C., 1982, The limits of resolution of zero-phase wavelets: Geophysics, 47(7), p. 1035-1046

Lancaster, S., and Whitcombe, D., 2000, Fast track coloured inversion. SEG Technical Program Expanded Abstracts, p. 1572–1575

Liang. C., Castagna, J. P., and Zavala-Torres, R., 2017, Spectral bandwidth extension - invention versus harmonic extrapolation: Geophysics, 82, No. 4, p. W1-W16

Merki, P., 1972, Structural geology of the Cenozoic Niger Delta- In: T.F.J. Dessauvagie, and A.J. Whiteman (Eds): African Geology-Ibadan Univ. Press, p. 635-646

Meza, R., G. Haughey, J. Castagna, U. Barbato, and O. Portniaguine, 2016, Phase decomposition as a hydrocarbon indicator - a case study: SEG Technical Program Expanded Abstracts, p. 1839-1843

Murat, R.C., 1972, Stratigraphy and Paleogeography of the cretaceous and Lower Tertiary in Southern Nigeria. in T.F.G. Dessauvagie and A.J. Whitman eds., African Geology. University of Ibadan. p. 251-266

Nwachukwu, J.I., and Chukwurah, P. I., 1986, Organic matter of Agbada Formation, Niger Delta, Nigeria: American Association of Petroleum Geologists Bulletin, v. 70, p. 48-55

Opara, A. I., 2010, Prospectivity evaluation of "Usso Field", onshore Niger Delta basin using 3-D seismic and well log data: Petrol Coal 52(4): p. 307–315

Orife, J.M., and Avbovbo, A.A., 1982, Stratigraphic and unconformity traps in the Nigeria Delta: AAPG Bulletin, vol. 66 (2). p. 251-262

Ostrander, W. J., 1984, Plane-wave reflection coefficients for gas sands at nonnormal angles of incidence: GEOPHYSICS, 49, No. 10, p. 1637-1648

Oyeyemi, K. D., Olowokere, M. T., and Aizebeokhai, A. P., 2018, Hydrocarbon resource evaluation using combined petrophysical analysis and seismically derived reservoir characterization offshore Niger Delta: J. Petrol. Explor. Prod. Technol., 8: p. 99–115

Peterson R.A., Fillippone, W.R., and Coker, F.B., 1955, The Synthesis of seismograms from well log data: Geophysics, Vol. XX, No. 3, p. 516 - 538

Puryear, C. I., and Castagna, J. P., 2008, Layer-thickness determination and stratigraphic interpretation using spectral inversion - Theory and application: Geophysics, 73, No. 2, p. R37-R4

Reed, K.J., 1969, Environment of deposition of source beds of high-wax oil: American Association of Petroleum Geologists Bulletin, v. 53, p. 1502-1506

Reijers, T.J.A., Petter, S.W., and Nwajide, C.S., 1996, The Niger Delta basin: In Reijers, T.J.A., ed.,: Selected Chapter on Geology: SPDC Warri. p. 103-118

Roden, R., and Forrest, M., 2005, The impact of seismic amplitudes on prospect risk analysis: SEG Technical Program Expanded Abstracts, p. 1572–1575

Short, K. C., and Stäuble, A.J., 1967, Outline of geology of Niger Delta: American Association of Petroleum Geologists Bulletin, v. 51, p. 761-779

Smith, M., G. Perry, J. Stein, A. Bertrand, and G. Yu, 2008, Extending seismic bandwidth using the continuous wavelet transform: First Break, 26, p. 97-102

Stacher, P., 1995, Present understanding of the Niger Delta hydrocarbon habitat, in, Oti, M.N., and Postma, G., eds., Geology of Deltas: Rotterdam, A.A. Balkema, p. 257-267

Tuttle, M.L.W., Charpentier, R.R., and Brownfield, M.E., 1999, The Niger Delta petroleum system: Niger Delta province, Cameroon, and Equatorial Guinea, Africa: http://greenwood.cr.usgs.gov/energy/WorldEnergy/OF99-50H/ChapterA.html#TOP

Weber, K.J., 1971, Sedimentological aspects of Oil fields in the Niger-Delta: Geol.en Mijnb., vol. 50 (3). p. 559-576

Weber, K. J., and Daukoru, E.M., 1975, Petroleum geology of the Niger Delta: Proceedings of the Ninth World Petroleum Congress, volume 2, Geology: London, Applied Science Publishers, Ltd., p. 210-221

Wiener, N. (1964), Extrapolation, Interpolation, and Smoothing of Stationary Time Series, Cambridge, Mass: MIT Press., ISBN 0-262-73005-7

Whiteman, A., 1982, Nigeria: Its Petroleum Geology, Resources and Potential: London, Graham and Trotman, p. 394

Widess, M. B., 1973, How thin is a thin bed? Geophysics, 38(6), p. 1176-1180

Yu, G., Smith, M., Wojslaw, B., and Stein, J., 2012, Multi-dimensional high-resolution imaging for accurate interpretation and reservoir characterization: SEG Technical Program Expanded Abstracts p. 1-5

Zhang, R., and J. P. Castagna, 2011, Seismic sparse-layer reflectivity inversion using basis pursuit decomposition: Geophysics, 76, no. 6, R147–R158

Zhang, R., Sen, M. K., Srinivasan, S., 2013, A prestack basis pursuit seismic inversion: Geophysics, 78, No. 1, p. R1-R11

APPENDIX A

Proof of the Additive Property of Reflection Coefficients

In interpreting phase decomposition, it is assumed that reflection coefficients are additive, such that the odd and even parts of a layer reflectivity series can be separated. This is not necessary to perform phase decomposition, but, is needed to interpret phase decomposition results in terms of reflection coefficients and impedance contrasts. The additive property of reflection coefficients is readily proved using Peterson's approximation (Peterson et al., 1955):

$$R \approx .5\ \Delta \ln(I)$$

where, R, is the reflection coefficient and, I, is layer impedance. The approximation is acceptable for reflection coefficients smaller than about .5. As reservoir reflection coefficients are rarely if ever this large, even for bright spots, it is safe for us to use in our application.

Next, consider the case of a layer inserted between two half-spaces (Figure 1.4) and consider the relationship between the reflection coefficients at the interfaces. The upper half space has an impedance of I_1 and the lower half-space an impedance of I_3 with the intermediate layer having an impedance of I_2. One can ask the question: Is it true that reflection coefficient R_C is approximately equal to the sum of the reflection coefficients at the top, R_T, and base, R_B, of the inserted layer?

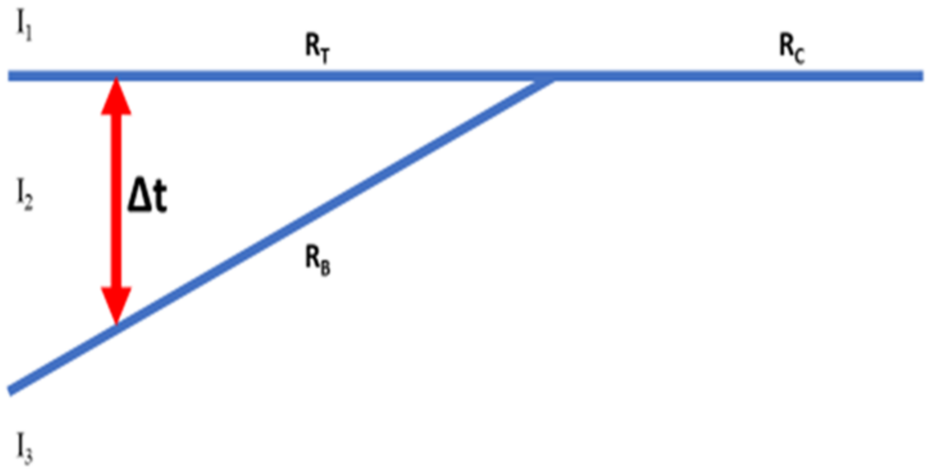

Figure A-1: A layer of time thickness Δt of impedance I_2 is inserted between half spaces with impedance I_1 above the layer and I_3 below the layer. The reflection coefficients are R_T at the top of the layer, R_B at the base of the layer, and R_C when the layer is zero thickness.

Substituting impedances into Peterson's equation:

$$R_C \approx .5(\ln(I_3) - \ln(I_1)),$$

$$R_T \approx .5(\ln(I_2) - \ln(I_1)), \text{ and}$$

$$R_B \approx .5(\ln(I_3) - \ln(I_2)).$$

To prove:

$$R_C \approx R_T + R_B.$$

By substitution this gives:

$$.5(\ln(I_3) - \ln(I_1)) \approx .5(\ln(I_2) - \ln(I_1)) + .5(\ln(I_3) - \ln(I_2))$$

Simplifying:

$$\ln(I_3) - \ln(I_1) \approx \ln(I3) - \ln(I_1). \qquad \text{Q.E.D.}$$

The additive approximation is proved.

To make the additive property relevant to odd and even separation, let Δt approach zero to see that any reflection can be represented as a sum of partial impedance contrasts. The Peterson et al., (1955) approximation thus lets us further understand the odd-even separation of reflection coefficients as a similar separation of impedances. As the reflection coefficient operator involves a 90° phase shift, it is apparent that the odd and even components of reflectivity correspond to the even and odd components of impedance. In other words, a symmetrical impedance profile (as results from a uniform layer inserted between two half-spaces with the same impedance), results in an odd reflectivity series (an odd impulse pair in the case of the same inserted layer). Similarly, an odd impedance profile has an even reflectivity series. One can thus arrive at the reflectivity phase components by directly separating the reflectivity series into odd and even parts using Bracewell's (1965) formulae as done in the body of this dissertation, or by separating the impedance profile into even and odd parts and calculating corresponding odd and even reflection coefficients (R_E and R_O). This is illustrated in Figure 1.5.

From Odd and Even Traces to Phase Components

Another issue is the separation of odd or even traces into phase components. This is readily performed because each odd or even trace is a superposition of positive phase or negative phase waveforms (see Figure 1.6). The odd trace can be decomposed into a trace with only -90° waveforms and a trace with only 90° waveforms. This is a simple matter of inspecting the odd trace and at each instantaneous amplitude maximum, recognizing the two main lobes of the waveform and determining if the leading lobe is positive or negative. If negative, it is -90° and added to the -90° phase component trace. Similarly, if the leading lobe is positive, the waveform is added to the +90° phase component trace. For the even trace, if the main lobe is positive the waveform is added to the 0° phase component trace, and if negative, the waveform is added to the 180° phase component trace. Alternatively, for each arrival, one can simply compute the instantaneous phase at the instantaneous amplitude maximum to ascertain if the phase of the waveform is positive or negative.

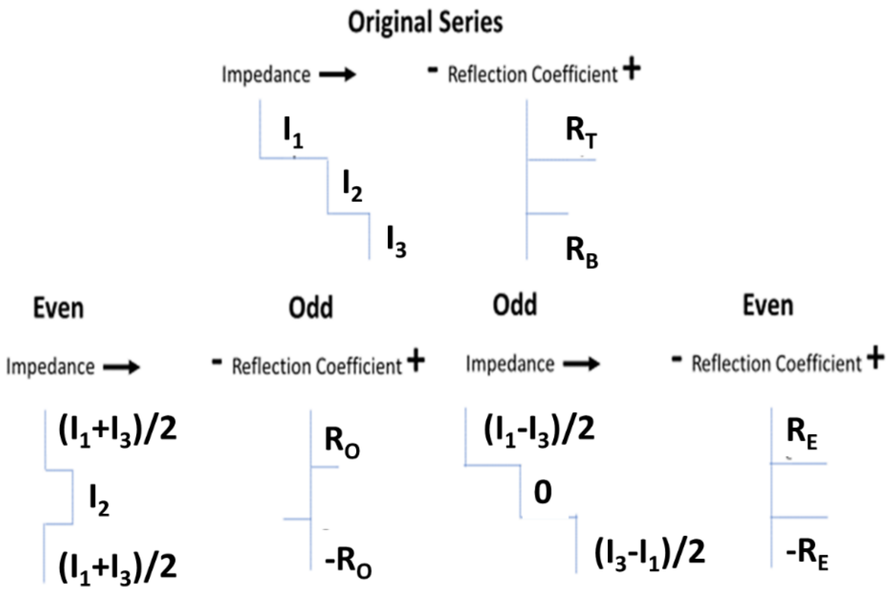

Figure A-2: Schematic relationship between impedance time series and reflectivity time series. The original impedance profile (I_1, I_2, I_3) has a reflection coefficient at the top of the intermediate later, R_T, and at the base of the layer, R_B. The impedance profile has an even part ((I_1 +I_3)/2, I_2, (I_1+I_3)/2)) and an odd part ((I_1-I_3)/2, 0, (I_3-I_1)/2). The even impedance profile has an odd reflectivity series (R_O, -R_O) and the odd impedance profile has an even reflectivity series (R_E, -R_E).

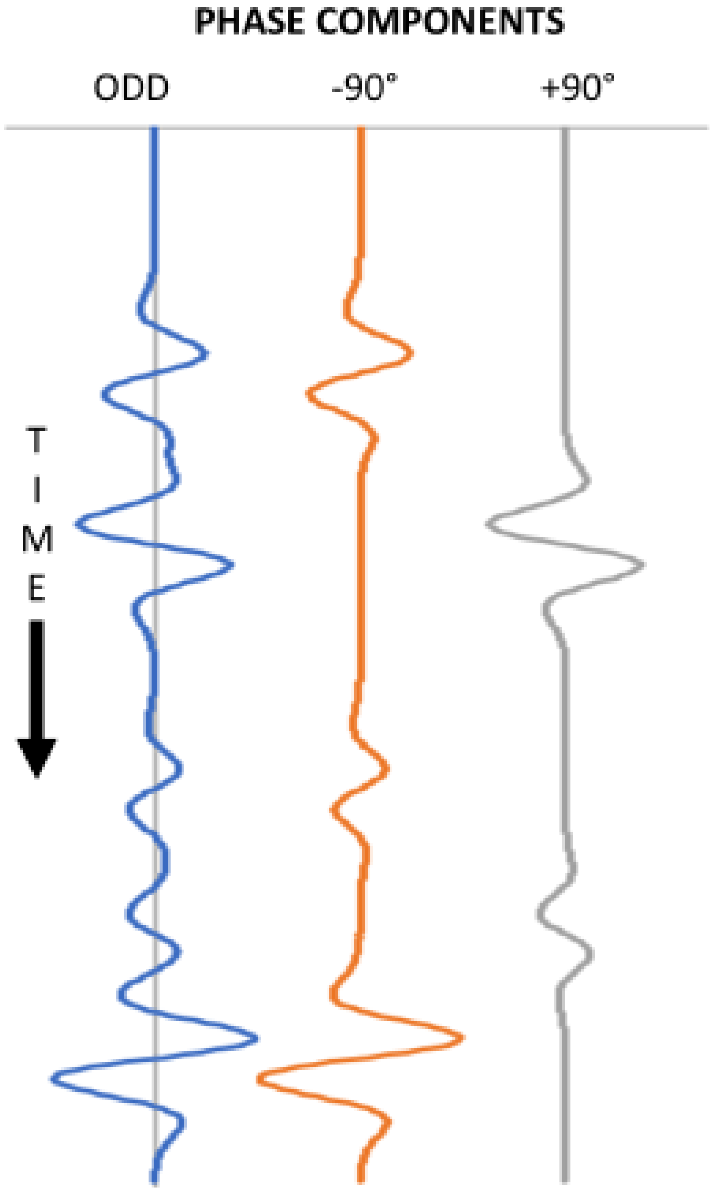

Figure A-3: Example of decomposition of a trace comprised of odd waveforms into 90° and -90° phase component traces by recognizing if the phases of arrivals are positive or negative. The original odd trace is blue. The sum of 90° waveforms is orange. The sum of -90° waveforms is gray.

APPENDIX B

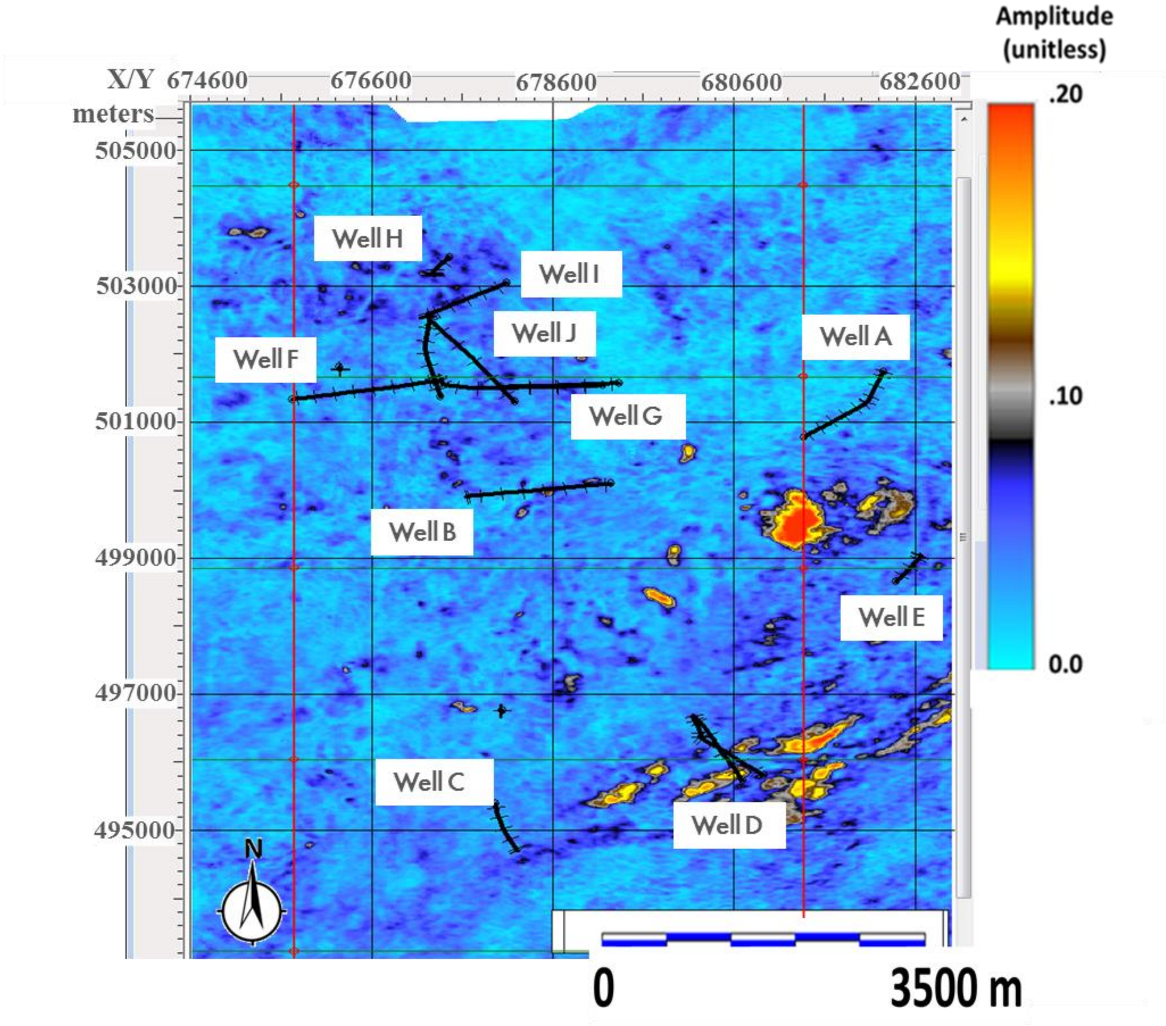

Figure B-1a: RMS amplitude map of ''Orange'' reservoir unit on original near stack. Red is high relative amplitude and light blue is low relative amplitude. Black lines are well paths. Solid black circles are bottom hole well locations. The amplitudes are relative and unitless.

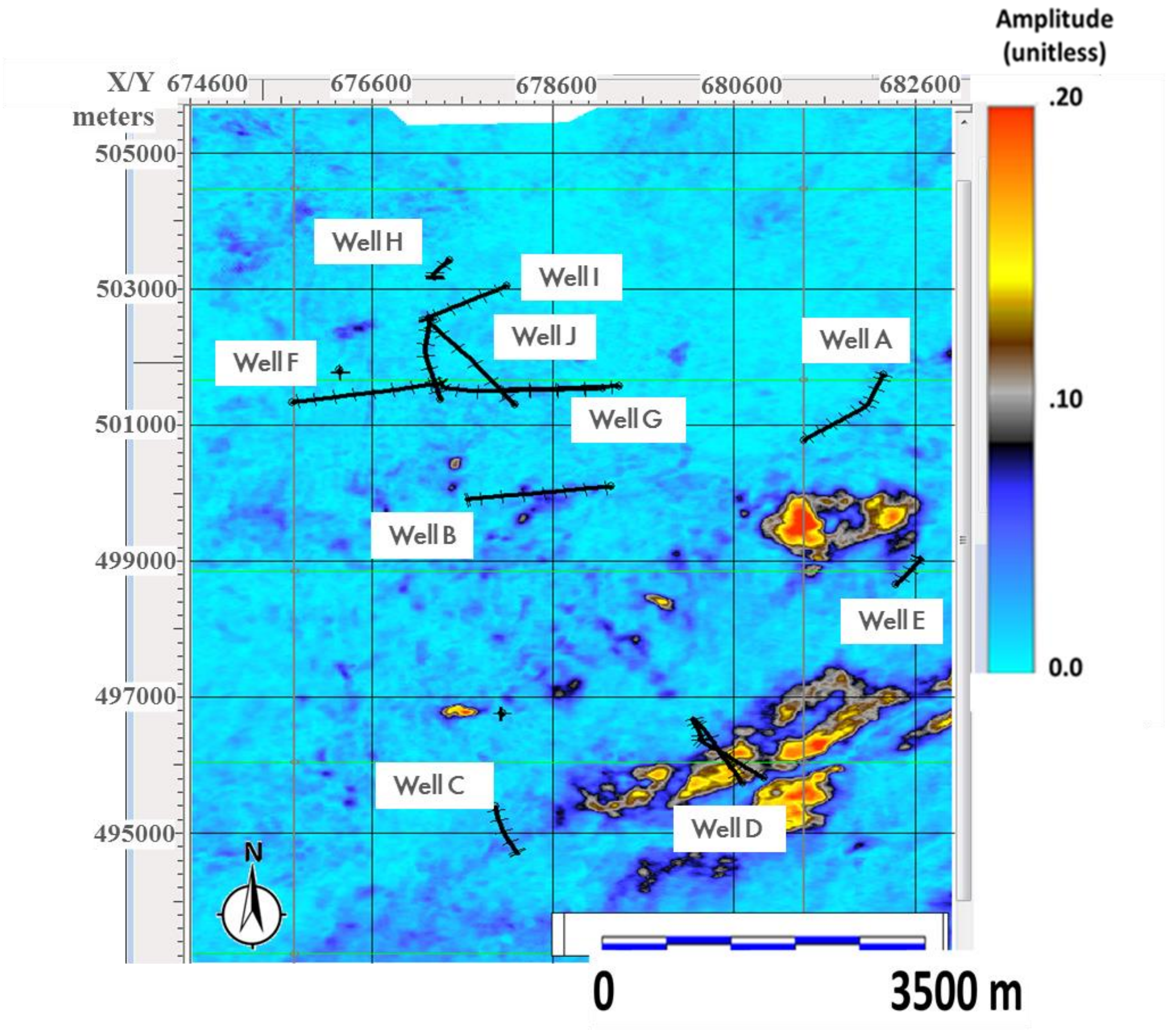

Figure B-1b: RMS amplitude map of ''Orange'' reservoir unit on original far stack. Red is high relative amplitude and light blue is low relative amplitude. Black lines are well paths. Solid black circles are bottom hole well locations. The amplitudes are relative and unitless.

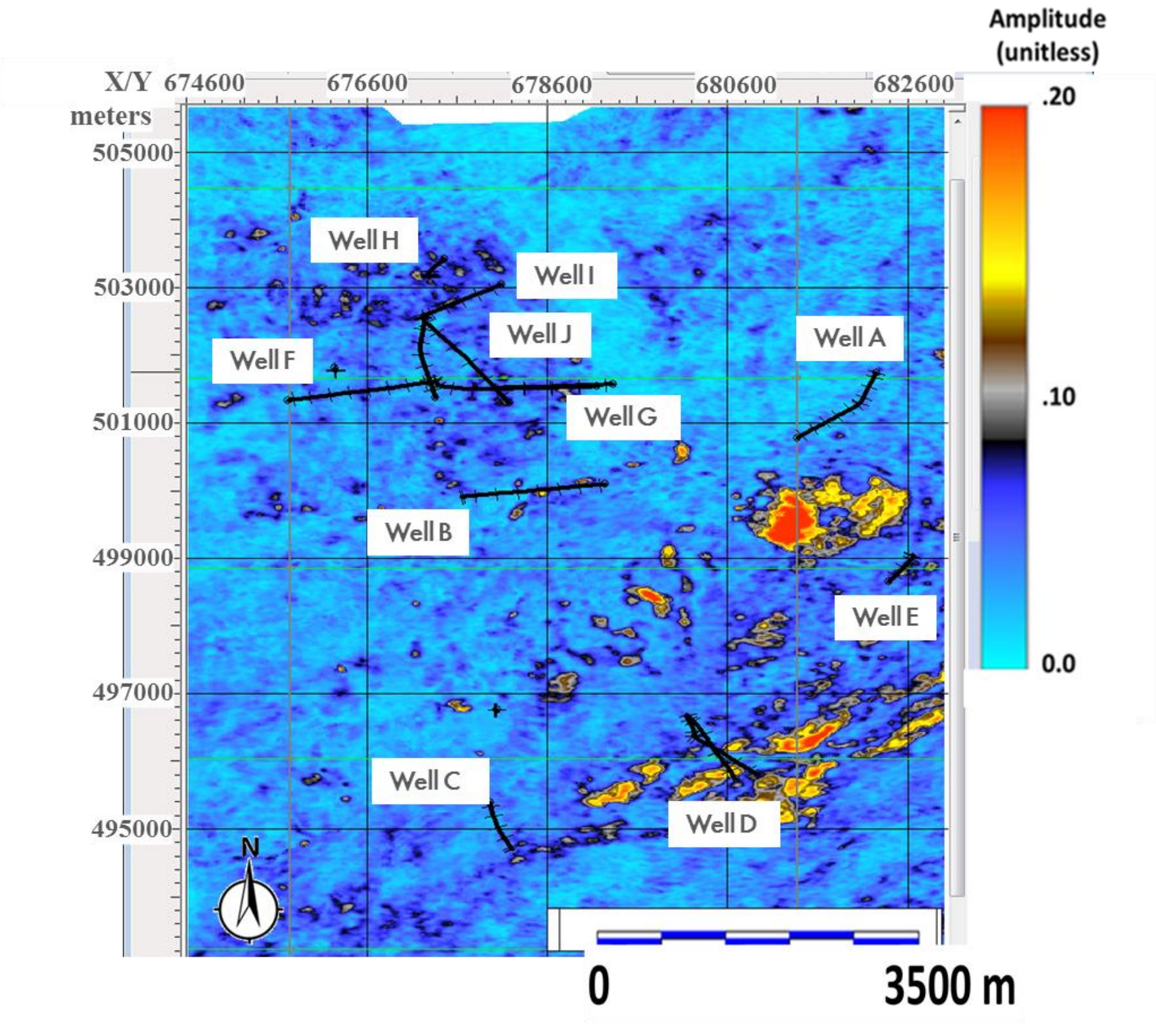

Figure B-1c: RMS amplitude map of ''Orange'' reservoir unit on bandwidth-extended near stack. Red is high relative amplitude and light blue is low relative amplitude. Black lines are well paths. Solid black circles are bottom hole well locations. The amplitudes are relative and unitless.

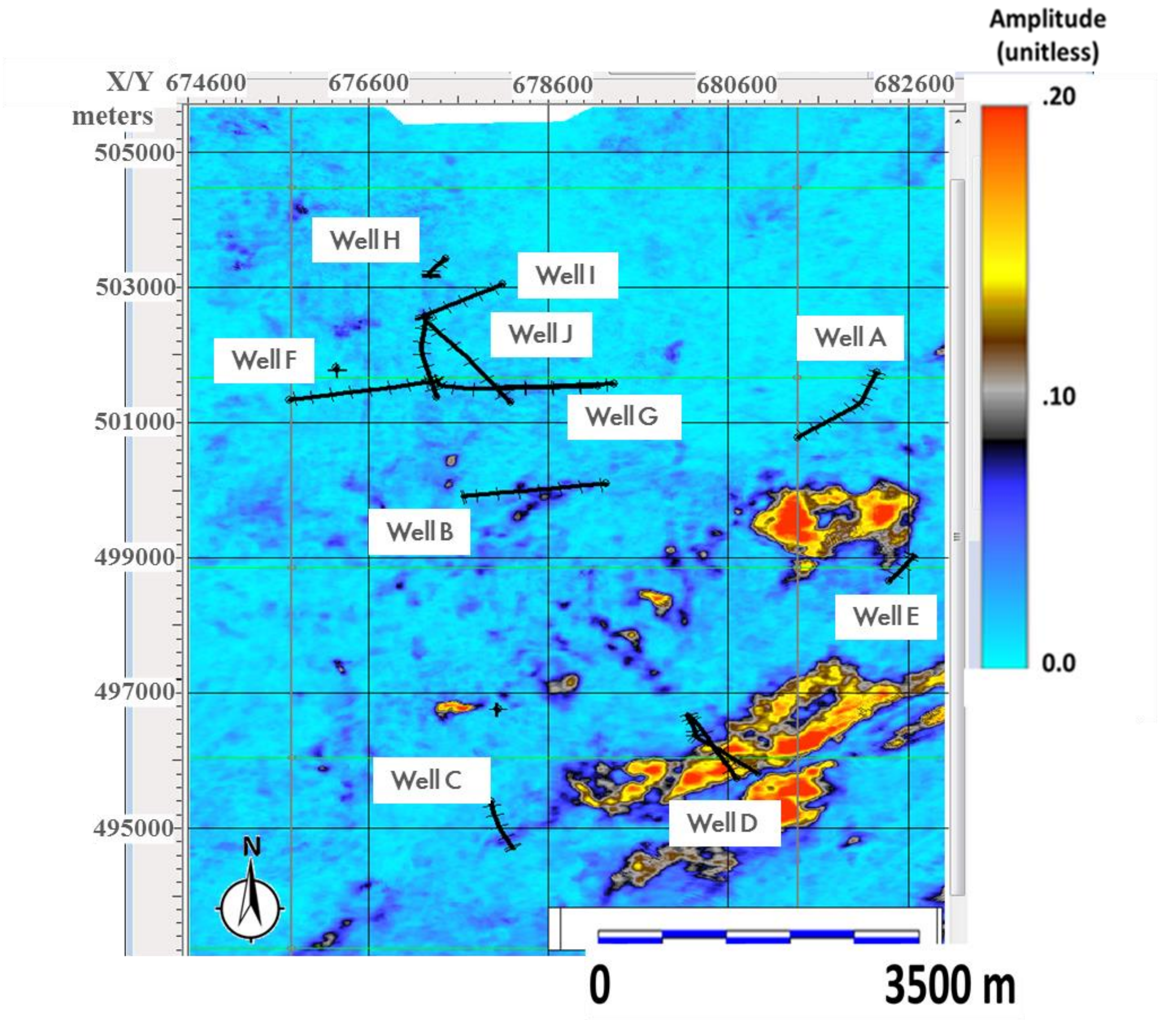

Figure B-1d: RMS amplitude map of ''Orange'' reservoir unit on bandwidth-extended far stack. Red is high relative amplitude and light blue is low relative amplitude. Black lines are well paths. Solid black circles are bottom hole well locations. The amplitudes are relative and unitless.

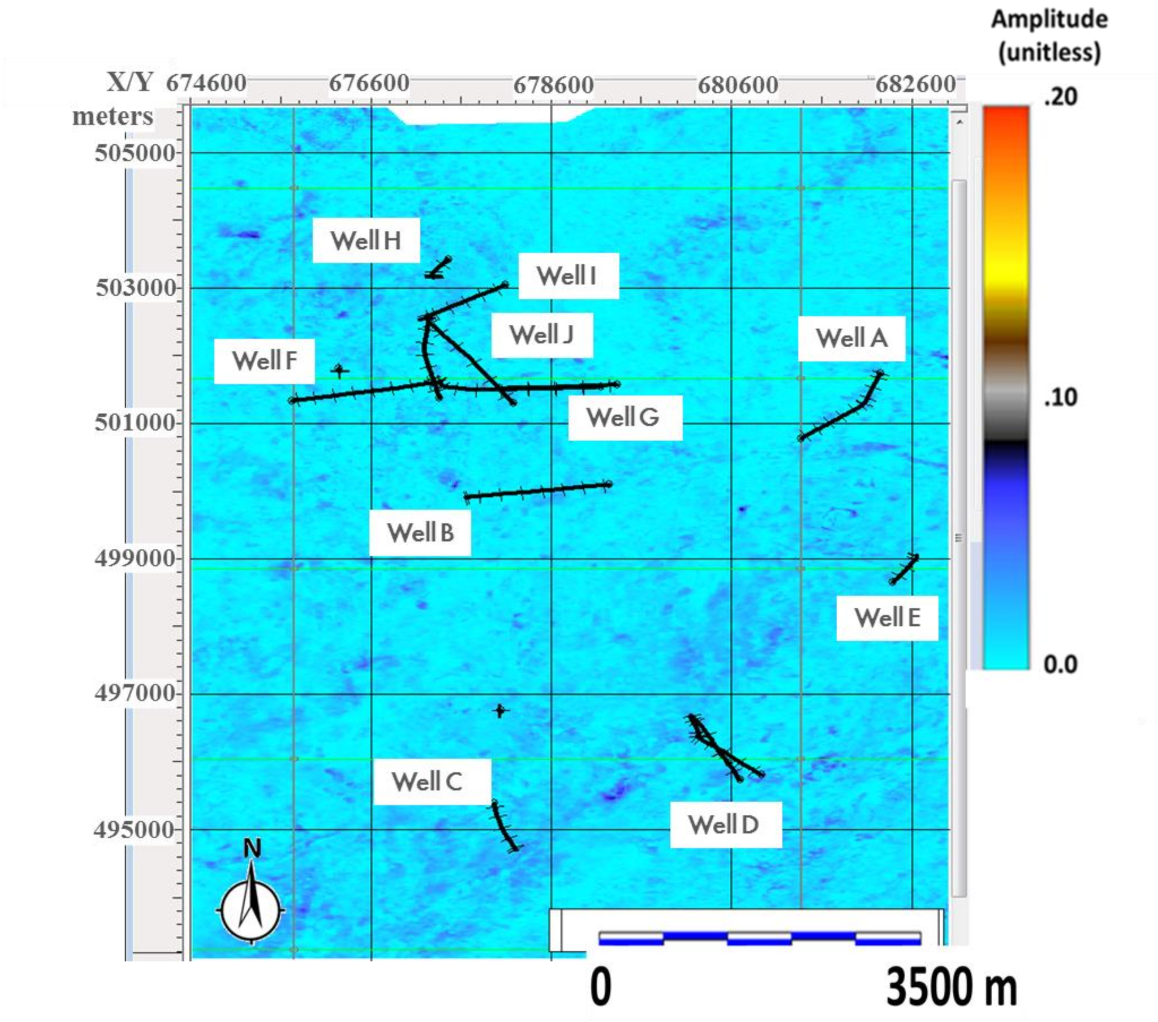

Figure B-2a: RMS amplitude map of ''Orange'' reservoir unit on 0° phase component of original near stack. Red is high relative amplitude and light blue is low relative amplitude. Black lines are well paths. Solid black circles are bottom hole well locations. The amplitudes are relative and unitless.

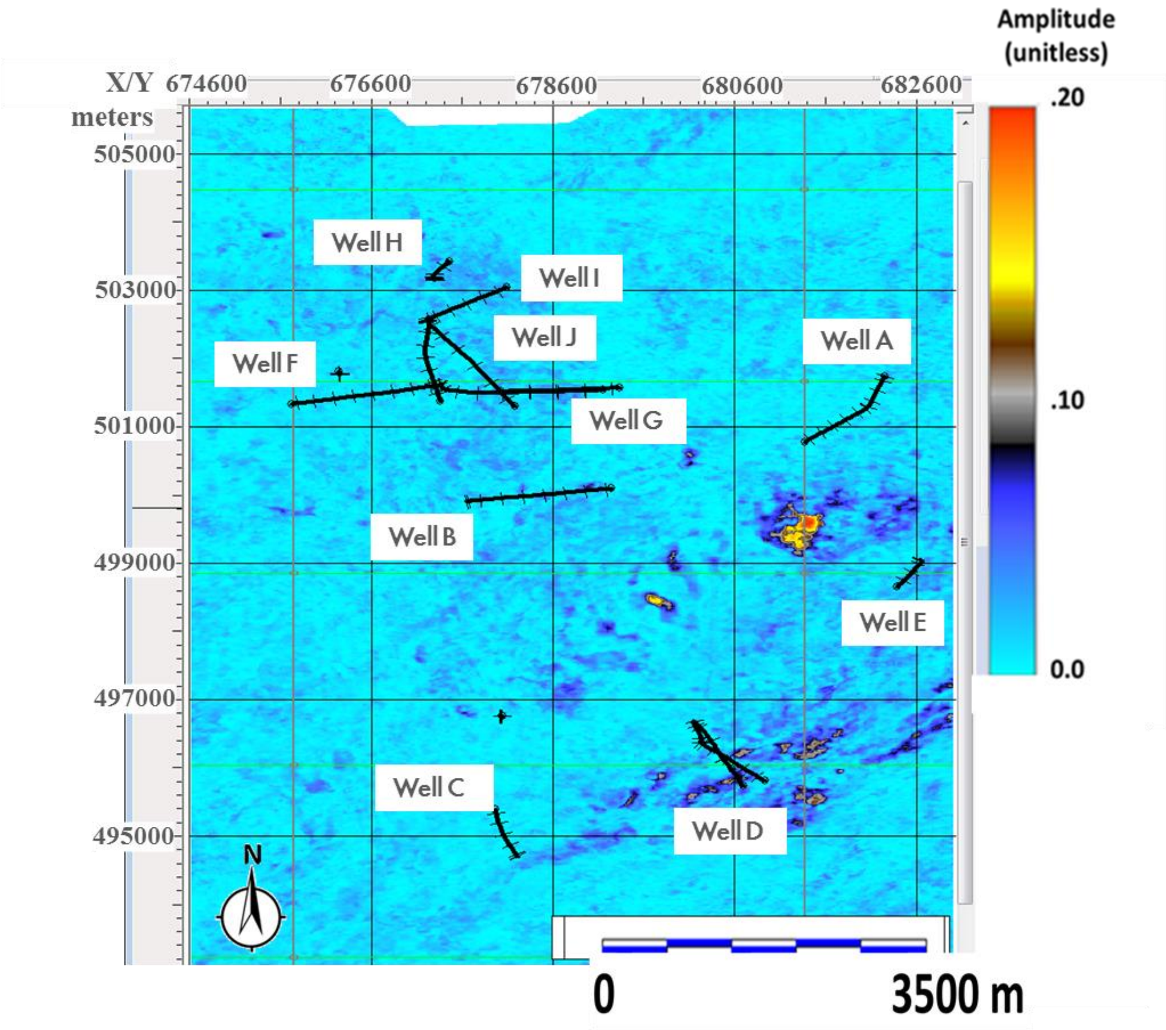

Figure B-2b: RMS amplitude map of ''Orange'' reservoir unit on 180° phase component of original near stack. Red is high relative amplitude and light blue is low relative amplitude. Black lines are well paths. Solid black circles are bottom hole well locations. The amplitudes are relative and unitless.

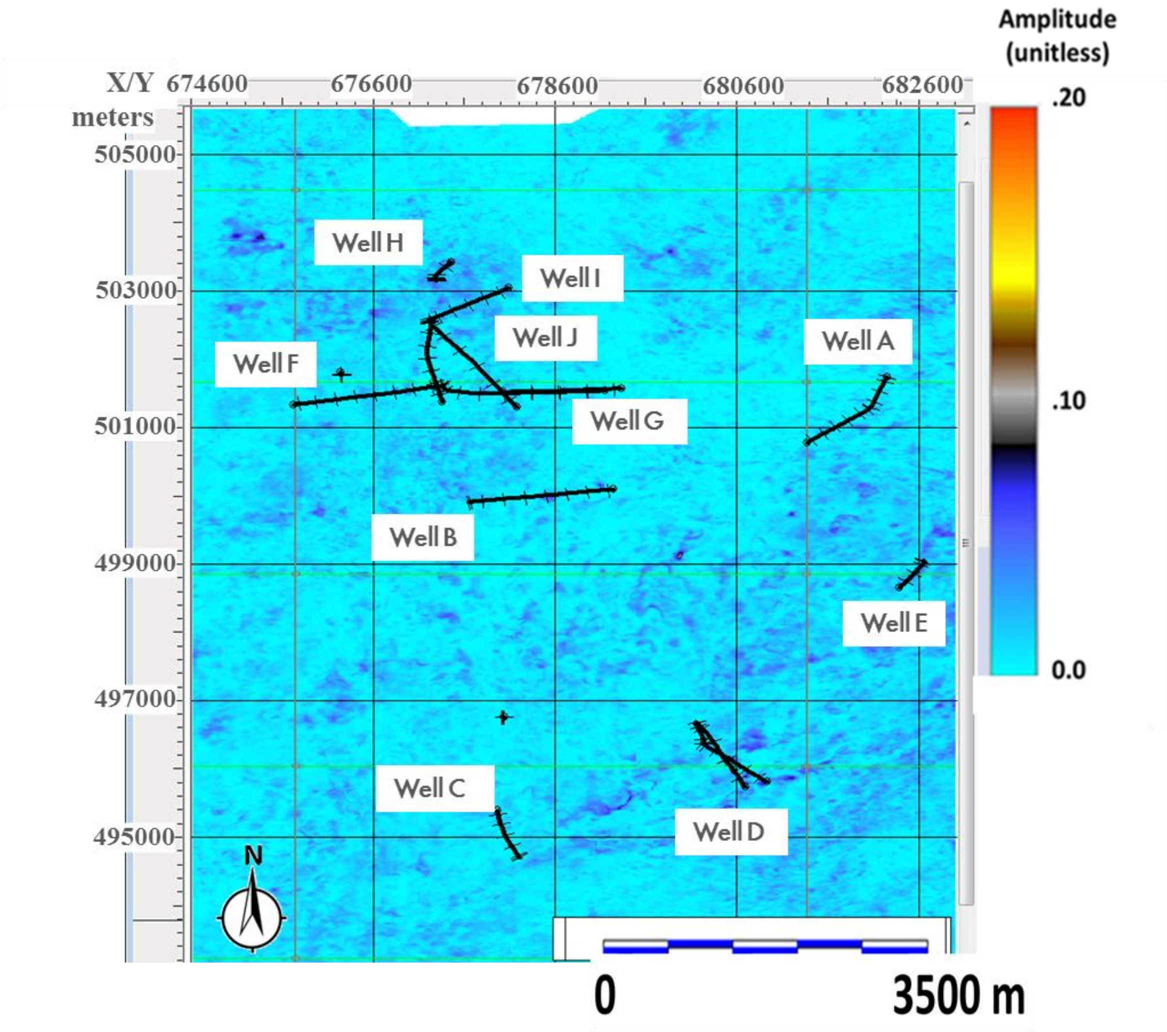

Figure B-2c: RMS amplitude map of ''Orange'' reservoir unit on +90° phase component of original near stack. Red is high relative amplitude and light blue is low relative amplitude. Black lines are well paths. Solid black circles are bottom hole well locations. The amplitudes are relative and unitless.

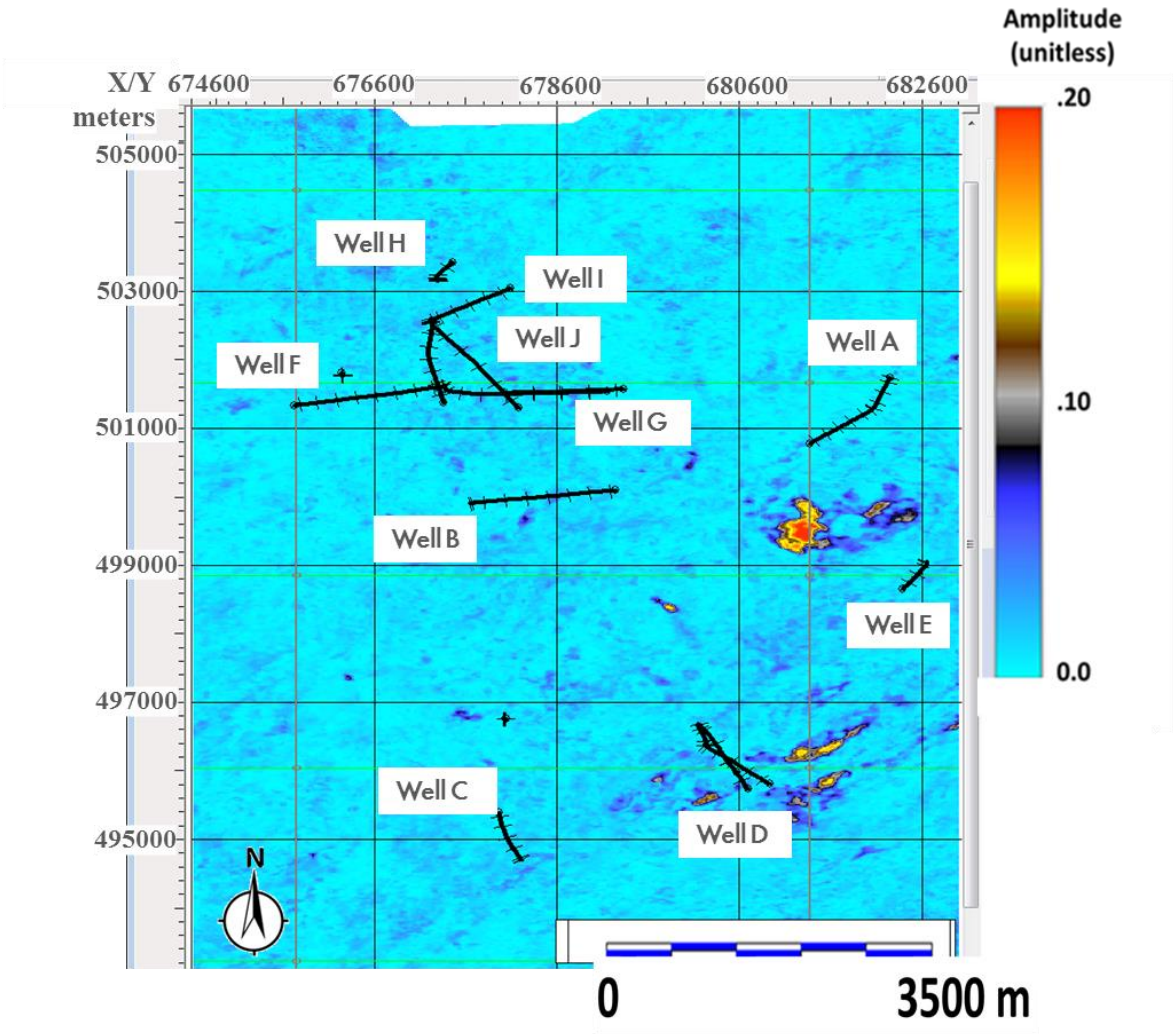

Figure B-2d: RMS amplitude map of ''Orange'' reservoir unit on -90° phase component of original near stack. Red is high relative amplitude and light blue is low relative amplitude. Black lines are well paths. Solid black circles are bottom hole well locations. The amplitudes are relative and unitless.

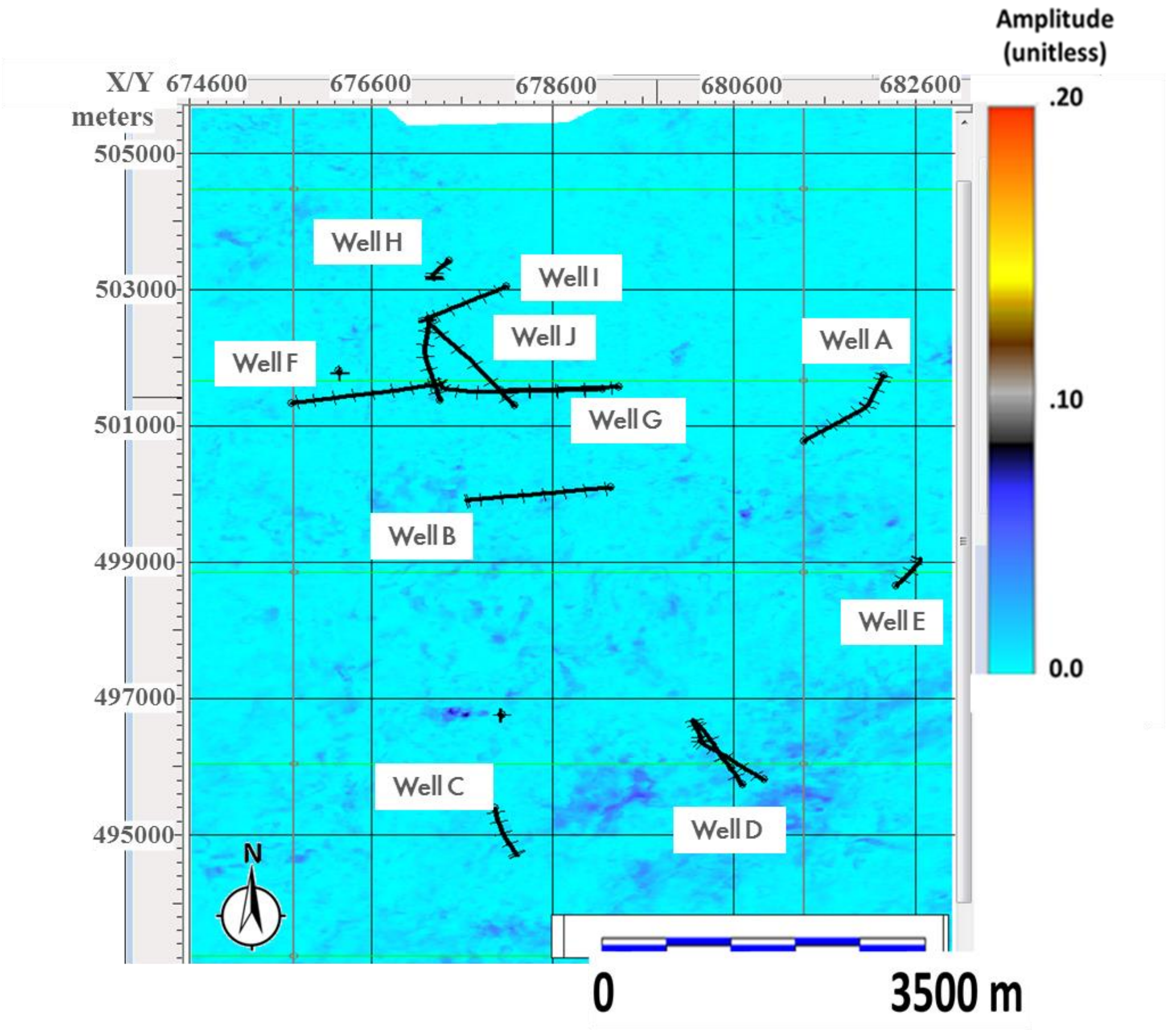

Figure B-3a: RMS amplitude map of ''Orange'' reservoir unit on 0° phase component of original far stack. Red is high relative amplitude and light blue is low relative amplitude. Black lines are well paths. Solid black circles are bottom hole well locations. The amplitudes are relative and unitless.

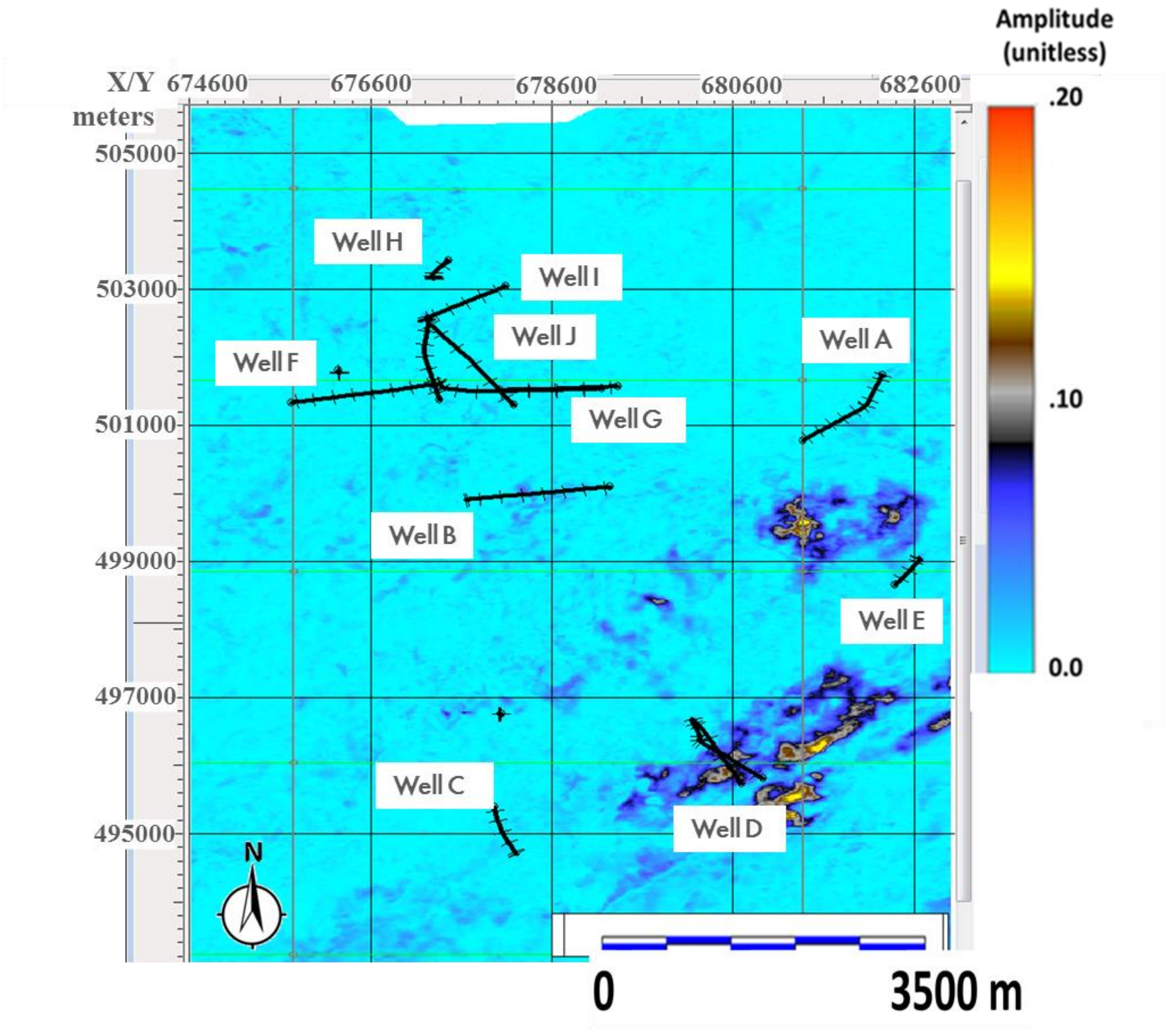

Figure B-3b: RMS amplitude map of ''Orange'' reservoir unit on 180° phase component of original far stack. Red is high relative amplitude and light blue is low relative amplitude. Black lines are well paths. Solid black circles are bottom hole well locations. The amplitudes are relative and unitless.

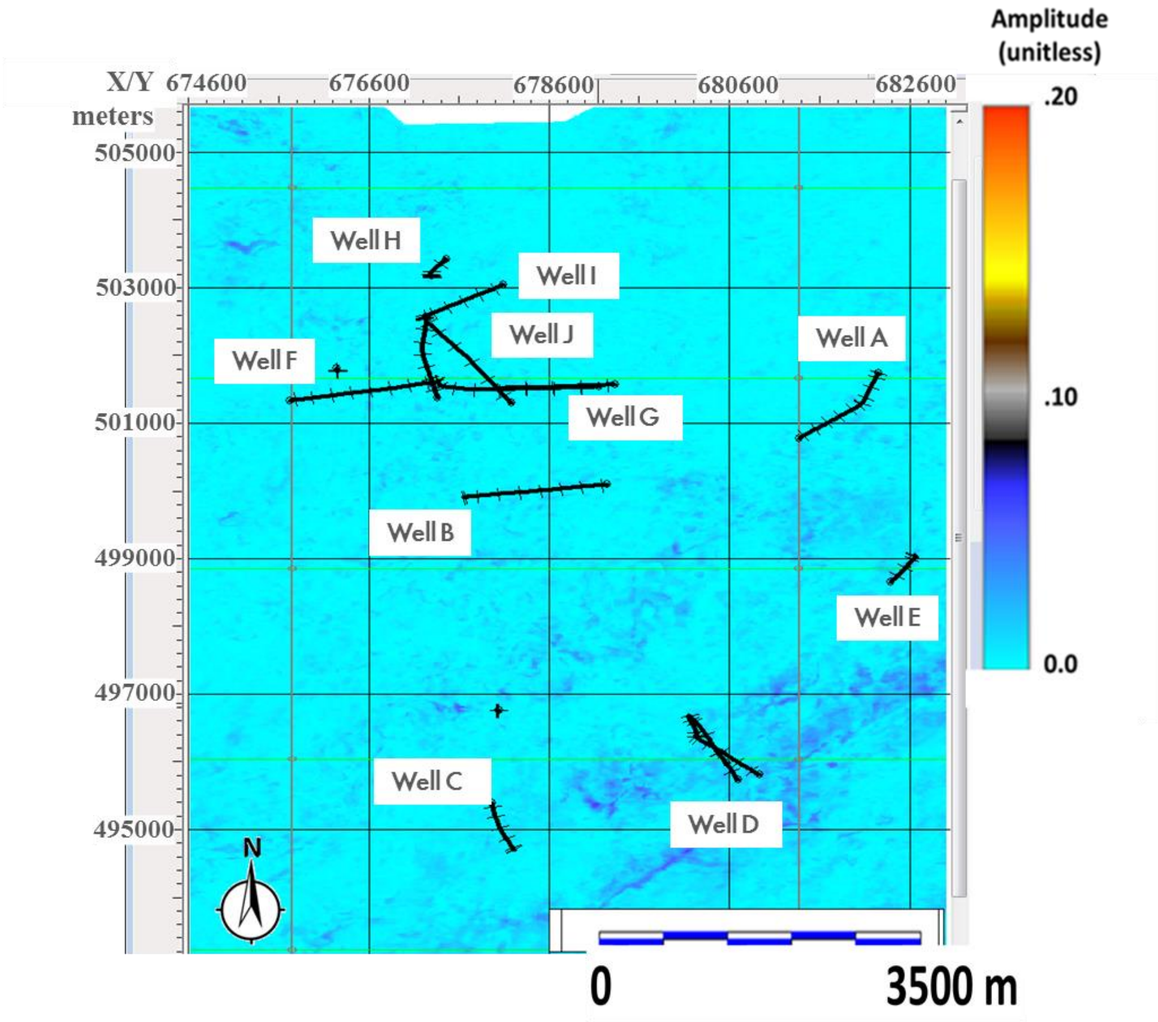

Figure B-3c: RMS amplitude map of ''Orange'' reservoir unit on +90° phase component of original far stack. Red is high relative amplitude and light blue is low relative amplitude. Black lines are well paths. Solid black circles are bottom hole well locations. The amplitudes are relative and unitless.

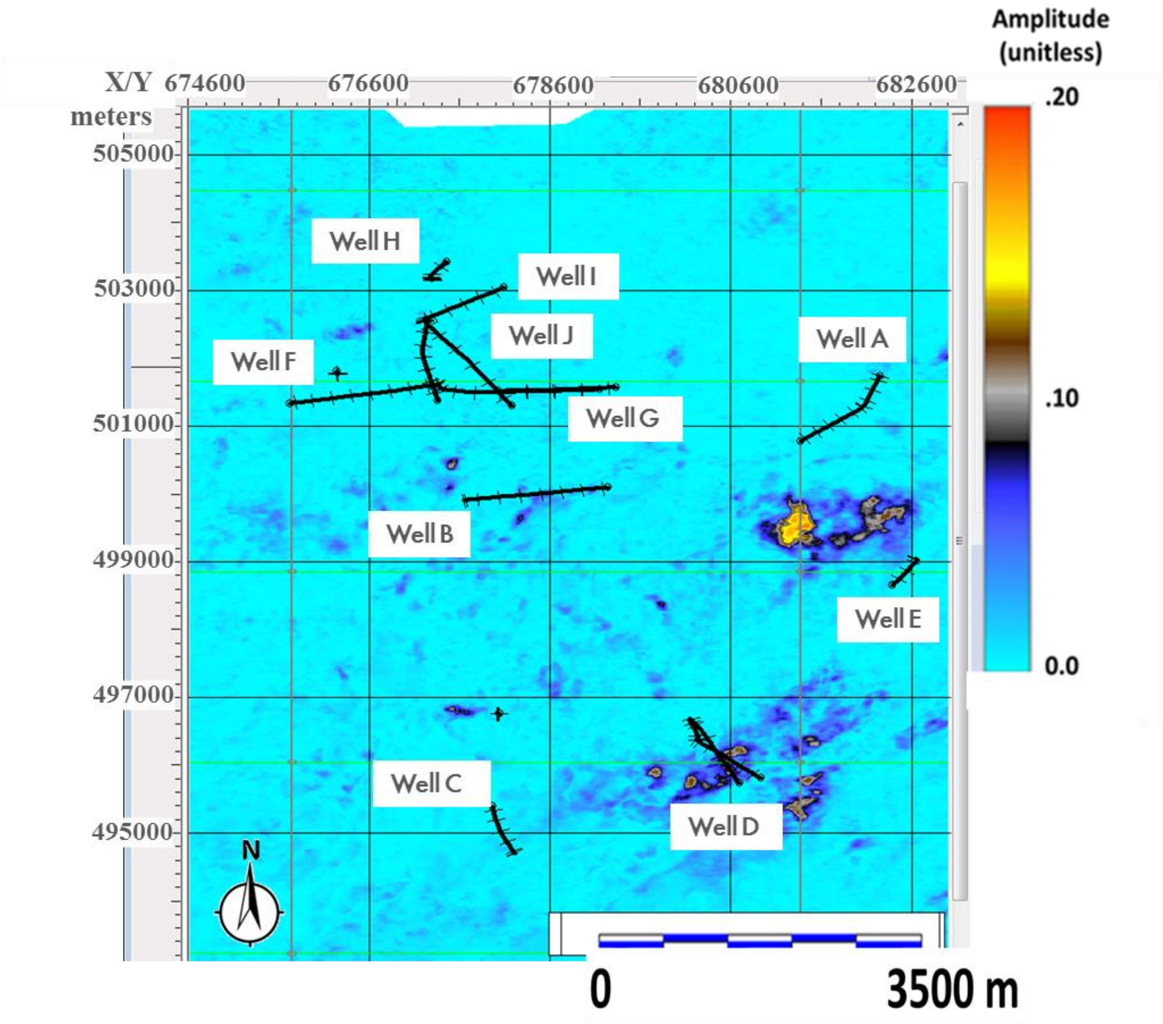

Figure B-3d: RMS amplitude map of ''Orange'' reservoir unit on -90° phase component of original far stack. Red is high relative amplitude and light blue is low relative amplitude. Black lines are well paths. Solid black circles are bottom hole well locations. The amplitudes are relative and unitless.

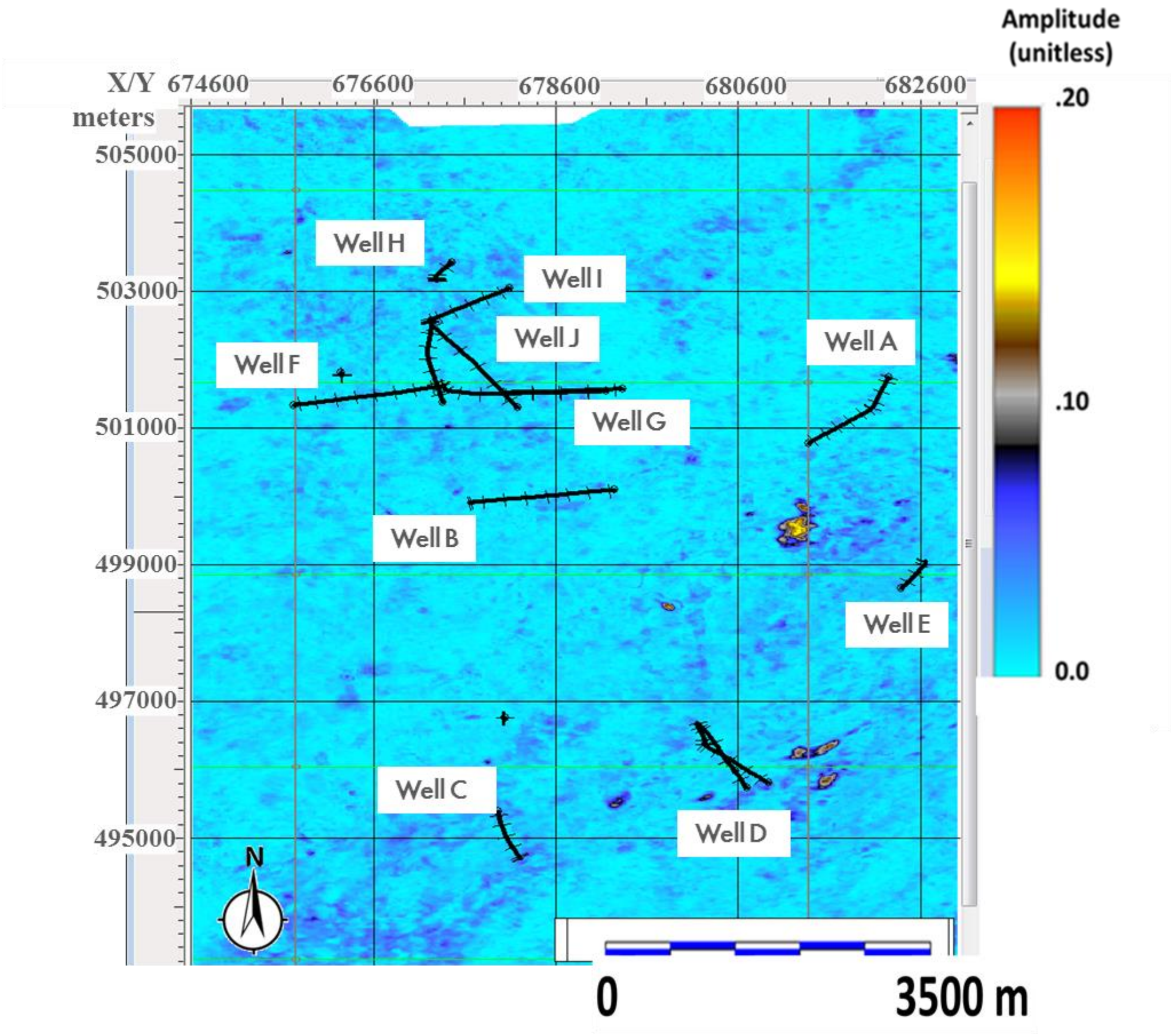

Figure B-4a: RMS amplitude map of ''Orange'' reservoir unit on 0° phase component of bandwidth-extended near stack. Red is high relative amplitude and light blue is low relative amplitude. Black lines are well paths. Solid black circles are bottom hole well locations. The amplitudes are relative and unitless.

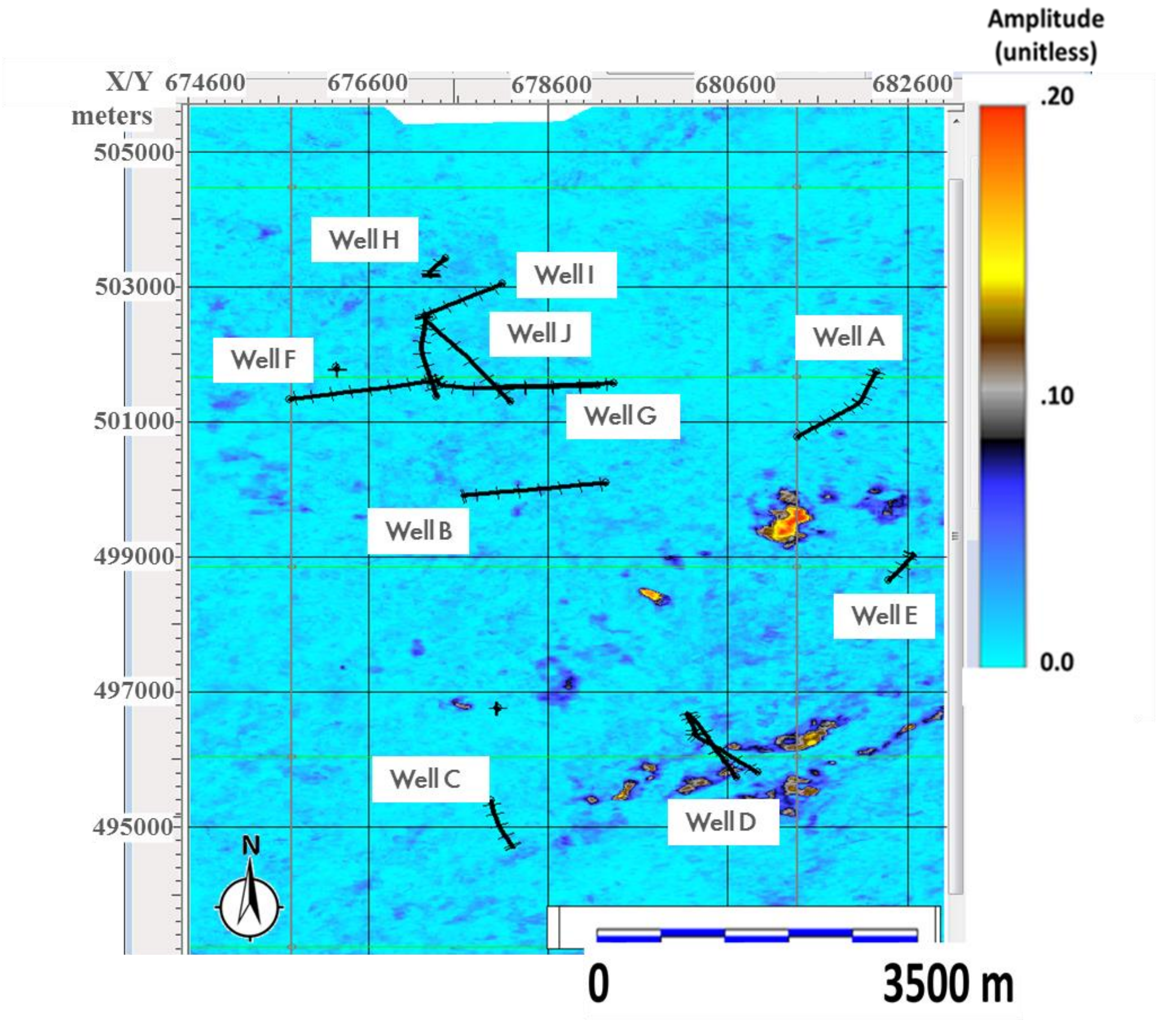

Figure B-4b: RMS amplitude map of ''Orange'' reservoir unit on 180° phase component of bandwidth-extended near stack. Red is high relative amplitude and light blue is low relative amplitude. Black lines are well paths. Solid black circles are bottom hole well locations. The amplitudes are relative and unitless.

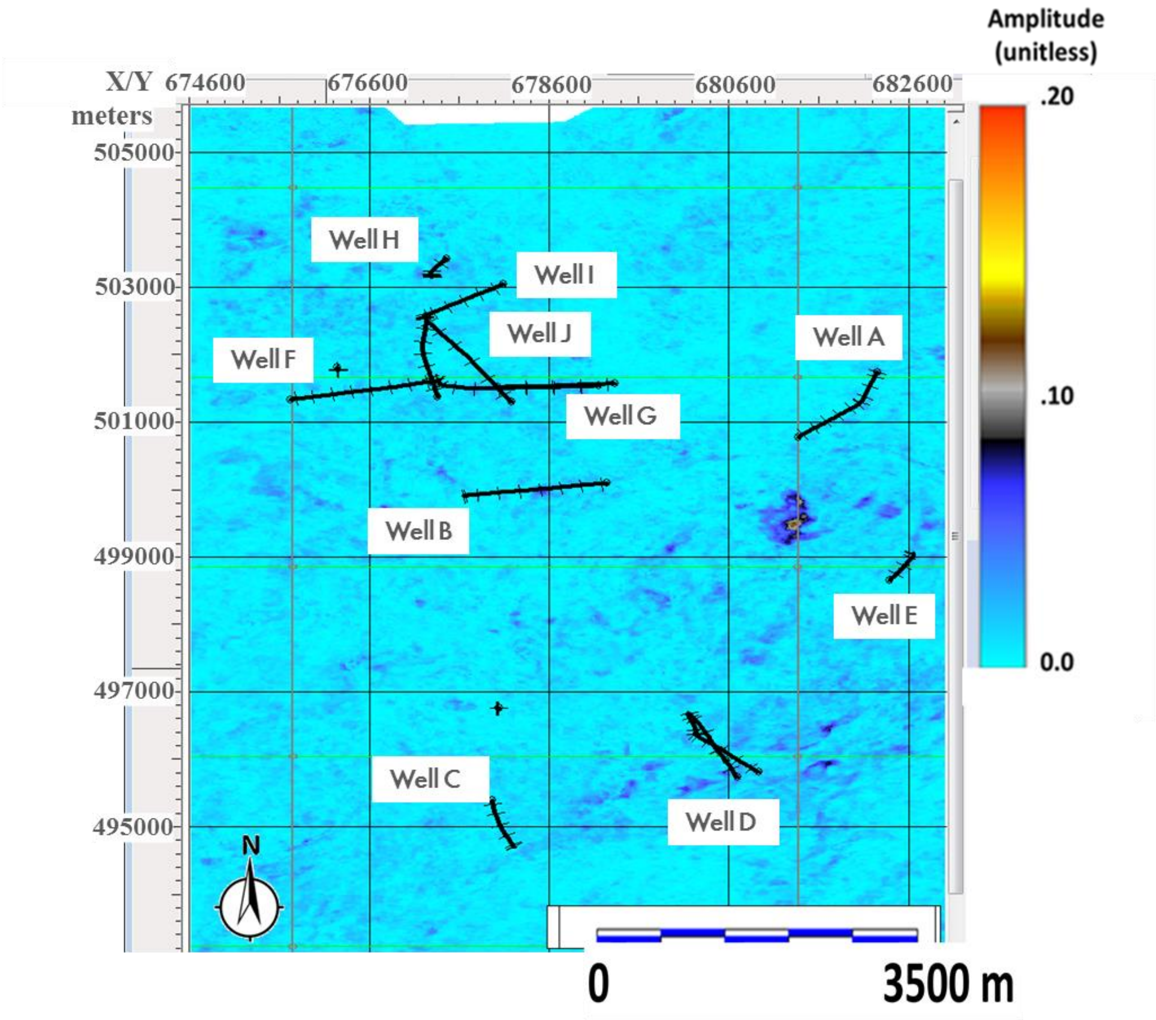

Figure B-4c: RMS amplitude map of ''Orange'' reservoir unit on +90° phase component of bandwidth-extended near stack. Red is high relative amplitude and light blue is low relative amplitude. Black lines are well paths. Solid black circles are bottom hole well locations. The amplitudes are relative and unitless.

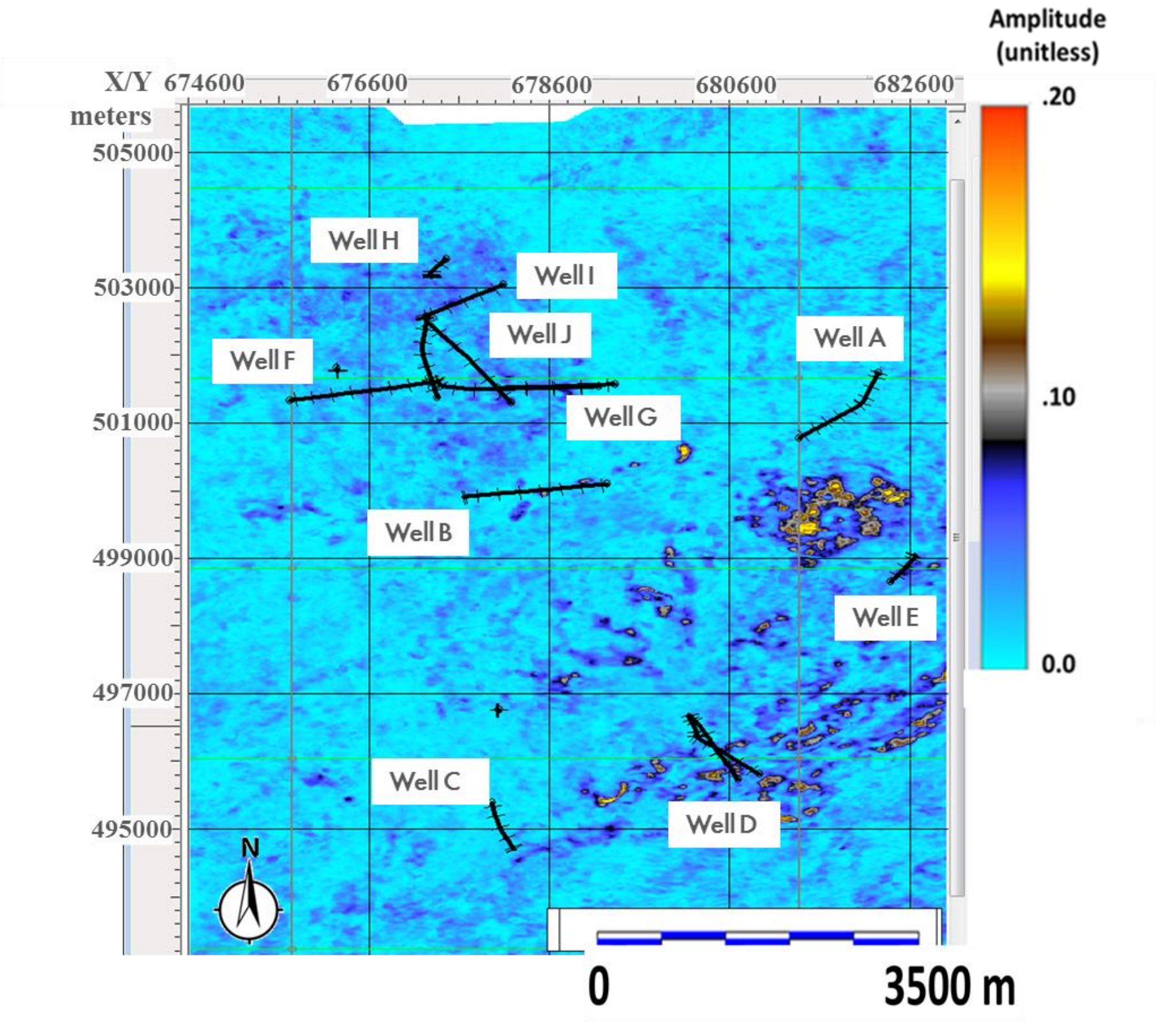

Figure B-4d: RMS amplitude map of ''Orange'' reservoir unit on -90° phase component of bandwidth-extended near stack. Red is high relative amplitude and light blue is low relative amplitude. Black lines are well paths. Solid black circles are bottom hole well locations. The amplitudes are relative and unitless.

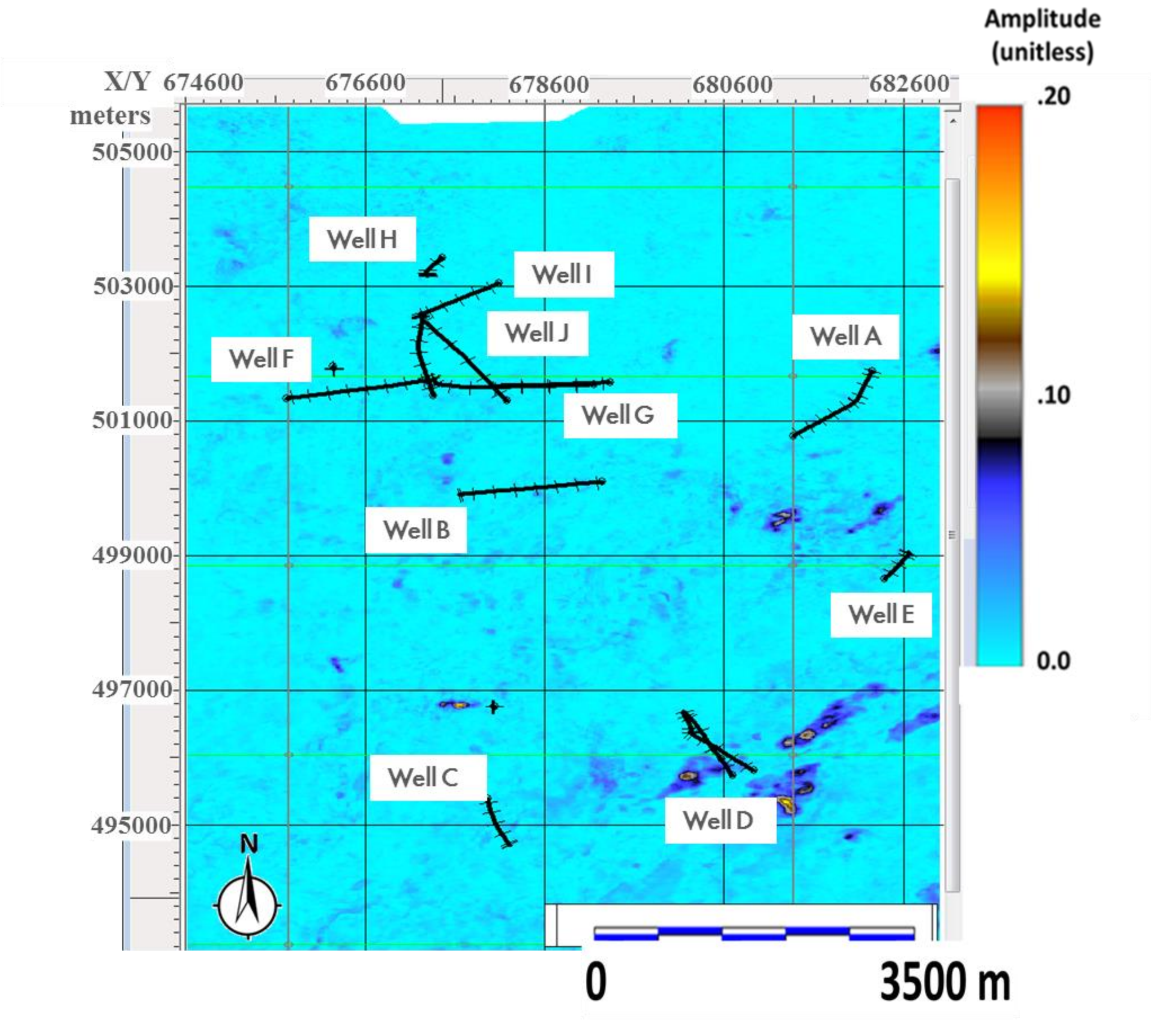

Figure B-5a: RMS amplitude map of ''Orange'' reservoir unit on 0° phase component of bandwidth-extended far stack. Red is high relative amplitude and light blue is low relative amplitude. Black lines are well paths. Solid black circles are bottom hole well locations. The amplitudes are relative and unitless.

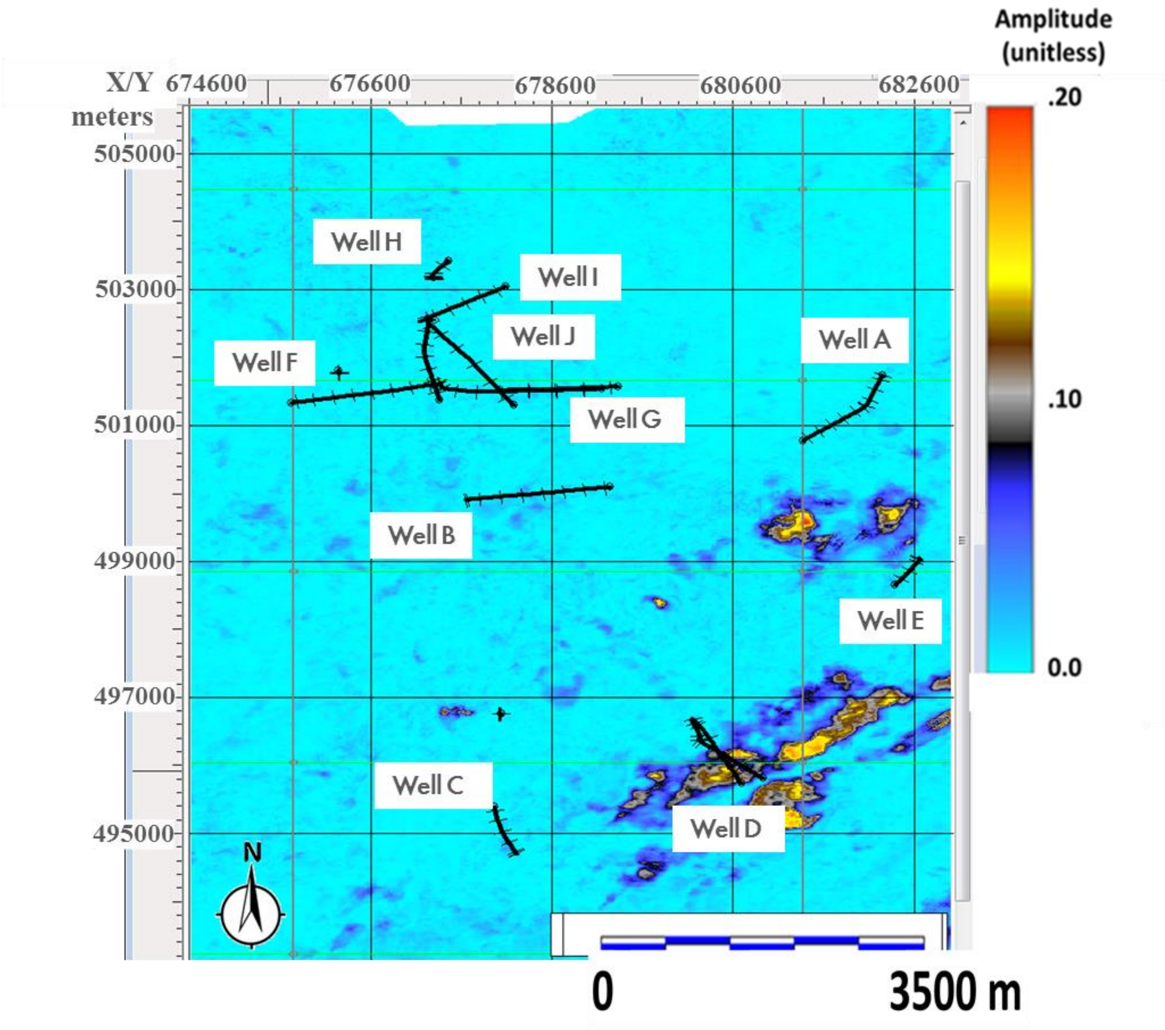

Figure B-5b: RMS amplitude map of ''Orange'' reservoir unit on 180° phase component of bandwidth-extended far stack. Red is high relative amplitude and light blue is low relative amplitude. Black lines are well paths. Solid black circles are bottom hole well locations. The amplitudes are relative and unitless.

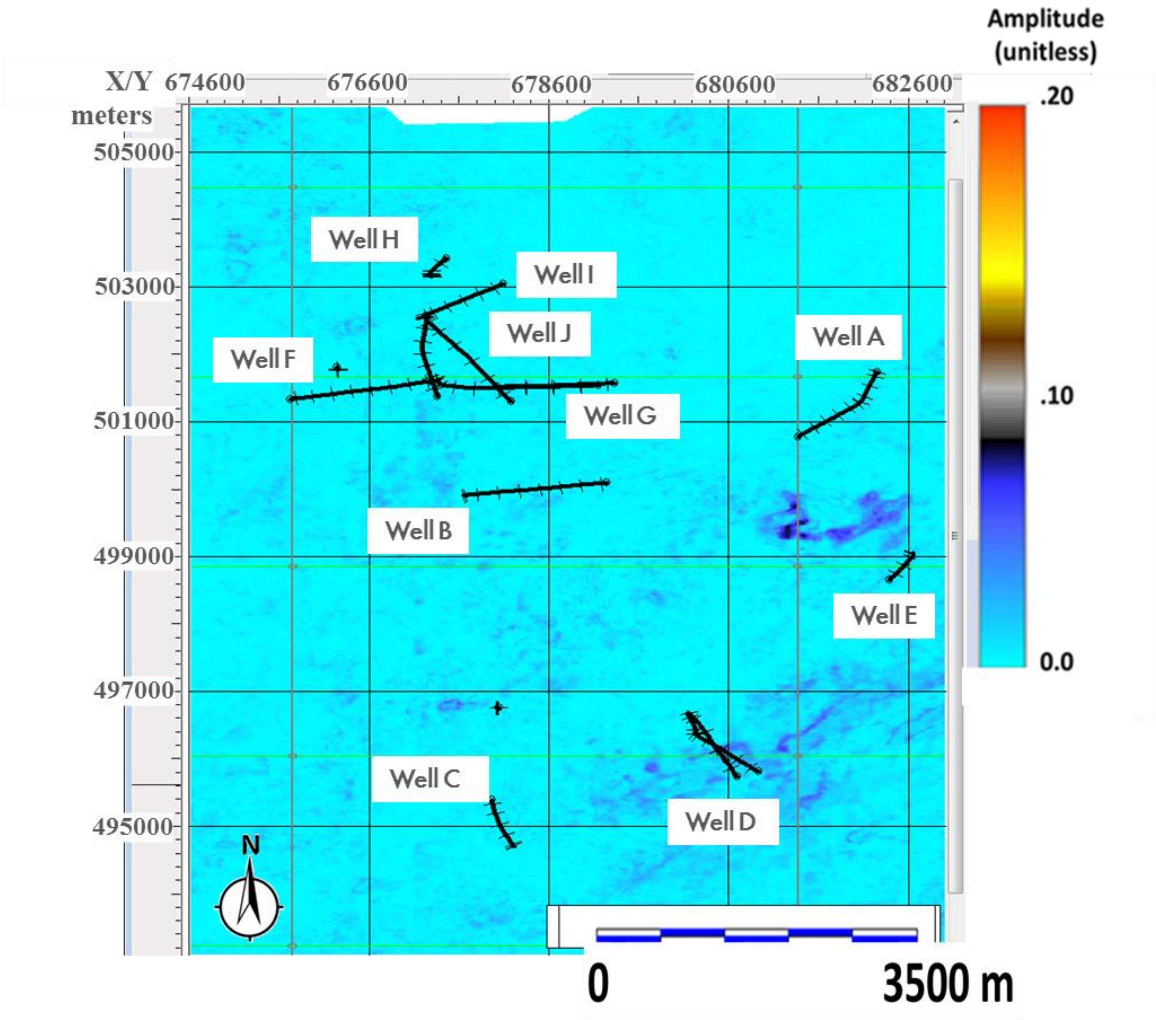

Figure B-5c: RMS amplitude map of ''Orange'' reservoir unit on +90° phase component of bandwidth-extended far stack. Red is high relative amplitude and light blue is low relative amplitude. Black lines are well paths. Solid black circles are bottom hole well locations. The amplitudes are relative and unitless.

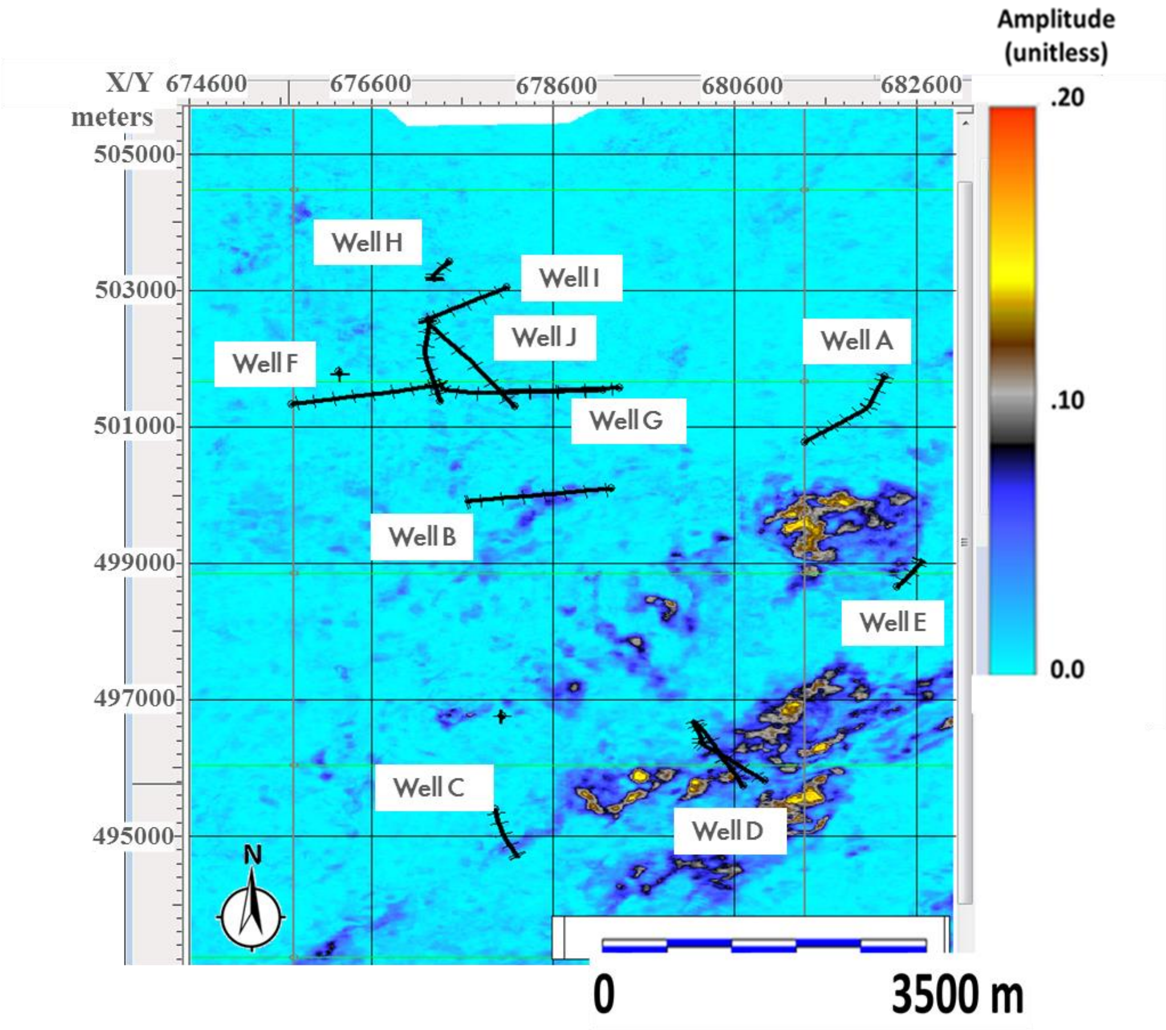

Figure B-5d: RMS amplitude map of ''Orange'' reservoir unit on -90° phase component of bandwidth-extended far stack. Red is high relative amplitude and light blue is low relative amplitude. Black lines are well paths. Solid black circles are bottom hole well locations. The amplitudes are relative and unitless.

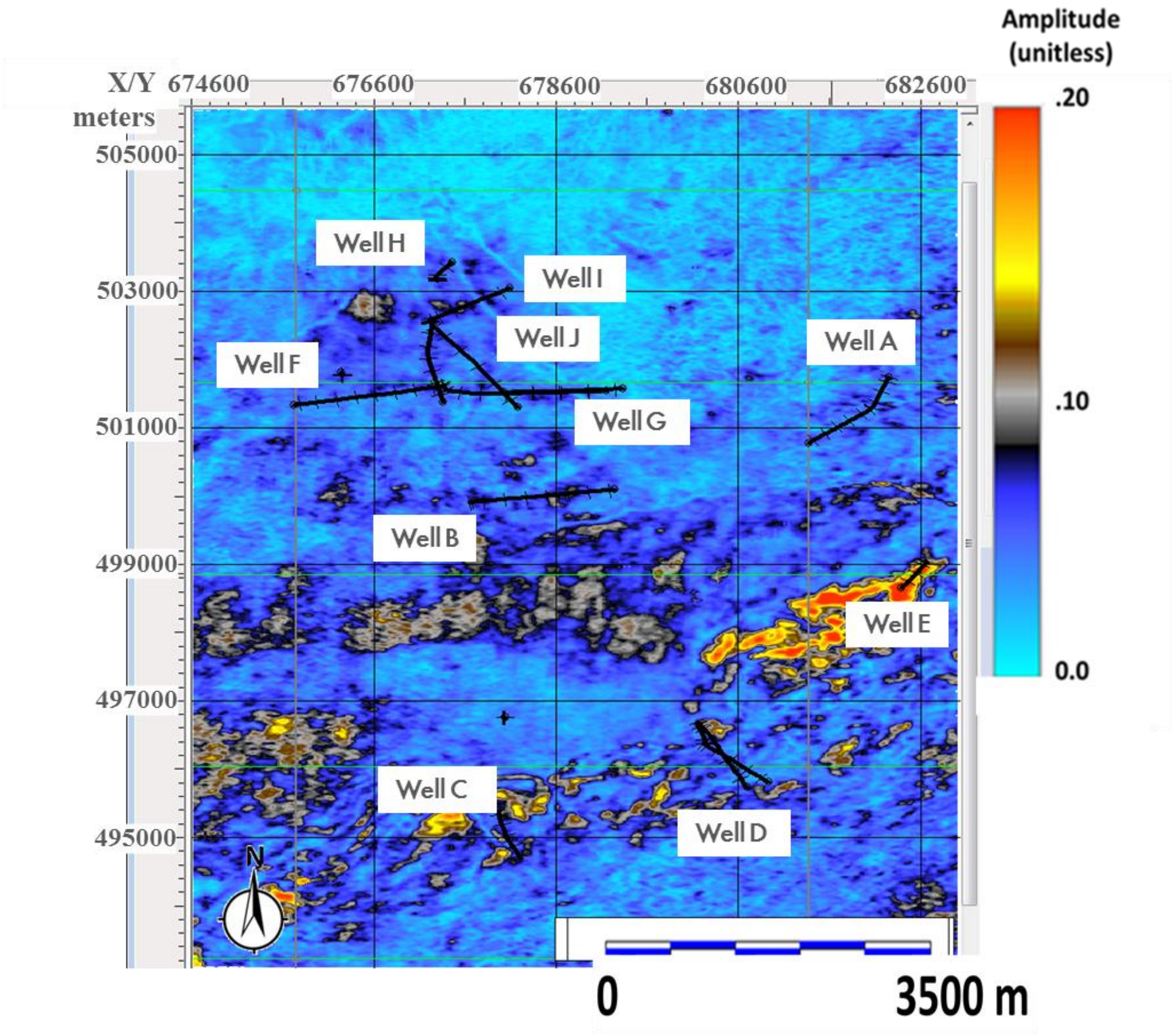

Figure B-6a: RMS amplitude map of ''Apple'' reservoir unit on original near stack. Red is high relative amplitude and light blue is low relative amplitude. Black lines are well paths. Solid black circles are bottom hole well locations. The amplitudes are relative and unitless.

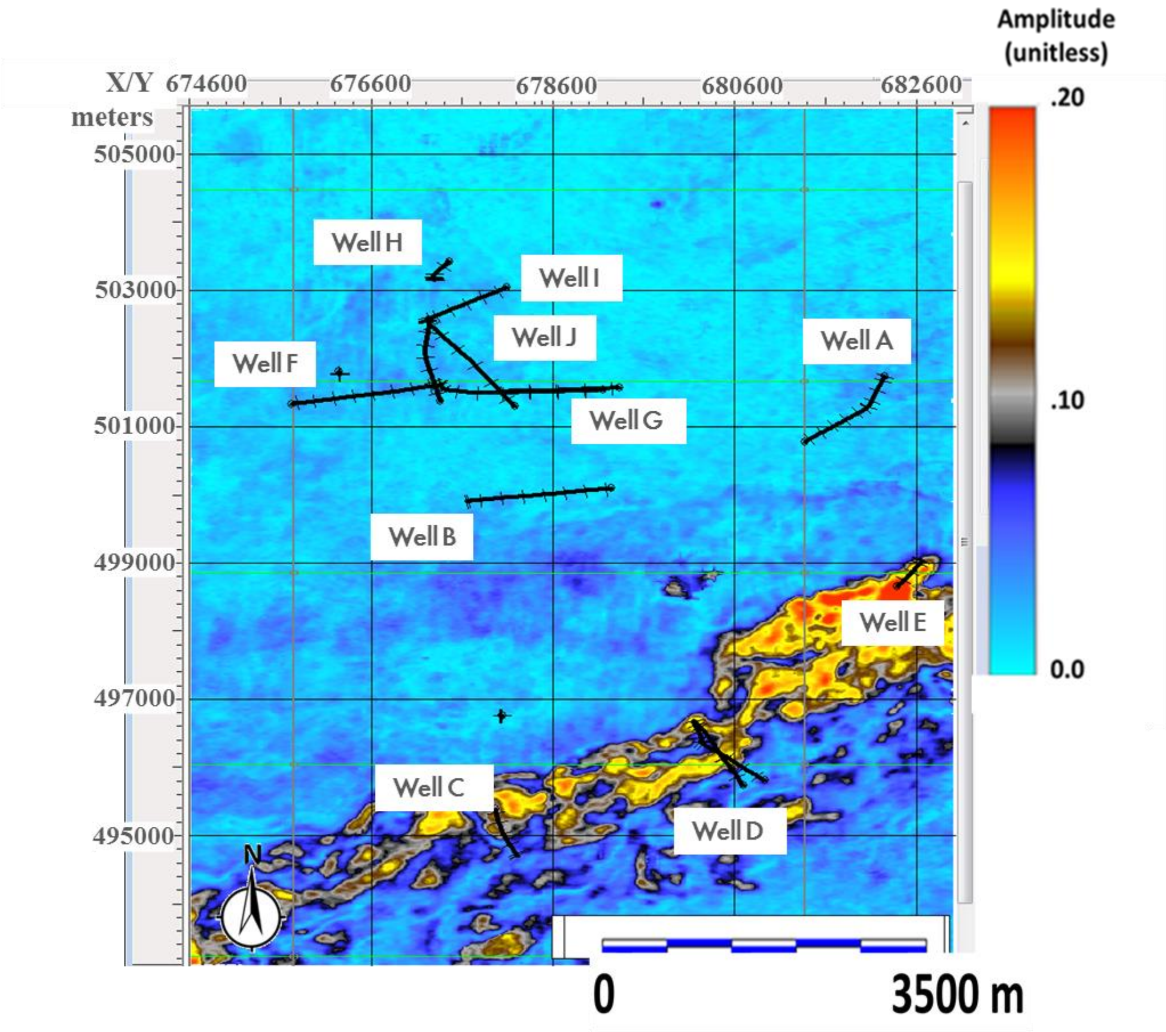

Figure B-6b: RMS amplitude map of ''Apple'' reservoir unit on original far stack. Red is high relative amplitude and light blue is low relative amplitude. Black lines are well paths. Solid black circles are bottom hole well locations. The amplitudes are relative and unitless.

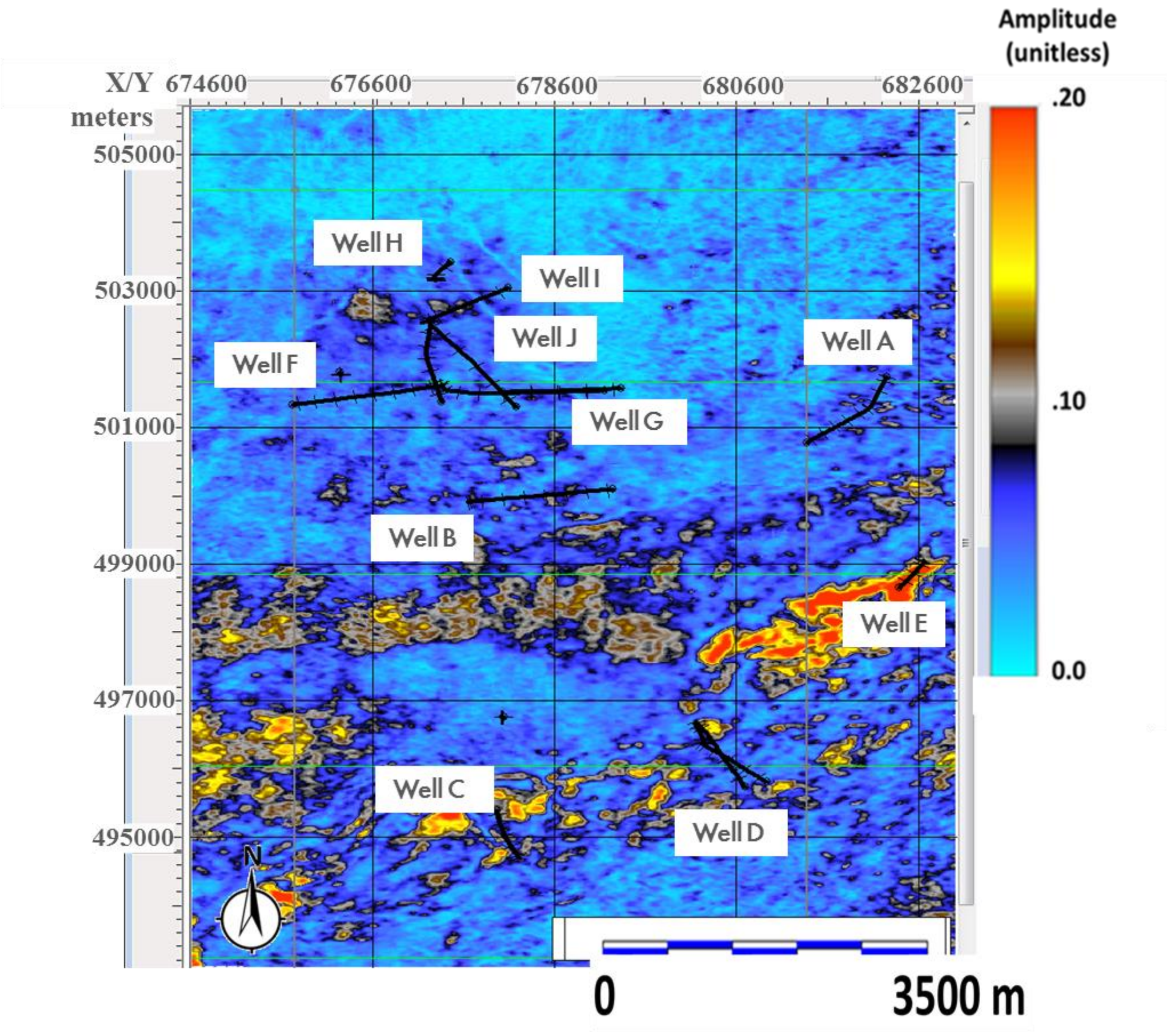

Figure B-6c: RMS amplitude map of ''Apple'' reservoir unit on bandwidth-extended near stack. Red is high relative amplitude and light blue is low relative amplitude. Black lines are well paths. Solid black circles are bottom hole well locations. The amplitudes are relative and unitless.

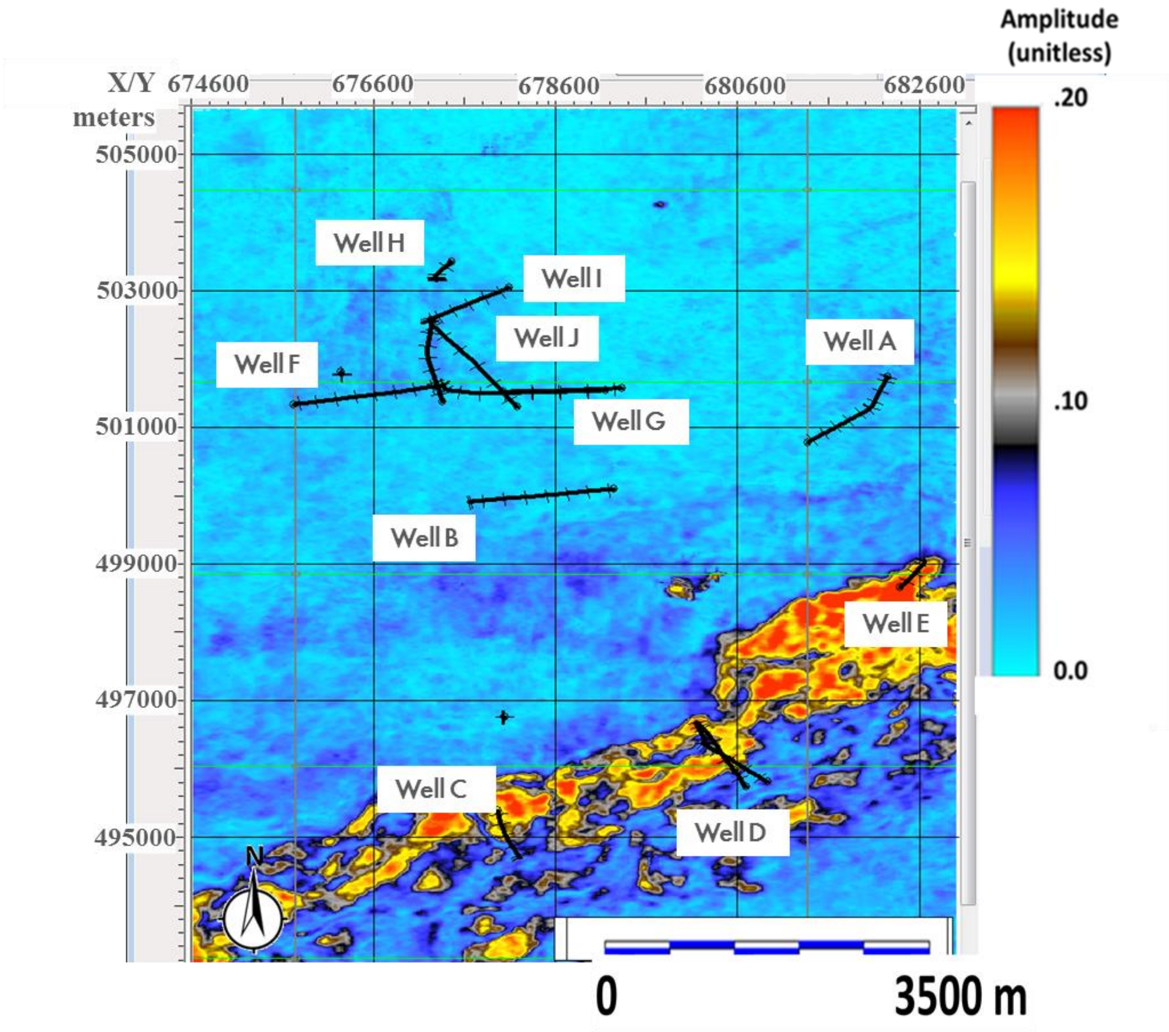

Figure B-6d: RMS amplitude map of ''Apple'' reservoir unit on bandwidth-extended far stack. Red is high relative amplitude and light blue is low relative amplitude. Black lines are well paths. Solid black circles are bottom hole well locations. The amplitudes are relative and unitless.

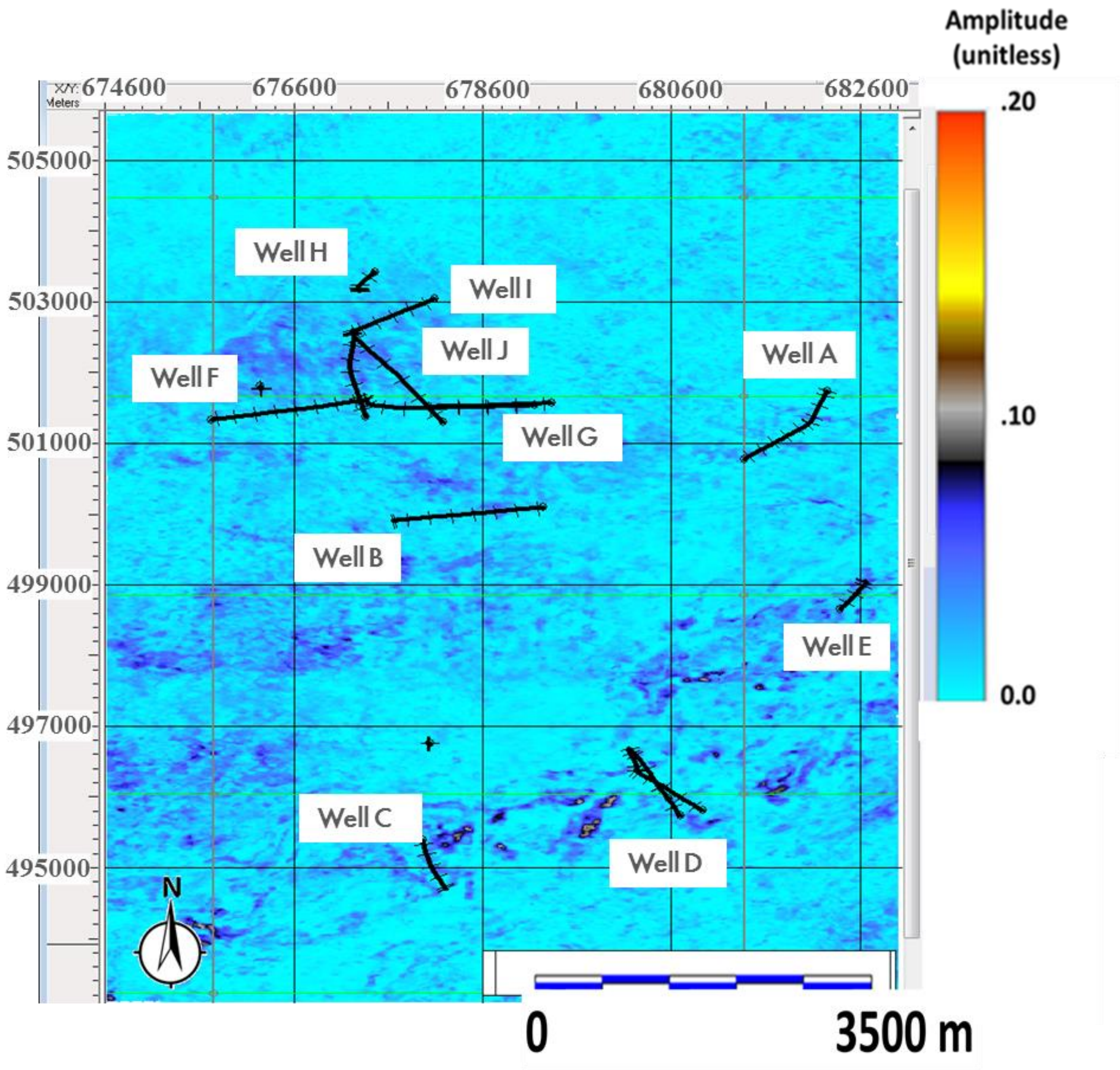

Figure B-7a: RMS amplitude map of ''Apple'' reservoir unit on 0° phase component of original near stack. Red is high relative amplitude and light blue is low relative amplitude. Black lines are well paths. Solid black circles are bottom hole well locations. The amplitudes are relative and unitless.

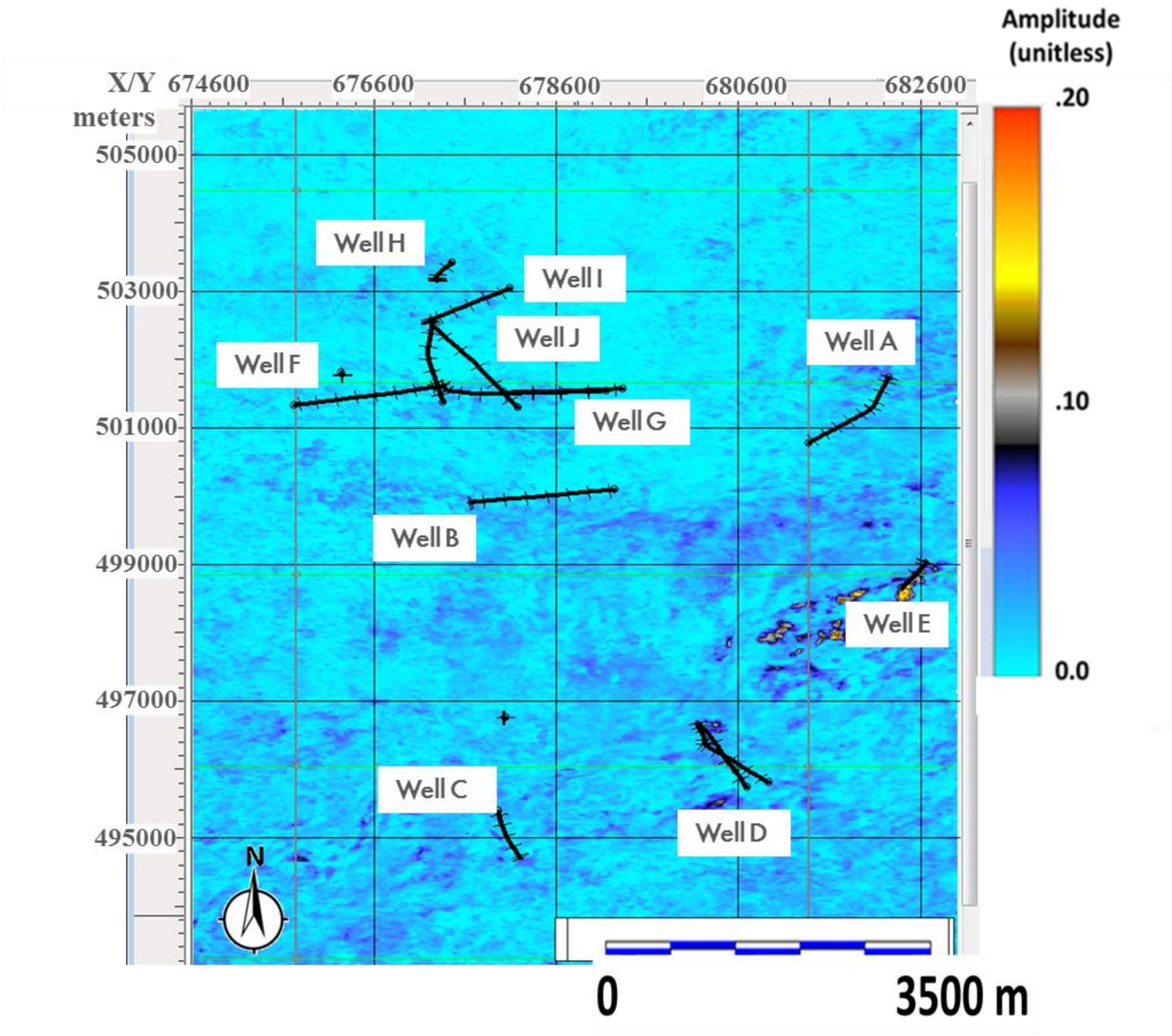

Figure B-7b: RMS amplitude map of ''Apple'' reservoir unit on 180° phase component of original near stack. Red is high relative amplitude and light blue is low relative amplitude. Black lines are well paths. Solid black circles are bottom hole well locations. The amplitudes are relative and unitless.

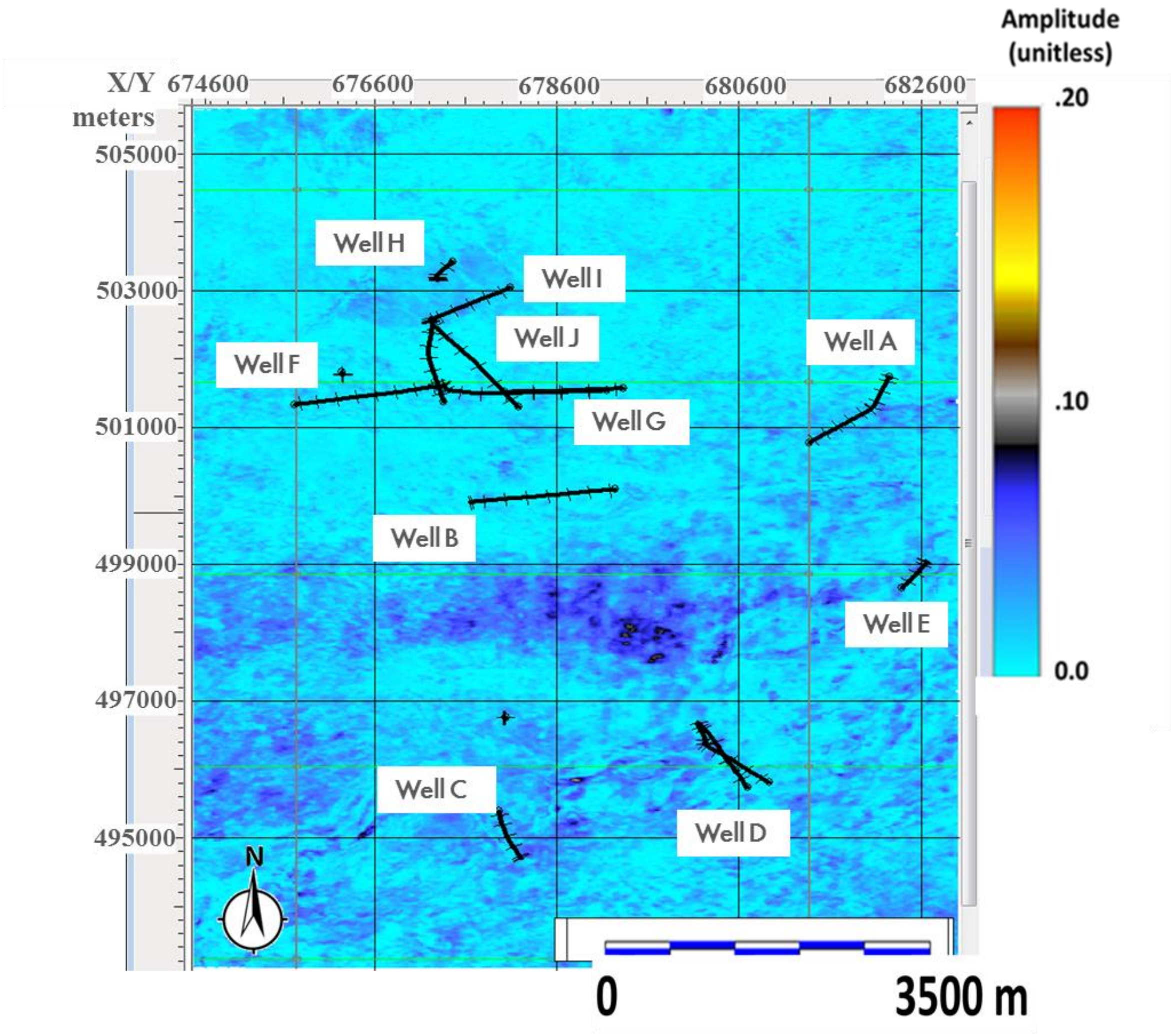

Figure B-7c: RMS amplitude map of ''Apple'' reservoir unit on +90° phase component of original near stack. Red is high relative amplitude and light blue is low relative amplitude. Black lines are well paths. Solid black circles are bottom hole well locations. The amplitudes are relative and unitless.

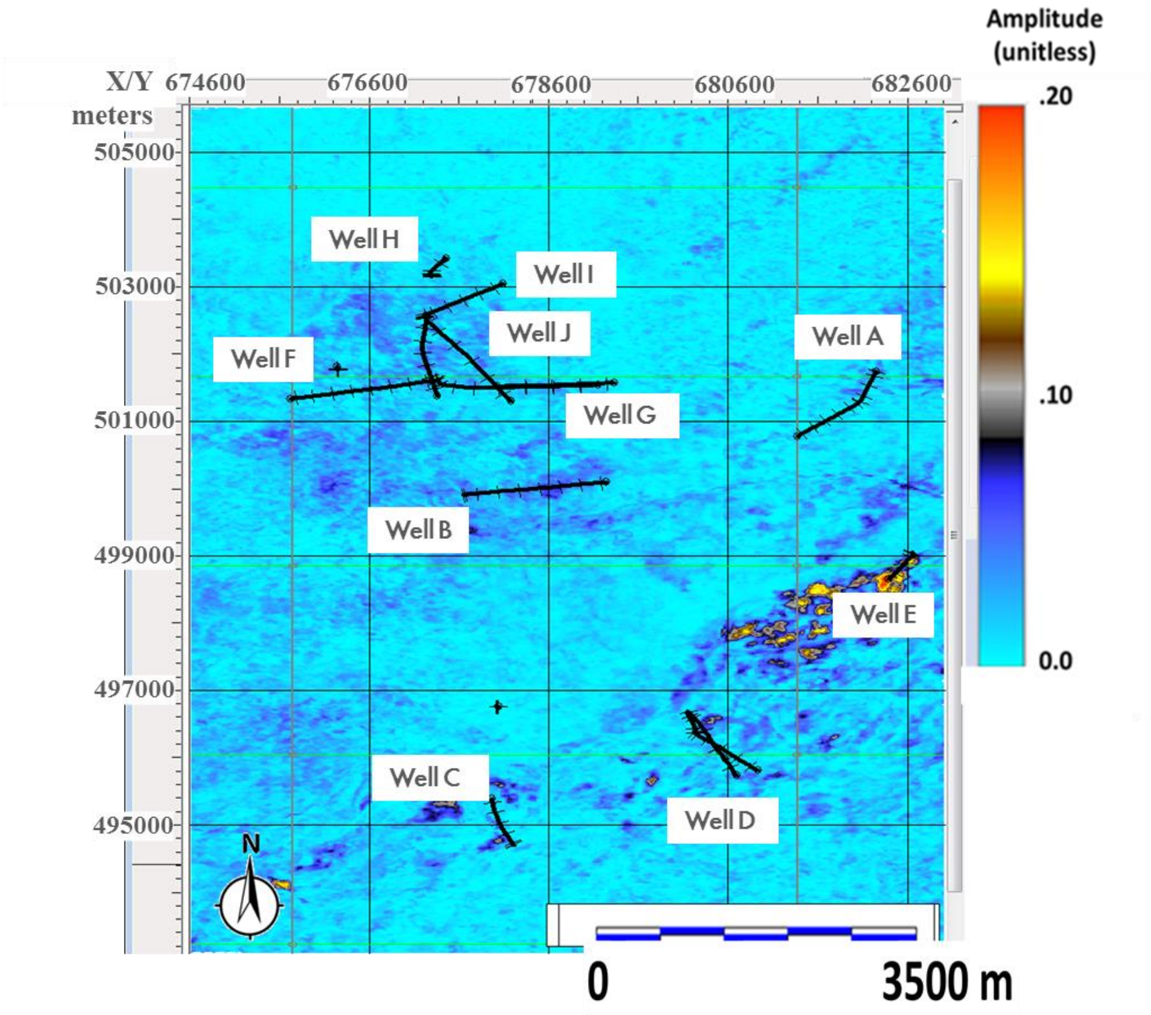

Figure B-7d: RMS amplitude map of ''Apple'' reservoir unit on -90° phase component of original near stack. Red is high relative amplitude and light blue is low relative amplitude. Black lines are well paths. Solid black circles are bottom hole well locations. The amplitudes are relative and unitless.

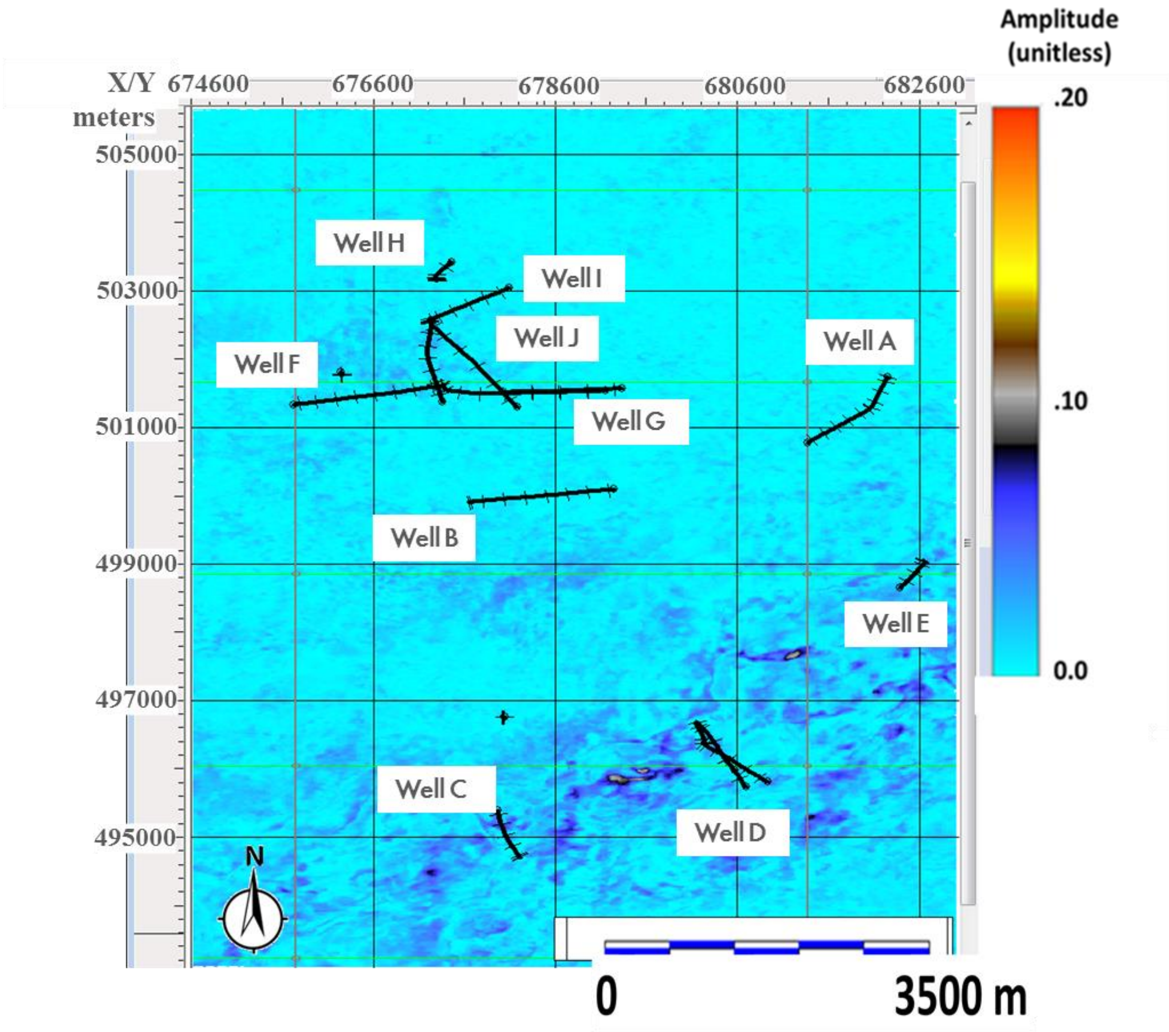

Figure B-8a: RMS amplitude map of ''Apple'' reservoir unit on 0° phase component of original far stack. Red is high relative amplitude and light blue is low relative amplitude. Black lines are well paths. Solid black circles are bottom hole well locations. The amplitudes are relative and unitless.

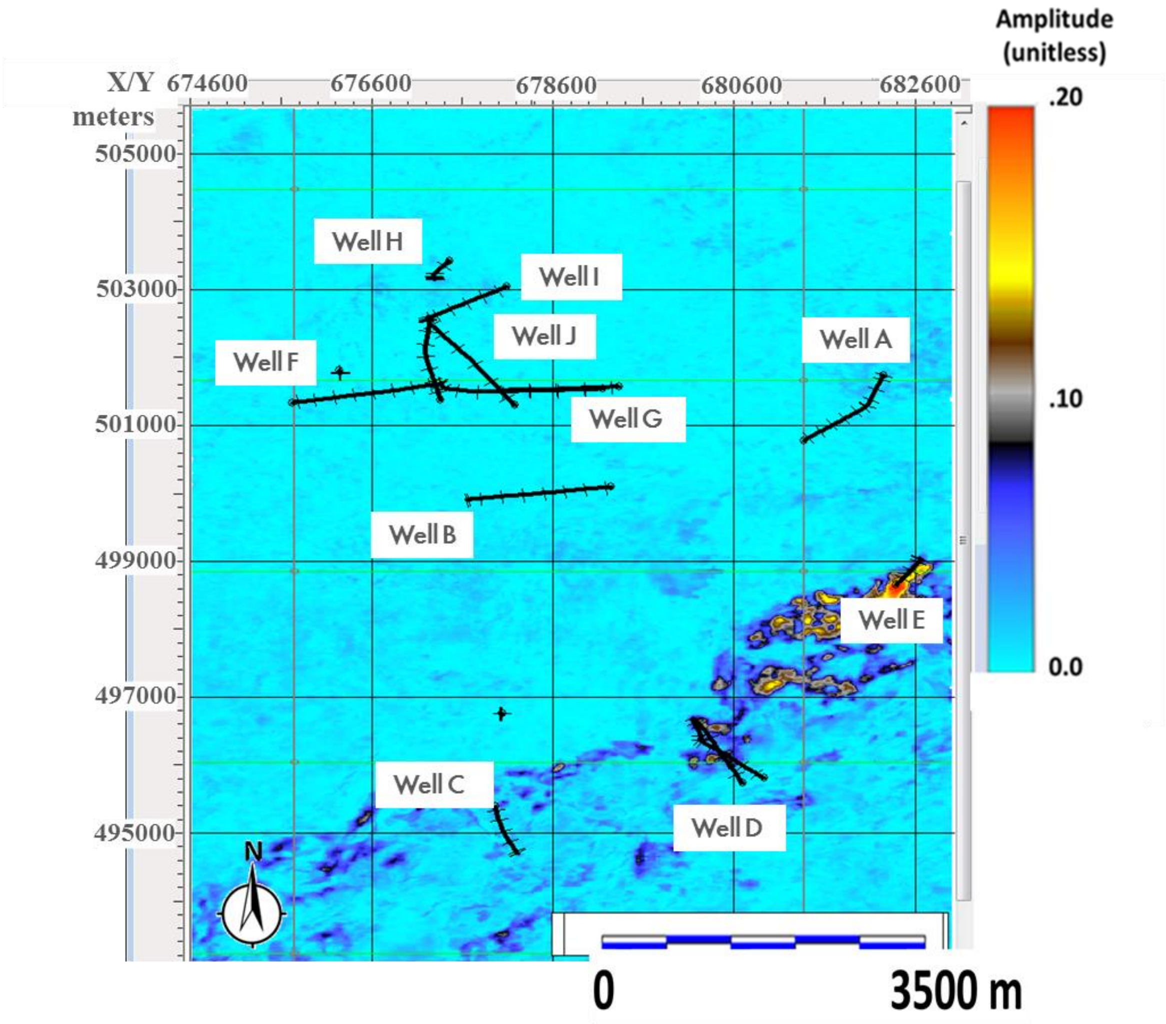

Figure B-8b: RMS amplitude map of ''Apple'' reservoir unit on 180° phase component of original far stack. Red is high relative amplitude and light blue is low relative amplitude. Black lines are well paths. Solid black circles are bottom hole well locations. The amplitudes are relative and unitless.

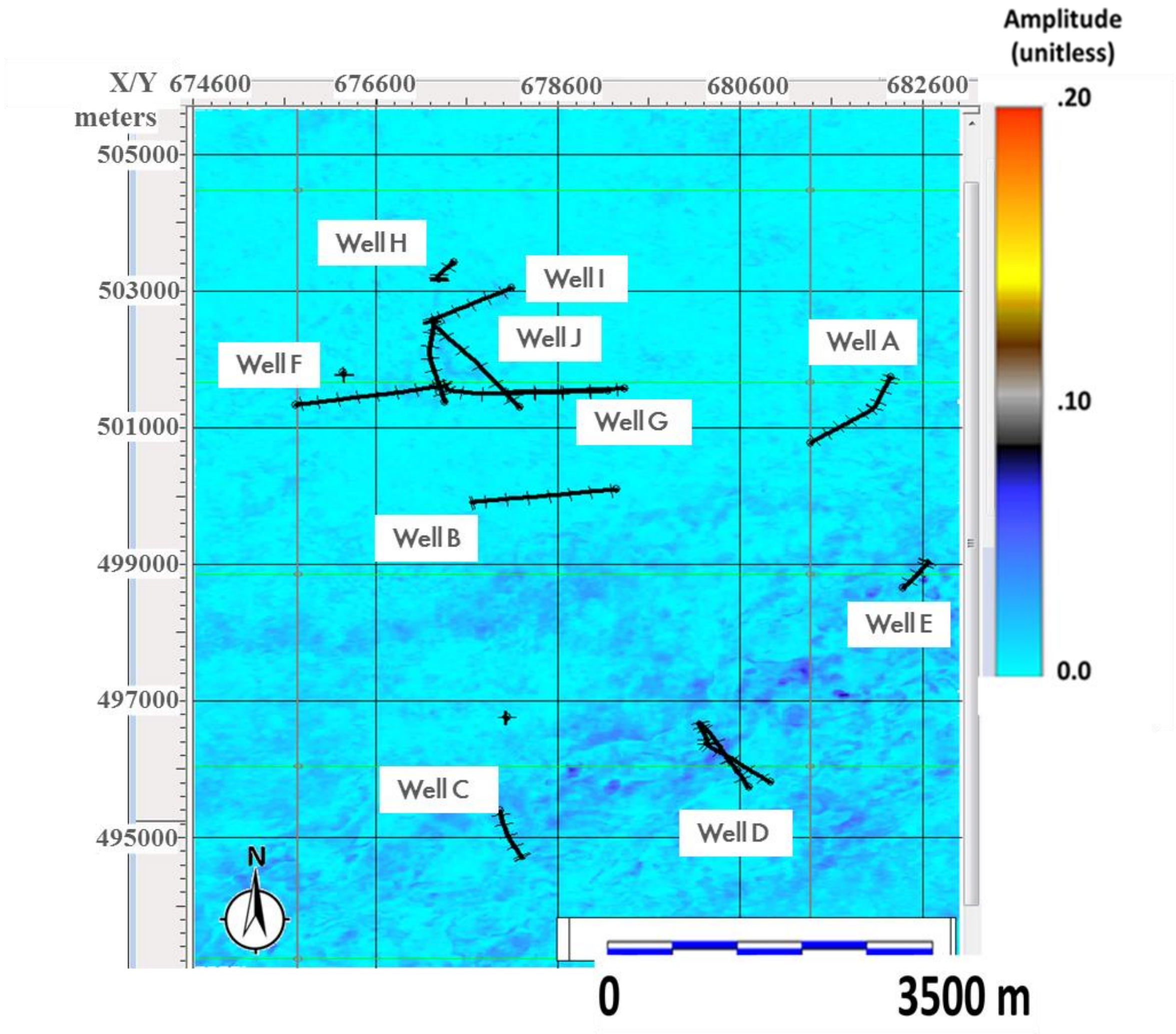

Figure B-8c: RMS amplitude map of ''Apple'' reservoir unit on +90° phase component of original far stack. Red is high relative amplitude and light blue is low relative amplitude. Black lines are well paths. Solid black circles are bottom hole well locations. The amplitudes are relative and unitless.

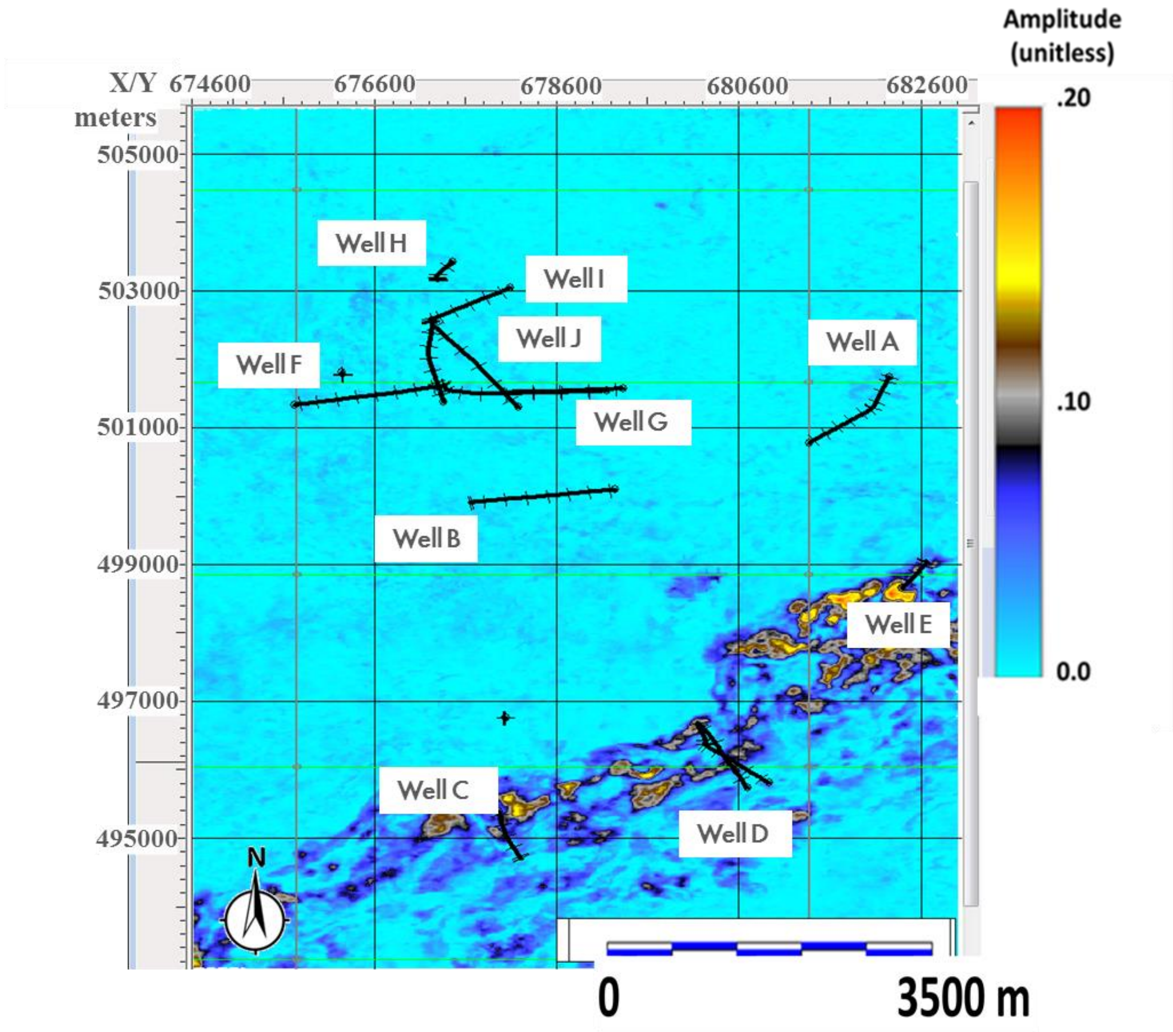

Figure B-8d: RMS amplitude map of ''Apple'' reservoir unit on -90° phase component of original far stack. Red is high relative amplitude and light blue is low relative amplitude. Black lines are well paths. Solid black circles are bottom hole well locations. The amplitudes are relative and unitless.

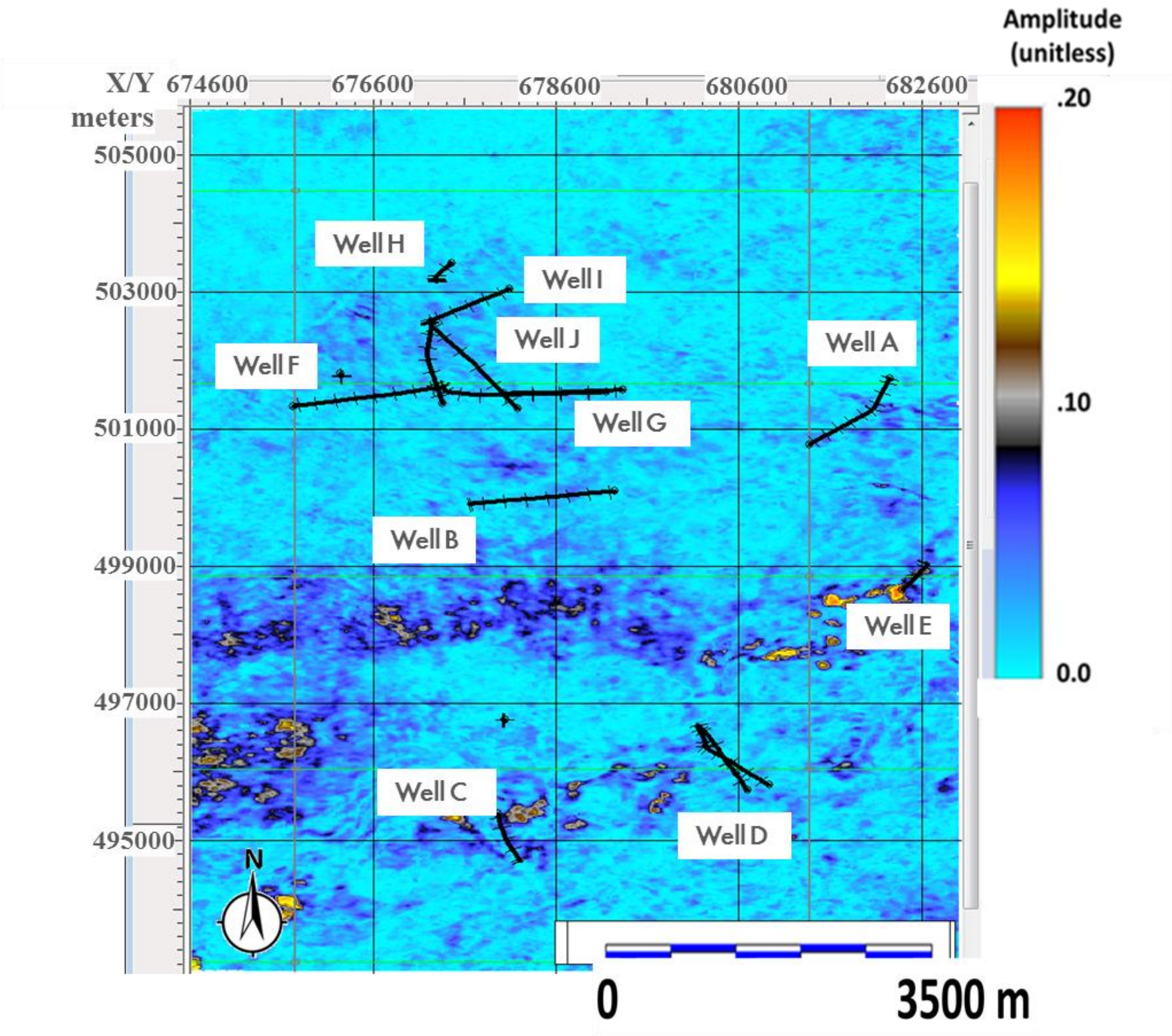

Figure B-9a: RMS amplitude map of ''Apple'' reservoir unit on 0° phase component of bandwidth-extended near stack. Red is high relative amplitude and light blue is low relative amplitude. Black lines are well paths. Solid black circles are bottom hole well locations. The amplitudes are relative and unitless.

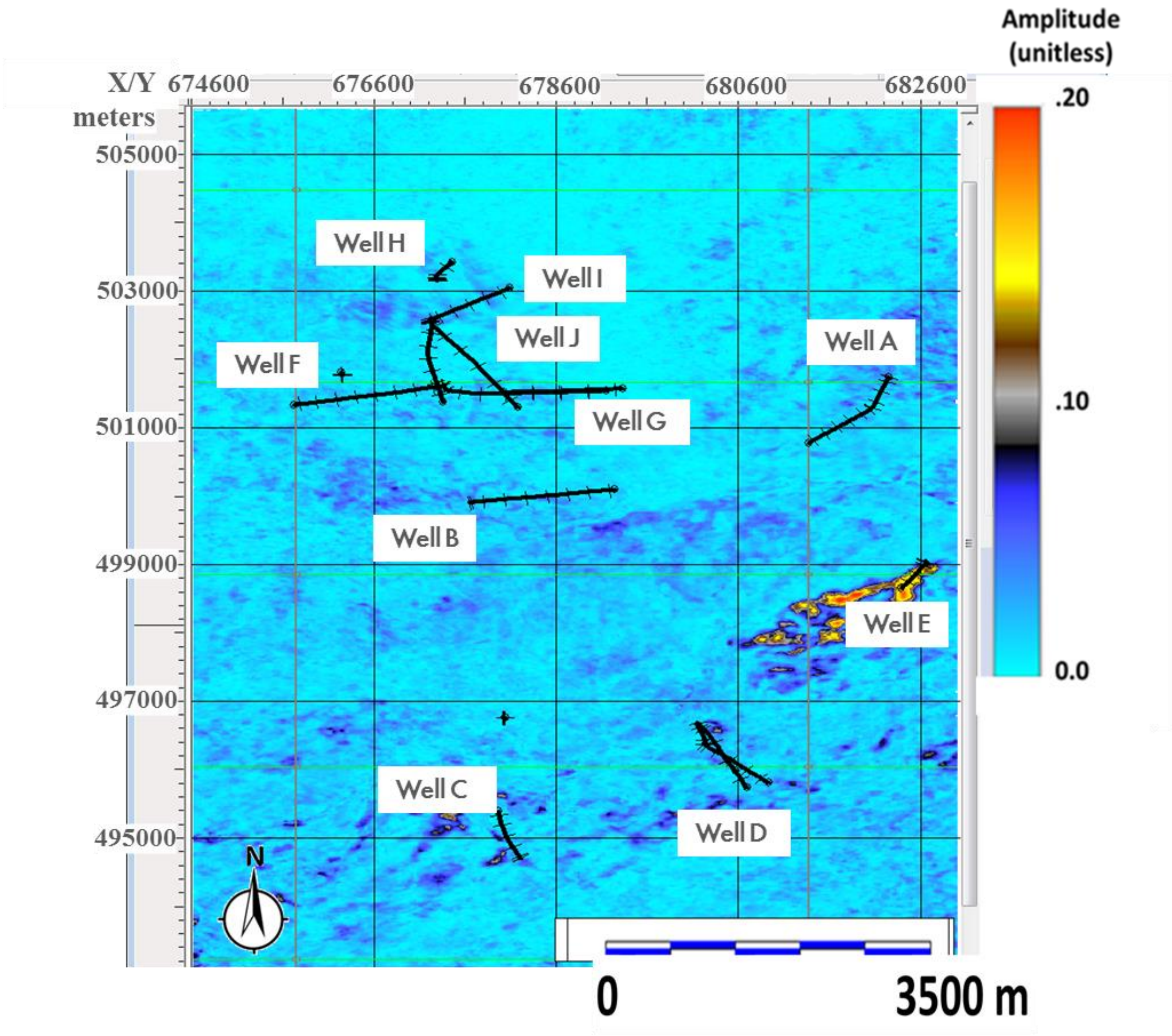

Figure B-9b: RMS amplitude map of ''Apple'' reservoir unit on 180° phase component of bandwidth-extended near stack. Red is high relative amplitude and light blue is low relative amplitude. Black lines are well paths. Solid black circles are bottom hole well locations. The amplitudes are relative and unitless.

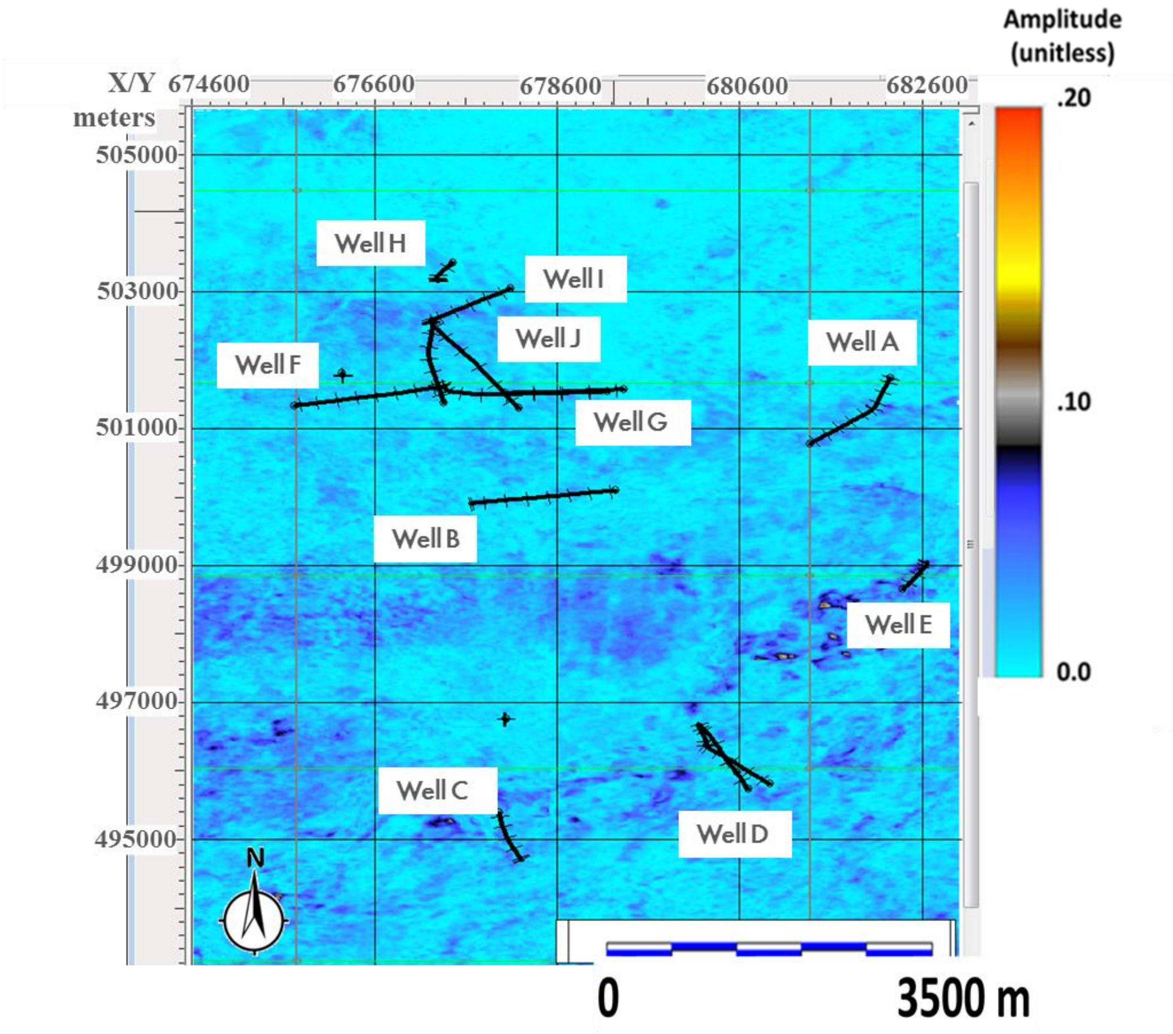

Figure B-9c: RMS amplitude map of ''Apple'' reservoir unit on +90° phase component of bandwidth-extended near stack. Red is high relative amplitude and light blue is low relative amplitude. Black lines are well paths. Solid black circles are bottom hole well locations. The amplitudes are relative and unitless.

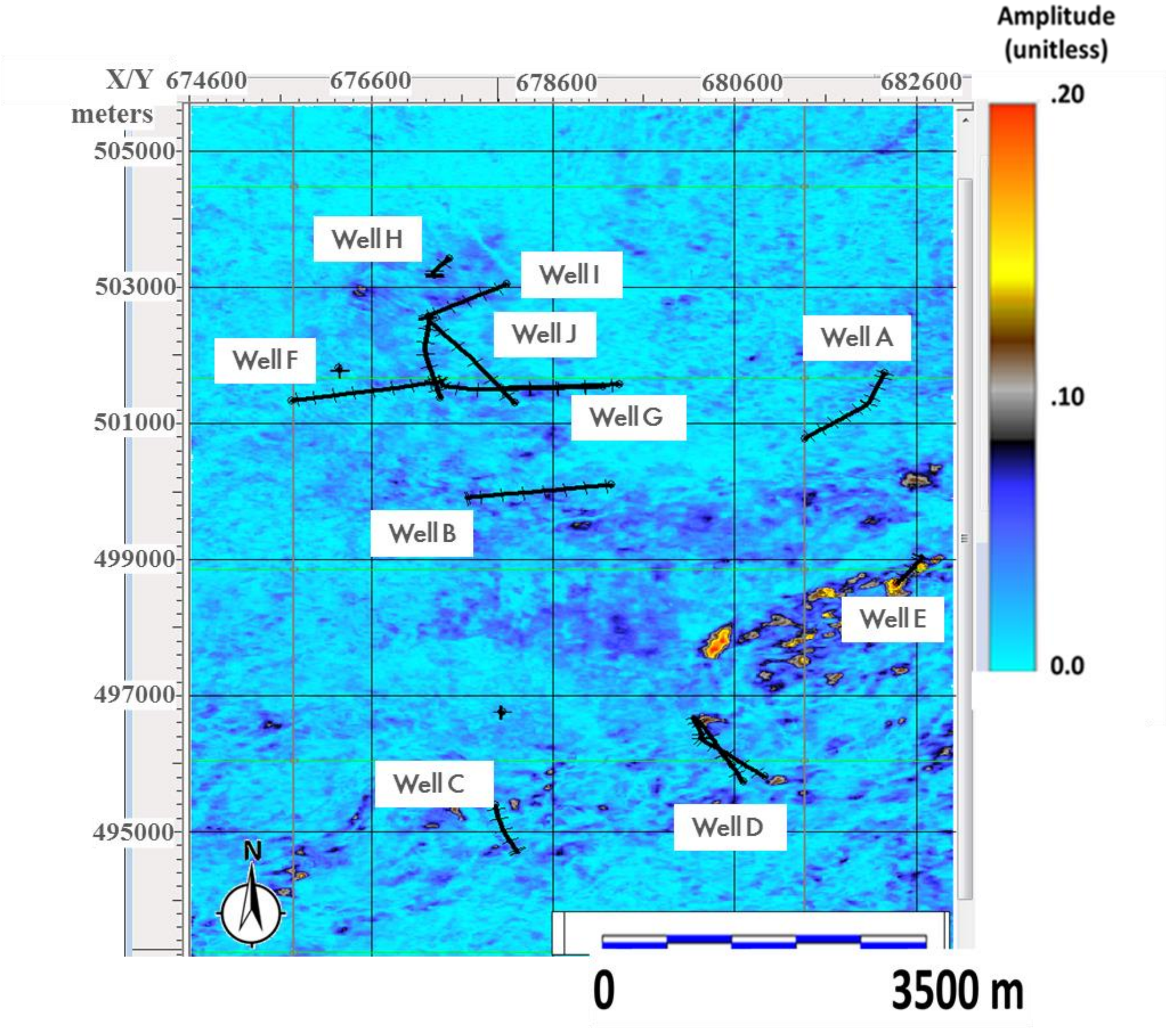

Figure B-9d: RMS amplitude map of ''Apple'' reservoir unit on -90° phase component of bandwidth-extended near stack. Red is high relative amplitude and light blue is low relative amplitude. Black lines are well paths. Solid black circles are bottom hole well locations. The amplitudes are relative and unitless.

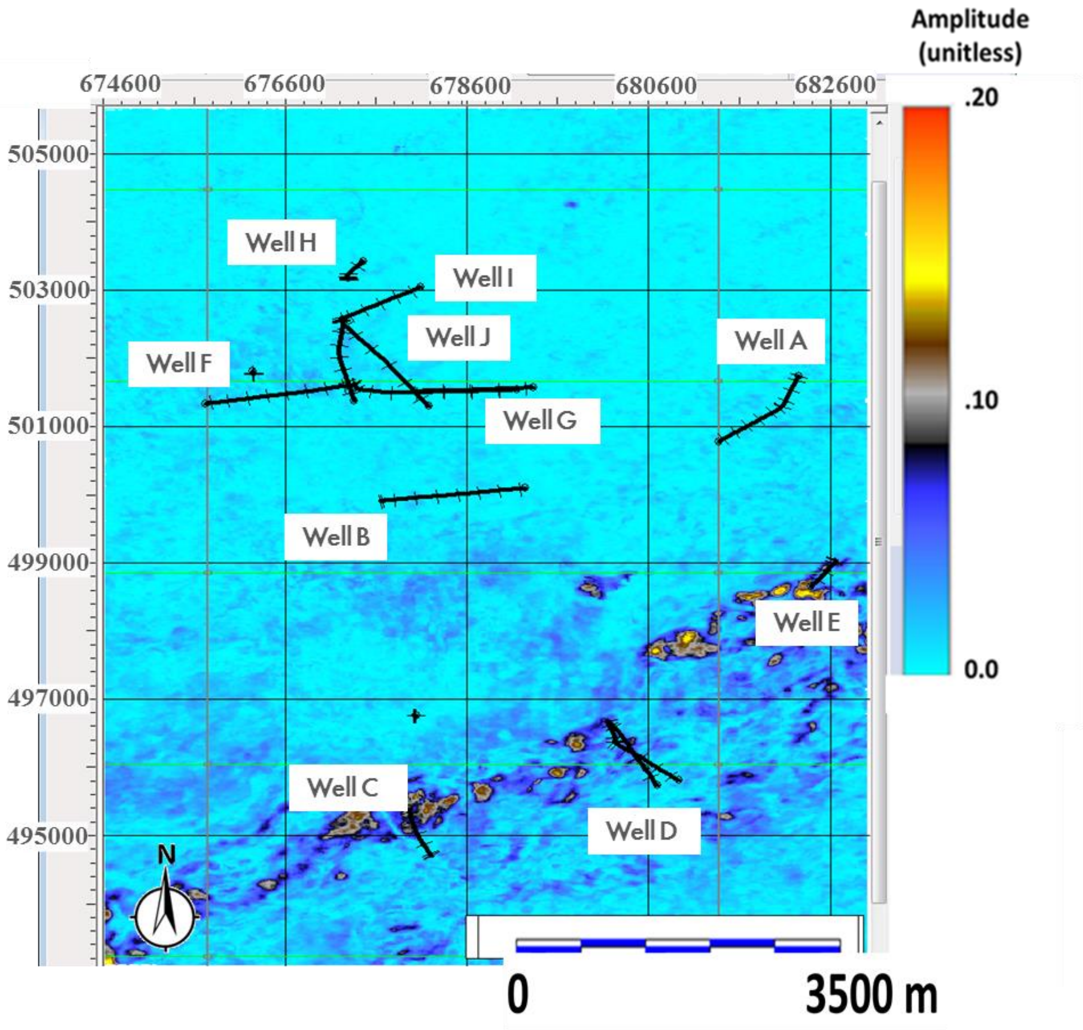

Figure B-10a: RMS amplitude map of ''Apple'' reservoir unit on 0° phase component of bandwidth-extended far stack. Red is high relative amplitude and light blue is low relative amplitude. Black lines are well paths. Solid black circles are bottom hole well locations. The amplitudes are relative and unitless.

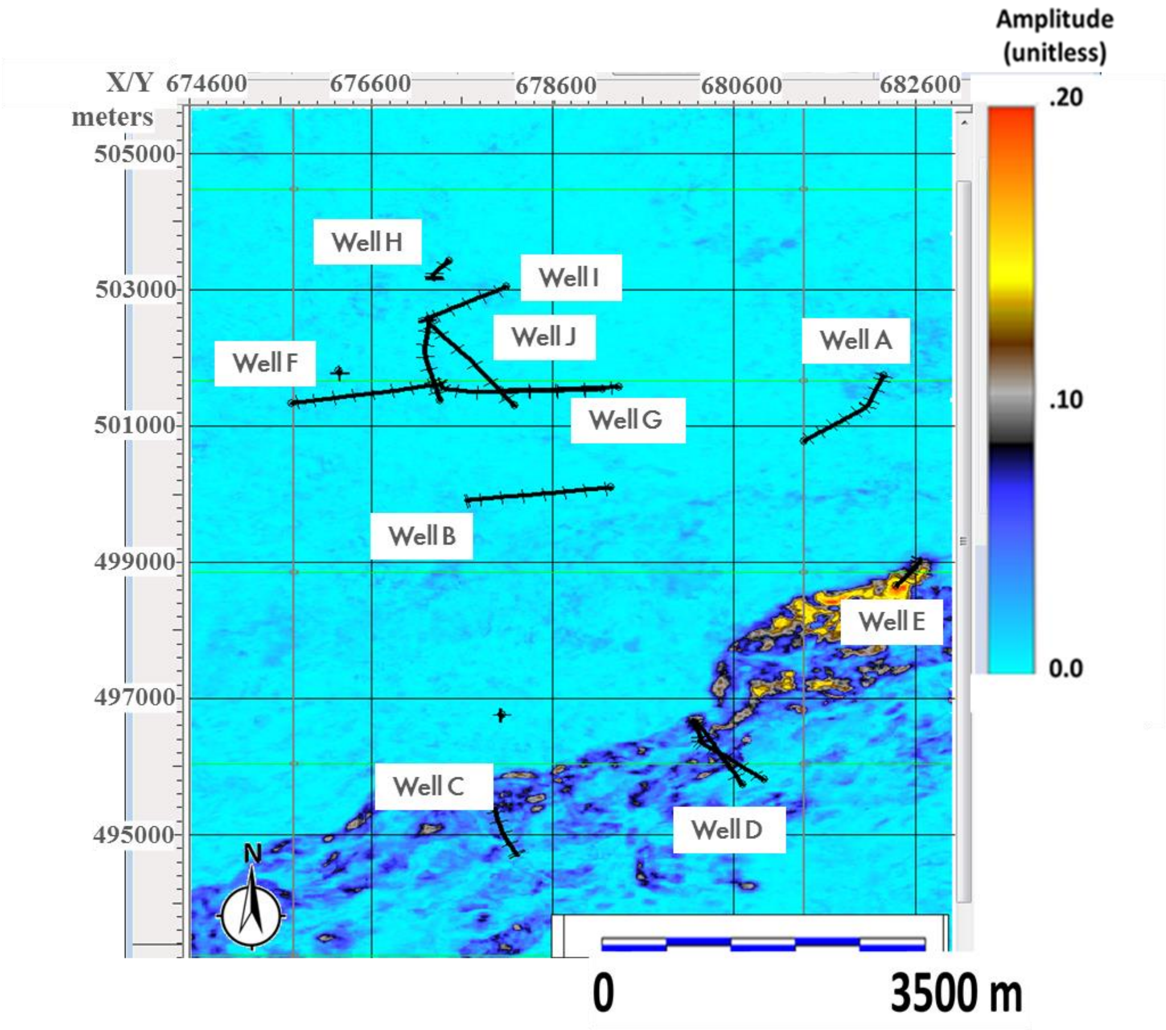

Figure B-10b: RMS amplitude map of ''Apple'' reservoir unit on 180° phase component of bandwidth-extended far stack. Red is high relative amplitude and light blue is low relative amplitude. Black lines are well paths. Solid black circles are bottom hole well locations. The amplitudes are relative and unitless.

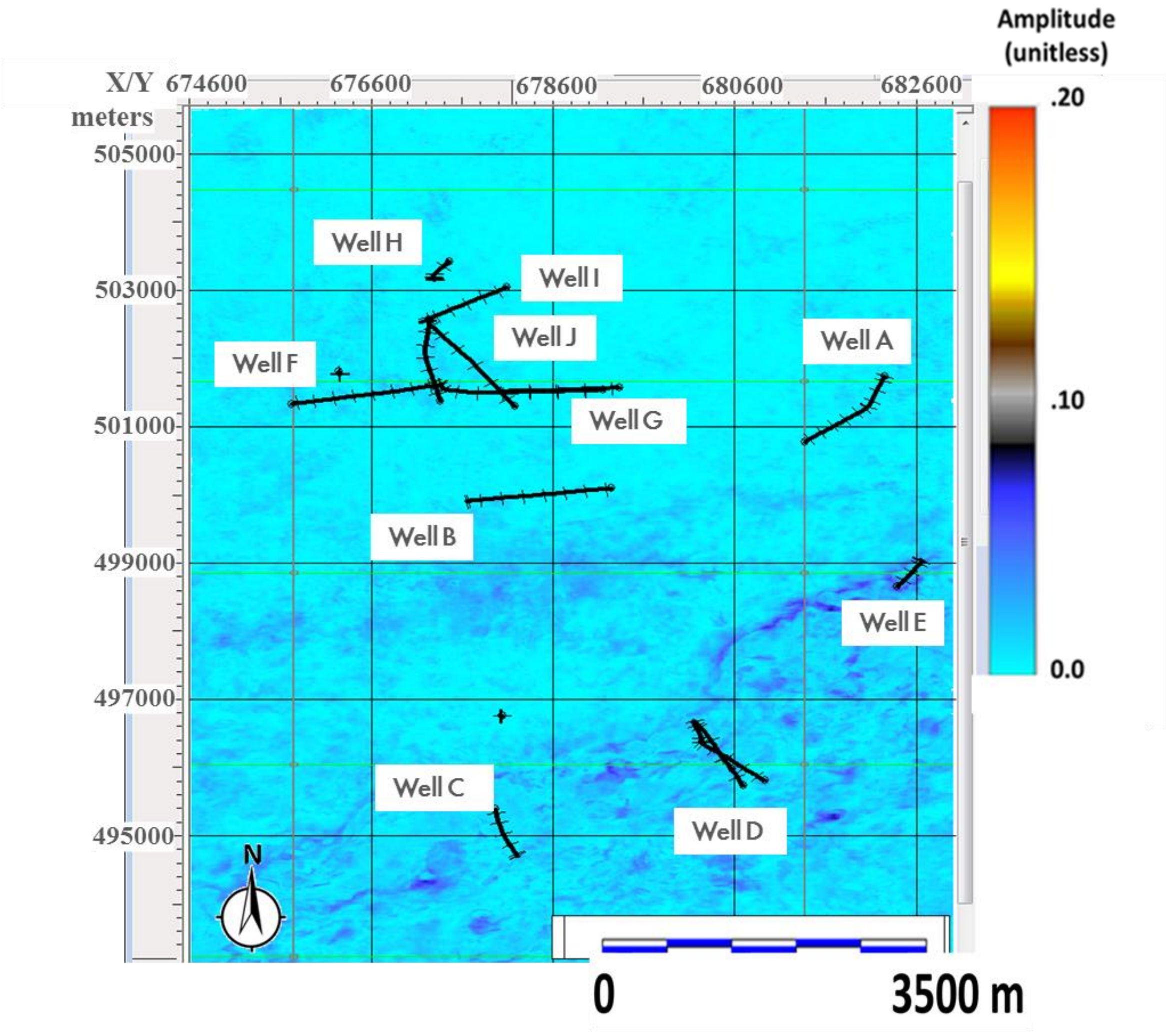

Figure B-10c: RMS amplitude map of ''Apple'' reservoir unit on +90° phase component of bandwidth-extended far stack. Red is high relative amplitude and light blue is low relative amplitude. Black lines are well paths. Solid black circles are bottom hole well locations. The amplitudes are relative and unitless.

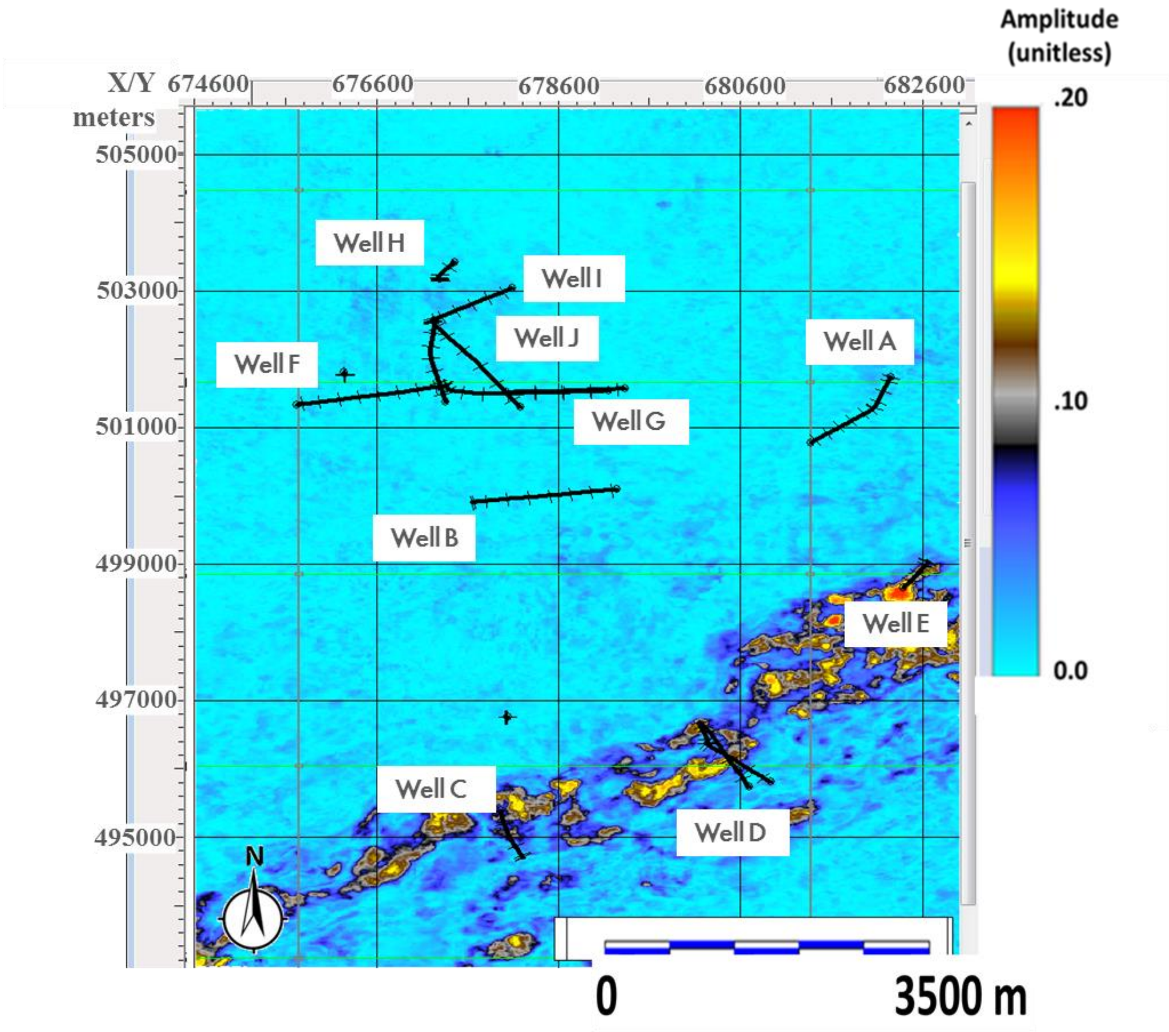

Figure B-10d: RMS amplitude map of ''Apple'' reservoir unit on -90° phase component of bandwidth-extended far stack. Red is high relative amplitude and light blue is low relative amplitude. Black lines are well paths. Solid black circles are bottom hole well locations. The amplitudes are relative and unitless.